Master's thesis

NTNU
Norwegian University of Science and Technology
Faculty of Engineering
Department of Marine Technology

Helen Abraham
Amund Garsrud Tvedt

A Feasibility Study of a Renewable-Energy Supply for an Offshore Oil and Gas Installation

Master's thesis in Marine Technology
Supervisor: Marilena Greco
Co-supervisor: Claudio Lugni
June 2022

NTNU
Norwegian University of
Science and Technology

Helen Abraham
Amund Garsrud Tvedt

A Feasibility Study of a Renewable-Energy Supply for an Offshore Oil and Gas Installation

Master's thesis in Marine Technology
Supervisor: Marilena Greco
Co-supervisor: Claudio Lugni
June 2022

Norwegian University of Science and Technology
Faculty of Engineering
Department of Marine Technology

NTNU
Norwegian University of
Science and Technology

NTNU Trondheim
Norwegian University of Science and Technology
Faculty of Engineering Science and Technology
Department of MarineTechnology

MASTER THESIS IN MARINE TECHNOLOGY

Spring 2022

FOR

Helen Abraham, Amund Garsrud Tvedt

A Feasibility Study of a Renewable-Energy Supply for an Offshore Oil and Gas Installation

(En mulighetsstudie av en fornybar energiforsyning for en offshore olje- og gassinstallasjon)

Powering offshore oil and gas activities with marine renewables offers opportunities for the energy industry and the society. In fact, it is challenging and often extremely expensive to supply power to offshore operations, particularly due to the need of sending boats out to deliver fuel supplies and/or batteries or due to the use of long supply cables. Marine renewables can provide power in loco, which could be combined with local over-power storage for a continuous supply to the oil and gas installations. This use can also speed up the development of marine renewables towards mainstream power markets and can reduce at the same time the carbon footprint of the oil and gas industry itself. Offshore wind (OW) represents a good candidate in this context. Floating wind turbines could be deployed more broadly than bottom fixed turbines, but they are still in a relatively early stage of development. In this context, Norway is opening for offshore wind development in two areas, Sørlige Nordsjø II and Utsira Nord. In the future, offshore wind could contribute as a renewable energy source for oil and gas installations on the Norwegian Continental Shelf and its combination with offshore energy storage could represent an attractive solution to produce carbon neutral oil and gas.
In the project thesis, the candidates examined the state-of-the art on the topic, selected the site (Utsira High) and targeted Oil and Gas installation, the wind turbine (10MW), the number of FOWTs (four) required as basis for energy supply and a semi-submersible concept as floater type (OO-Star). Finally, they selected SIMA as time-domain simulation tool, and related frequency-domain and other needed numerical tools, and performed a preliminary frequency-domain analysis of the hydrodynamic coefficients using HydroD.

Objective
This master thesis aims to contribute to the study on the feasibility of a renewable-energy supply for an offshore oil and gas installation. The focus is on the analysis of survivability, operativity and energy production of a floating OW turbine (FOWT) to be used as supplier of an oil and gas installation. An important quest is on the possibilities to meet maximum (100%) of the annual power demand of the oil and gas installation with such offshore renewable energy supply.

The work should be carried out in steps as follows; some include part of the work done in the project thesis so to make the MSc thesis a stand-alone document:

1. Provide the background motivation and the state-of-the-art relevant for this topic, collect the information on the selected site, the oil and gas installation and related environmental conditions, provide the relevant information on the selected FOWT and

describe the selected prediction tool for studying its behaviour at sea. Base this on the material collected in the project work and complement it when needed.
2. Finalize the frequency-domain analysis, including numerical convergence study for one of the FOWT assumed as isolated and compare the properties (e.g. natural periods) against those expected.
3. Based on the site characteristics, on the targeted oil and gas installation and on the FOWTs mooring-line arrangements, examine and justify a set-up of the four FOWTs in terms of their absolute and relative location and orientation. In doing this choice, you should attempt that the FOWTs do not interact hydrodynamically with the installation and do not interact hydro and aero-dynamically with each other. As for the hydrodynamic interactions with each other, attempt to assess that they can be neglected in the analysis (e.g., examining the decay of radiated and diffracted waves associated to an isolated FOWT). As for their aerodynamic interactions, use available studies on wakes interactions for wind turbines as guidance to assess their importance.
4. Perform statistical analyses of the FOWTs in operational conditions when including linear and second-order hydrodynamic loads, using time-domain simulations and examine relevant response variables. If possible, examine also extreme conditions.
5. Based on the literature study performed in step 1, propose a wind farm layout design and examine the feasibility aspects of the proposed FOWT solution for energy supply.
6. Draw the conclusions from the studies and discuss possible further research steps.

The work may show to be more extensive than anticipated. Some topics may therefore be left out after discussion with the supervisor without any negative influence on the grading.

The candidate should in his report give a personal contribution to the solution of the problem formulated in this text. All assumptions and conclusions must be supported by mathematical models and/or references to physical effects in a logical manner.

The candidate should apply all available sources to find relevant literature and information on the actual problem.

The thesis should be organised in a rational manner to give a clear presentation of the work in terms of exposition of results, assessments, and conclusions. It is important that the text is well written and that tables and figures are used to support the verbal presentation. The thesis should be complete, but still as short as possible. In particular, the text should be brief and to the point, with a clear language. Telegraphic language should be avoided.

The thesis must contain the following elements: the text defining the scope (i.e. this text), preface (outlining project-work steps and acknowledgements), abstract (providing the summary), table of contents, main body of thesis, conclusions with recommendations for further work, list of symbols and acronyms, references and (optional) appendices. All figures, tables and equations shall be numerated.

The supervisor may require that the candidate, in an early stage of the work, present a written plan for the completion of the work. The plan should include budget for the use of computer and laboratory resources that will be charged to the department. Overruns shall be reported to the supervisor.

From the thesis it should be possible to identify the work carried out by the candidate and what has been found in the available literature. It is important to give references to the original source for theories and experimental results.

Supervisor : Marilena Greco
Co-supervisor : Claudio Lugni

Submitted : January 15th 2022
Deadline : June 11th 2022

Marilena Greco
Supervisor

Preface

This report concludes the Master of Science (MSc) degree of Subsea Technology under the department of Marine Technology at Norwegian University of Science and Technology (NTNU). The specialization of the Master thesis is Marine Hydrodynamics and was written in the spring of 2022. The authors' concern for hydrodynamics and offshore renewable energy were influential in the decision for the topic of the thesis.

During the fall of 2021, a project thesis was completed which consisted of preliminary studies and calculations for the Master thesis. The project thesis aimed to contribute to the study on the feasibility of a renewable-energy supply for an offshore O&G installation. The Master thesis extended the work carried out in the project thesis, but is more narrowly focused on the coupled time-domain analysis of the floater. The focus was on the analysis of the hydrodynamic behavior of a floating wind turbine substructure to be used as power supplier of an O&G installation. Learning how to utilize the modeling and analytic tools GeniE, HydroD, and SIMA took a significant amount of effort. However, the knowledge and abilities in the field of hydrodynamics have grown and the authors are greatful to have gained deeper insight into an interesting field of topic.

Lastly, we would like to inform the reader of our background which differs considerably from most candidates writing a master's thesis in marine hydrodynamics. In fact, both authors have their academic background from Oil and Gas technology. However, we have been fortunate enough to have guidance from various professors and fellow students at Tyholt to meet our goal.

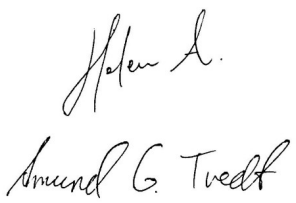

Helen Abraham
Amund Garsrud Tvedt
Trondheim, June 11, 2022

Acknowledgement

The authors would like to express our great appreciation to the main supervisor Marilena Greco, for the assistance provided throughout the year. The help and guidance provided every week and her willingness to give her time was appreciated.

Secondly, we wish to acknowledge the help provided by co-supervisor Claudio Lugni. The advice given throughout the master's thesis is appreciated.

Abstract

The feasibility of an offshore wind concept consisting of four floating wind turbines operating at a depth of 130 meters has been investigated. The OO Star Wind Floater consisting of a semi-submersible substructure supporting the 10 MW DTU reference wind turbine were analysed. The FWT are studied on the premise that they are aerodynamically and hydrodynamically independent of one another. After developing a numerical panel model in GeniE, the structure's hydrodynamic parameters were determined using first-order and second-order frequency domain analysis in HydroD. The numerical model was verified, and the findings of first-order frequency domain analysis were compared to the LIFES50+ project's results, which showed good agreement. The numerical models were verified using the results of HydroD's hydrodynamic analysis and free decay tests in SIMA. The verification, which was deemed adequate, compared mean drift forces, natural periods, and QTFs.

The properties acquired from the frequency domain analyses were then imported into SIMA, which was used to run time-domain simulations. The main goal was to investigate the FWT's behavior in operational and extreme conditions. Three different models were used to assess the numerical model's applicability, survivability, and operability under operational and extreme conditions. The models simulated in a coupled time-domain analysis were based on results from:

- First-order frequency domain analysis model (**1.M**).
- Second-order frequency domain analysis with wave drift damping calculated with wave loads calculated with Newman's approximation (**2.M**).
- Second-order frequency domain analysis with full QTF (**3.M**).

The results demonstrated the need of taking second-order effects into account when capturing low-frequency movements. Newman's approximations were shown to be quite accurate when compared to analyses using a full quadratic transfer function.

The maximum values of the mooring line tension were underestimated using linear potential theory compared to the full QTF model for load case 1.EX. The difference was 27.67 % for line 1, which experienced the largest tensions. In theory, this was due to the linear model not accounting for second-order effects in low-frequency motions, hence the second-order effects were determined to be particularly relevant to consider.

Lastly, three different layout concepts were presented which consisted of four FWTs, placed in different patterns. The layout concepts were based on a literature study, where aerodynamic wake effects were given a particular consideration. The selected layout concept presents the FWTs in a single row with a crosswind spacing distance of

4D. The design of the wind farm was based on the design of WindFloat Atlantic and the decision was based on the literature review conducted on requirements for prevention of wake interactions and placement of the turbines.

Sammendrag

En hydrodynamisk studie av en flytende vindturbin plassert i Nordsjøen på 130 meters dyp er utført. OO Star Wind Floater som består av en halvt nedsenkbar konstruksjon som støtter referansevindturbinen DTU 10 MW. Den flytende vindturbinen er studert med den forutsetning at de er aerodynamisk og hydrodynamisk uavhengige av hverandre. Etter å ha utviklet en numerisk panelmodell i GeniE, ble strukturens hydrodynamiske parametere bestemt ved bruk av førsteordens og andreordens frekvensdomeneanalyse i HydroD. Den numeriske modellen ble verifisert, og funnene fra førsteordens frekvensdomeneanalyse ble sammenlignet med LIFES50+-prosjektets resultater, som viste god samsvar.

Egenskapene hentet fra frekvensdomeneanalysene ble deretter importert til SIMA, som ble brukt til å kjøre tidsdomene-simuleringer. Hovedmålet var å undersøke FWTs oppførsel under operasjonelle og ekstreme forhold. Tre ulike modeller ble brukt for å vurdere de numeriske modellenes anvendelighet, overlevelsesevne og operabilitet under operasjonelle og ekstreme forhold. Modellene simulert i en koblet tidsdomeneanalyse var basert på resultater fra; førsteordens frekvensdomeneanalysemodell, andreordens frekvensdomeneanalyse med Newmans tilnærming for å løse bølgedempning og andre-ordens frekvensdomeneanalyse med full QTF.

Resultatene demonstrerte behovet for å ta hensyn til andre-ordens effekter når man fanger lavfrekvente bevegelser. Newmans tilnærming ble vist å være tilstrekkelig, sammenlignet med analyser ved bruk av en differanse-frekvense full QTF.

De maksimale verdiene for fortøyningslinespenningen ble underestimert ved bruk av lineær potensialteori sammenlignet med den fullstendige QTF-modellen for load case 1.EX. Forskjellen var 27.67 % for linje 1, som opplevde de største spenningene. I teorien skyldtes dette at den lineære modellen ikke tok hensyn til andre-ordens effekter i lavfrekvente bevegelser.

Til slutt ble det presentert tre forskjellige layoutkonsepter som besto av fire FWT-er, plassert i forskjellige mønstre. Konseptene var basert på en litteraturstudie hvor aerodynamiske wake-effekter ble tatt spesielt hensyn til. Det foretrukne layoutkonseptet presenterer FWT-ene i en enkel rad, med en sidevindsavstand på 4D. Utformingen av vindparken var basert på designet til WindFloat Atlantic og beslutningen var basert på litteraturgjennomgangen foretatt om krav til forebygging av wake-interaksjoner og plassering av turbinene.

Contents

List of Figures

List of Tables

Nomenclature

Abbreviations

BEM Blade Element Momentum

CAGR Compound Annual Growth Rate

DoF Degree of Freedom

FEM Finite Element Method

FOW Floating Offshore Wind

FWT Floating Wind Turbine

GDW Generalized Dynamic Wake Method

GHG Green House Gases

HVAC High Voltage Alternating Current

HVAC High Voltage Direct Current

JONSWAP Joint North Sea Wave Project

LCOE Levelized Cost of Electricity

NCS Norwegian Continental Shelf

O&G Oil and Gas

QTF Quadratic Transfer Function

RAO Response Amplitude Operator

rpm Rotations per minute

WADAM Wave Analysis by Diffraction and Morison Theory

WTG Wind turbine generator

Greek Letters

ϵ Phase angle

η Body Response

λ Wave length

ω Wave frequency

ρ Density

ζ Wave elevation

Other symbols

C_D Drag coefficient

C_M Mass coefficient

D Diameter

g Gravitational acceleration

p Pressure

R Radius

U Velocity

1 Introduction

The Norwegian oil and gas industry intends to achieve a 40% reduction in its absolute GHG emissions within 2030 and near zero by 2050 (KonKraft 2020-1). This climate strategy was recently initiated through electrification of oil and gas installations on the Norwegian continental shelf (NCS). The electrical power available is transported by long distance power cables from shore, which sparked interest in the offshore wind industry. Floating offshore wind (FOW) would provide power locally and contributing to the technological enhancement of marine renewable energy.

The petroleum industry is a key contributor to climate change due to obvious implications. Thus, the Norwegian petroleum companies are at the vanguard of climate debate by public demand to contribute resourcefully to sustainable power production. Beyond the initial phase of reducing the petroleum companies' annual CO_2 equivalent emissions, the North Sea has a promising potential to ascertain a key part in the development of the offshore wind value chain industry.

The main objectives of this master's thesis is to provide a feasibility study of a renewable energy supply for an offshore O&G installation in the North Sea. The focus being numerical analysis of survivability, operativity and power production of a floating offshore wind farm to supply an offshore oil and gas installation.

1.1 Background

The European commission has an ambition of increasing Europe's offshore wind capacity from its current level of 12 GW to 300 GW by 2050 (2020). The aim is to meet European Union's goals of climate neutrality in the same time frame. This expansion will be accommodated by state-of-the-art emerging technologies and contributions to the job market across the continent.

The Norwegian government announced in June 2020 that two locations would be opened for development of offshore wind, in accordance with the electrification plan and the increase interest in offshore wind (2020). The areas, Utsira Nord and Sørlig Nordsjø II, were officially opened for application of concession on January 1st, 2021.

In recent years, bottom-fixed wind turbines are rarely used in areas deeper than 60 meters (H. Song et al. 2012). The area of Utsira Nord's water depth ranges from 220 to 280 meters, suggesting that floating offshore wind is most suitable. Due to the costly development of FOW turbines, the Norwegian government has expressed their intention of providing finical funding for projects on Utsira Nord in service of incentivizing private energy companies (2020).

Floating offshore wind has created opportunities for the extraction of renewable energy in considerably larger areas than conventional bottom-fixed wind turbines could. The development of floating offshore wind turbines is an undertaking. Nonetheless, researching the possibility of a hybrid system consisting of energy supply in loco and energy storage presents a unique field of interesting challenges.

1.1.1 Summary of Preliminary Studies

The project thesis was carried out during the fall semester of the academic year 2021/2022 as a preliminary presentation for this master's thesis. The projects contributed to the feasibility study of a renewable-energy supply for an offshore O&G installation. The focus was on the analysis of the hydrodynamic behavior of a floating wind turbine with a semi-submersible substructure. The selected offshore site was in the North Sea, near a suitable O&G installation in actively production at a water depth of 130 m. The project thesis was in collaboration with Lundin Energy Norway. It was intended to continue throughout the master's thesis, however this was not the case.

Through a though literature study a substructure and turbine size was selected, namely the OO Star 10 MW by Dr.Tech Olav Olsen. The wind farm would consist of 4x10 MW turbines to directly supply the power to the installation. The suitability of a semi-submersible substructure was determined by geometry, dimensions and environmental conditions. The environmental conditions were provided by a Norwegian Energy company from an O&G platform with the intentions of implementation in the coupled analysis.

A numerical model was developed via panel model and preliminary first-order frequency domain analysis was performed to obtain the hydrodynamic properties of the floating structure. The hydrodynamic loads and response in waves were analyzed though first-order frequency domain. Thereby, the added mass and damping displayed satisfactory agreement with the reference values from the LIFES50+ project (Pegalajar-Jurado et al. 2018).

Furthermore, a background study on the following aspects was performed:

- State-of-the-art theoretical, numerical, and experimental research.
- Industrial development relevant for the thesis.
- Active and planned projects for FOW substructures.
- Methodology of a fully coupled time-domain analysis in SIMA.

The thesis project was for the most part research based for the upcoming semester. The aim was to be familiarized with the numerical tools required to conduct a complete study. Due to lack of expertise and experience with HydroD and SIMA, this was no easy task. Nonetheless, by formulating a comprehensive methodology and completing first-order frequency domain analysis said task become feasible.

1.1.2 Current State of Offshore Wind Industry

Wind resources have been used for energy production since the late 1800s; offshore wind is a rather recent phenomenon (Johansen 2021). The first offshore wind farm was built off the coast of Denmark in 1991, consisting of 11 turbines with a total installed capacity of 5 MW (Shahan et al. 2014). Ever since, the offshore wind industry has made an increasing contribution to global energy consumption. According to the Global Wind Energy Council's (GWEC) report from 2021, the historic development of total installations (GW) had increased by 4.5 % from 2019 to 2020 (2021). This historical growth has become a part of a larger plan for various countries to achieve net zero by continuously investing in renewable energy. European countries have been at the forefront of the offshore wind industry's development with several offshore wind farms situated off the coast of Europe.

The general global outlook of the offshore wind industry is encouraging. The industry has all the indications of becoming a formidable contender in the future energy market. NORWEP's annual market report Global Offshore Wind 2020 points to an expected cumulative global growth of 76 GW until 2025 (2021). Figure 1.1 depicts the historical development of total installations (GW) with the compound annual growth rate (CAGR) for onshore and offshore wind turbines.

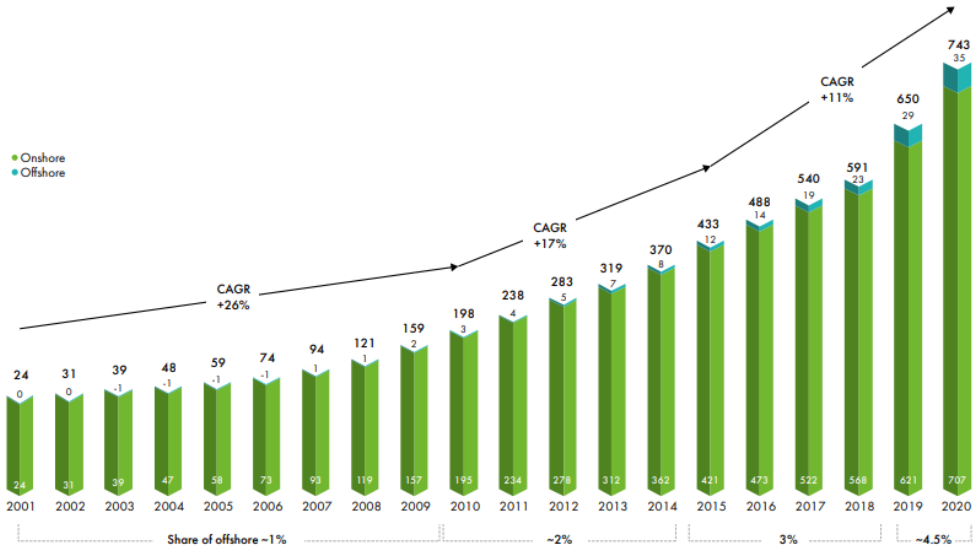

Figure 1.1: Market status of the historic development of total wind turbines.

The North Sea is a geographical area with considerable wind resource potential. The figure (1.2) below displays the mean annual wind speed, and as previously noted the northern European seas have large potential wind resources with the highest mean annual wind speeds (Rodrigues et al. 2015). Beyond the offshore petroleum expertise, these characteristics have allowed northern European countries to take the lead in this venture.

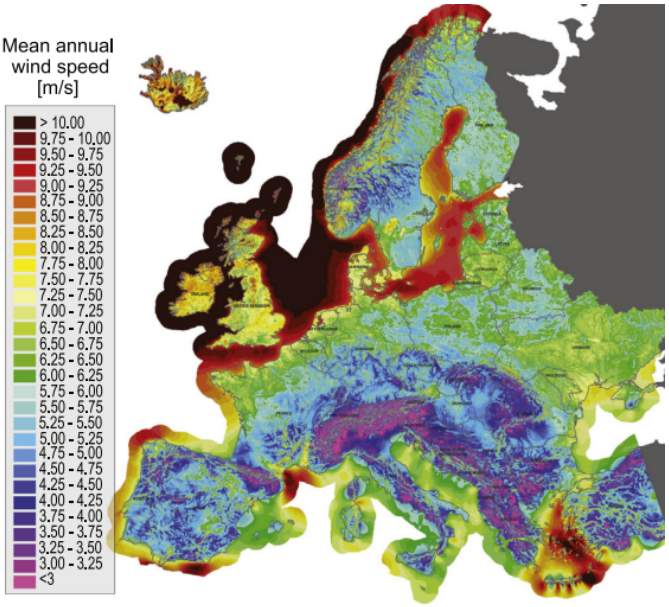

Figure 1.2: Annual European onshore and offshore mean wind speeds at an 80 m height.

Coelingh et al. (1996) conducted studies in the late 90s from multiple O&G platforms and the results clearly state that the wind speed increases by increasing distance from the coasts (Coelingh et al. 1996). Thus, turbines sizes have been scaled up over recent years to complement the offshore environmental conditions.

1.2 Feasibility of Floating Wind Turbines

In the past, the offshore wind industry has largely utilized fixed substructures to the seabed. The dominating substructures were monopile and jacket foundations due to their cost effective and certified functionalities. The O&G industry in Norway has vast knowledge of technological advancement in deep waters. Hence, they have been instrumental in the development of various foundation concepts to ensure durability and operativity over the years. Nonetheless, bottom-fixed foundations have their structural restrictions and are confined to water depths below 60 meters (H. Song et al. 2012).

The necessity for floating substructures was driven by the possibility of generating wind energy at greater water depths and higher installed capacity. A great portion of Europe's coastal areas have a water depth of above 60 meters, especially the North Sea. Due to the wind industry's desire for commercial market for FWTs, offshore wind has moved into deeper waters recently.

The development of FWTs has come far since the early 2000's. However, the market is still far from commercial due to economic constraints and government regulations. The world's first commercial floating wind farm was installed in 2017 by Equinor off the coast of Scotland, with a total installed capacity of 30 MW. Hywind Scotland consists of 5x6 MW turbines with spar substructure and suction anchors on the seabed at a water depth ranging from 95 to 120 m (Equinor 2019a).

The latest milestones in FWT development are mentioned in the following:

- Hywind Tampen: The world's first floating wind farm supplying power to five O&G installations consisting of 11x8.6 MW turbines with spar substructures, owed by Equinor and their partners. This project is located on the Norwegian North Sea (Equinor 2019b). The water depth of the wind farm ranges from 260 m to 300 m.
- WindFloat Atlantic: The floating wind farm is located off the coast of Portugal consisting of 3x8.4 MW turbines with semi-submersible substructures at water depth 100 m. The wind farm has been fully operational and supplying the Portuguese electrical grid since late July of 2020. This project was sponsored by Ocean Winds, Repsol and Principle Power (Principle-Power 2019).
- EOLMED Project: The floating wind farm is to be located in the Mediterranean Sea, off the coast of Gruissan, France and consisting of 3x10 MW turbines with barge substructures. The wind turbines were fully constructed early 2022 and expected to be operational in 2023. This project is sponsored by the French government, BW Ideol and EOLMED. The selected site for the wind farm has a water depth of 55 m (BW-Ideol 2021).

The OO Star 10 MW Wind Floater is a floating turbine with a substructure of a semi-submersible designed by Dr. Tech Olav Olsen and selected for the LIFES50+ project (2018). This wind turbine has been well researched by various world class research facilities. Thus, it has been selected to be the substructure element of this study.

1.3 Scope of Thesis

The master thesis is a continuation of the project work from the previous semester. The thesis aims to perform a hydrodynamic analysis of the OO Star 10 MW wind floater at a water depth of 130 m. The scope of this thesis will be to investigate the hydrodynamic behavioral characteristics of the FWT under operational and extreme conditions and perform a comparison of the response features to the LIFES50+ project, when possible.

Proceeding from the preliminary literature study of the state-of-the-art FWTs and related studies, possible inquire factors could be:

- Second-order effects.
- Aerodynamic interactions, wake effects,
- Load cases under operational and extreme conditions.
- Wind farm layout design.

Figure 1.3 illustrates the workflow of the master thesis.

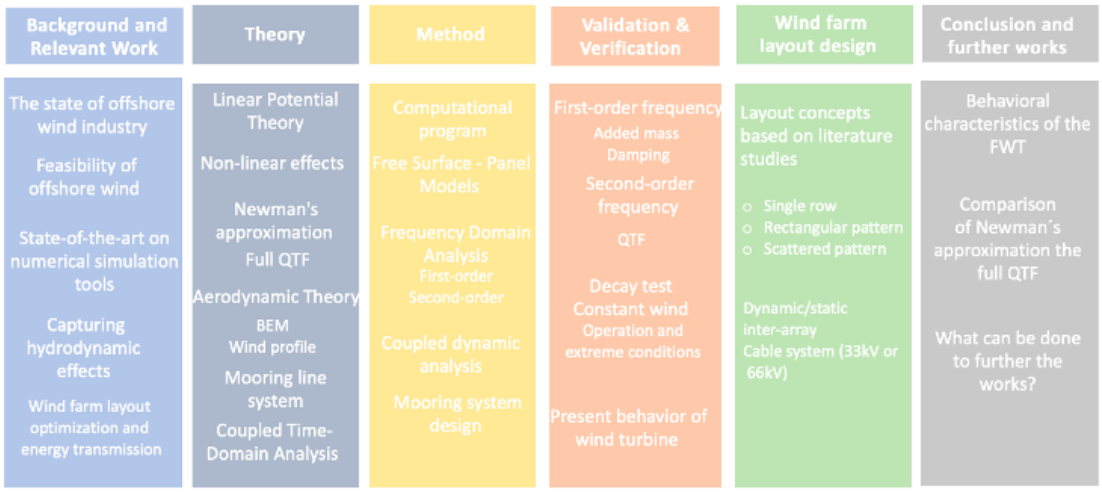

Figure 1.3: Workflow of Master thesis

1.4 Structure of Thesis

The structure of the master thesis is as follows:

- Chapter 2 - Provides a state-of-the-art literature review on numerical analysis of floating wind turbines, second-order effects and heave plate effects. In addition, a literature study was conducted on wind farm layout optimization in connection with aerodynamic interactions.
- Chapter 3 - Consists of the theoretical background deemed necessary for the numerical simulations. The utilized theory in hydrodynamics, aerodynamics and time-domain analysis are presented accordingly.
- Chapter 4 - Contains a fairly detailed description of the FWT concept selected for this thesis. The OO Star wind floater is presented with its structural properties, wind turbine dimensions and mooring line system.
- Chapter 5 - Provides the wind farm location considered with corresponding environmental conditions, along with the load cases used in time-domain simulations.
- Chapter 6 - Consists of a descriptive methodology including software usage, the design process of numerical model based on theoretical background covered in Chapter 3.
- Chapter 7 - Contains verification of the numerical model based on first-order, second-order frequency domain analysis, decay test and wind turbine performance. The findings are provided in the form of graphs and tables, followed by a discussion.
- Chapter 8 - Provides a study of the numerical model in operation and extreme conditions. Presentation of FWTs motion response, aerodynamic-, hydrodynamic loads and mooring line tensions.

- Chapter 9 - Consists of wind farm design based on literature studies covered in Chapter 2 and presents three layout concepts followed by a discussion.
- Chapter 10 - Concludes this master's thesis and recommendations for future works are given.

2 Literature Study

A literature study was carried out to acquire material regarding previous work related to floating wind turbines. Additionally, relevant hydrodynamic effects deemed important were included.

2.1 Research Studies

In the initial stages of FWT development (early 2000s), numerical modelling and analysis was performed in frequency domain. This method of conducting a study is frequently used in the offshore O&G industry to determine the floating structure response to incoming waves (Chuang et al. 2020). However, recent studies of FWTs consider important coupling effects between the tower, controller, mooring-lines, aerodynamics, and hydrodynamics that are not accounted for in frequency-domain analyses. Therefore, when designing FWTs with state-of-the-art numerical tools, the methods are integrated aero-hydro-servo-elastic analyses based on coupled time-domain analysis. Considerable amount of progress has been made to compare, validate, and improve these tools so that engineers may create more cost-effective and robust FWTs (E. E. Bachynski and Eliassen 2019).

LIFES50+ was a European Horizon-2020-funded programme, led by SINTEF Ocean. The research programme was a consortium with 12 partners, which began in June 2015 and adjourned in April 2019. The goals of the research program were to develop next generation substructures for large floating offshore wind turbines (10 MW) and contribute to the development of hybrid model testing procedures for FWTs (Thys, Fontanella, et al. 2019). The project met its goals by delivering two optimized, innovative substructure designs for 10 MW turbines that were qualified to technology readiness levels (TRL) 5 through experimental validation in a relevant environment (Bayati et al. 2016). The OO Star 10 MW Wind Floater was one of the substructure designs analyzed in this study.

FLAGSHIPS (2021) is a research project where the goal is to design, manufacture, install and test an OO Star, supporting an 11 MW turbine at the MetCentre demonstration site west of Karmøy, Norway. The floater will be built and assembled with the tower and wind turbine generator (WTG) on the west coast of Norway. Prior to towing the complete OO Star unit (including tower/WTG) from shore to the MetCentre offshore location, the mooring and export cable will be pre-installed. The OO-Star will be linked up to the pre-laid mooring lines and the cable will be brought in through a j-tube when it arrives at the location. The FLAGSHIP project is a natural extension of the LIFES50+ H2020 initiative.

Another research project regarding design of FWTs and verification and validation of numerical codes includes the WINDMOOR project (Silva de Souza, Berthelsen, et al. 2021). WINDMOOR is a four-year Competence Development Project supported by the Norwegian Research Council and industry partners, which began in 2019. The project's main objective is to gain a comprehensive understanding regarding the loads that influence the design of floating wind turbine mooring systems.

The scope of the study included:

- Validation of low-frequency hydrodynamic models.
- Gain an insight of atmospheric stability and turbine aerodynamic interaction.
- Global examination of FWTs in farm formation, with a focus on mooring lines.

The project describes the INO WINDMOOR 12 MW base case floating wind turbine, and an aero-hydro-servo-elastic model implemented in SIMA, a combination of SIMO and RIFLEX. The wind turbine is installed on a floating platform designed jointly by Inocean and Equinor. The floating platform consists of a steel semi-submersible platform with three columns, connected by pontoons and deck beams.

2.1.1 Numerical Software

Borg and Bredmose (2015) gives an overview of the most prevalent numerical tools used by consortium partners for FWT design and verification. The partners in LIFES50+ commonly utilize the open-source integrated numerical tool FAST, developed by National Renewable Energy Laboratory (NREL) for their aero-hydro-servo-elastic simulations. For aerodynamics, the blade element momentum method (BEM) or generalized dynamic wake method (GDW) can be implemented in FAST. Large-volume or slender structures are implemented in the hydrodynamic force models from ANSYS AQWA or WAMIT (Borg and Bredmose 2015).

SIMA is another common numerical tool for aero-hydro-servo-elastic coupled time-domain simulations. SIMA was developed by SINTEF Ocean and has been used for coupled time-domain simulations by partners in the LIFES50+ consortium and this master thesis. SIMA supports the complete process of a marine simulation, from the definition of the simulation, the execution and post-processing of results. The program is an integrated simulation workbench designed for analyses of marine operations and floating systems. SIMA workbench includes the numerical codes SIMO and RIFLEX, which is used for coupled analyses of floating platforms. When analyzing and simulating a FWT in SIMA, the blades, turbine, and control system can be specified in the program or be given via link to an external program. The mooring system can be defined in SIMA and the hydrodynamics of the floating foundation can be read from general hydrodynamic analysis programs (i.e., HydroD). A time domain analysis by a fully coupled method can analyze the complete floating system with mooring lines. Aerodynamics are implemented by BEM including a correction for dynamic wakes (Wei Yu et al. 2018). The coupled dynamics are calculated by a non-linear finite element method (FEM) analysis in RIFLEX (Atcheson et al. 2016). The frequency domain analysis in this master thesis was performed using WADAM, which is a part of the DNV software HydroD.

Computational capacity is among the most paramount challenges facing design codes today. To execute the coupled analysis, several programs are assembled under the same workbench. Lack of effective communication between the different programs can lead to extensive simulations span (Michael Borg and Collu 2015).

2.1.2 Verification

The LIFES50+ consortium has verified the numerical models for aerodynamics and structural dynamics analysis by testing a spar- and semi-submersible type of floating wind turbine (Wei Yu et al. 2018). Furthermore, verification of numerical tools employed FWT analyses, has been the focus of several other research programs:

- Offshore Code Comparison Collaboration (OC3) (Jason Jonkman and Musial 2010).
- Offshore Code Comparison Collaboration Continuation (OC4) (A. Robertson et al. 2014).
- INNWIND.EU (Azcona et al. 2013).

The OC3 (Offshore Code Comparison Collaboration) – OC6 projects (Offshore Code Comparison Collaboration, Continued with Correlation, and uncertainty) were developed as part of the International Energy Agency's (IEA) Wind initiative to meet the requirement for load predictions using coupled modeling tools for offshore wind design to be verified and validated (Amu N Robertson et al. 2020). The OC3 and OC4 projects intended to verify that the numerical codes used in FWT analysis were accurate and proper in a code-to-code way. The analyses covered a wide range of offshore wind turbines from semi-submersibles, spar-buoys, monopiles, jackets to tripods where different codes were tested.

The INNWIND.EU provided verification of numerical codes by code-to-code analyses and validation by comparison with experimental model tests. The main objectives of the INNWIND.EU project was to develop a high-performance, innovative design for a 10-20 MW FWT beyond state-of-the-art, including hardware demonstrations of the critical components (2017). These research projects provided verification of the numerical tools used in the LIFES50+ studies.

2.1.3 Validation

Validation of numerical tools utilized in analyses of FWTs have been performed by comparison of experimental model tests. The Offshore Code Comparison Collaboration Continuation, with Correlation (OC5) (2017), the INNWIND.EU (2013) and LIFES50+ (2016) projects have performed validation studies of the numerical codes.

The OC5 project (2017) compared numerical analysis to a model test of a semi-submersible in a wave basin under combined Froude-scaled wind and wave loads. The goal of this study was to validate the modeling tools for offshore wind systems by comparing simulated responses of various system designs to physical experimental data. The numerical models of the DeepCwind floating semi-submersible were validated by performing results comparison to a $1/50^{\text{th}}$- scale model at Maritime Research Institute Netherlands offshore wave basin. Following the calibration using free-decay, wind-only, and wave-only testing, the models were validated by comparing calculated ultimate and fatigue loads for eight different wave-only and combination wind/wave test cases against measured data. The results displayed that non-linear wave excitation forces were underestimated, and it was concluded that hydrodynamic properties causing non-linear wave forces should be included in numerical codes.

Borisade et al. (2018) conducted a study, which was part of the INNWIND.EU (2013) project, where the purpose was to verify and validate existing numerical codes for floating offshore wind turbine structures using wave tank model experiments. In a combined wind-and-wave basin, a model of the OC4 DeepCwind semi-submersible platform was tested beside a Froude-scaled rotor model. A multibody technique incorporating hydrodynamic and aerodynamic loads and mooring line forces were used in the modeling environment. The validation of the hydrodynamics of a modified model hull shape compensating for the additional mass of the nacelle was the topic of this paper. The results revealed that the simulation model and the experiment were in good agreement.

Bayati et al. (2016) describes the first set of data from the LIFES50+ project's steady and unsteady wind tunnel tests, which were conducted at the Politecnico di Milano wind tunnel on a $1/75^{\text{th}}$- rigid scale model of the DTU 10 MW wind turbine. The purpose of those tests was to validate the open-source code AeroDyn, which was developed by NREL. In terms of thrust and torque coefficients, numerical and experimental results showed good agreement. Satisfactory results were again shown for the unsteady measurements collected with a two-degree-of-freedom test rig capable of imposing displacements at the model's base and providing surge and pitch motion of the FOWT scale model. Supplementary to the wind tunnel test developed at Politecnico di Milano (POLIMI), SINTEF Ocean developed a method for tests in an ocean basin (Thys, Fontanella, et al. 2019). Since one of the goals of the LIFES50+ project was to contribute to the development of hybrid model testing procedures for FWTs, Real-Time Hybrid Model test was performed. There will normally be a physical and a numerical substructure for real-time hybrid model testing of FWTs. One of the substructures will be used to simulate the system's hydrodynamics, while the other will be used to represent the system's aerodynamics.

Thys, Chabaud, et al. (2018) performed Real-Time Hybrid Model tests to reach beyond the limits of performing model tests with wind and waves. The model and waves were physical in the experiments, while the tower and rotor loads were computed in real-time using FAST and applied to the model via a horizontal cable driven parallel robot as illustrated in Figure 2.1 (2019). To gain insight into the breakdown of the effects of wave and wind loads, the test program with irregular waves and turbulent wind included tests with wave only, wind only, and wind and wave combined. In the presence of wind and waves, the low frequency surge response was reduced compared to waves alone.

The wind had minuscule effect on the surge and pitch response in the wave frequency zone. The pitch period changed with wind conditions and was caused by the wind turbine controller, surge coupling and mooring system (due to different mean offset). Gravity loads dominated the low frequency loads near the base of the tower due to pitch motions. Furthermore, it was discovered that wind turbulence influenced the surge and pitch responses at low frequencies.

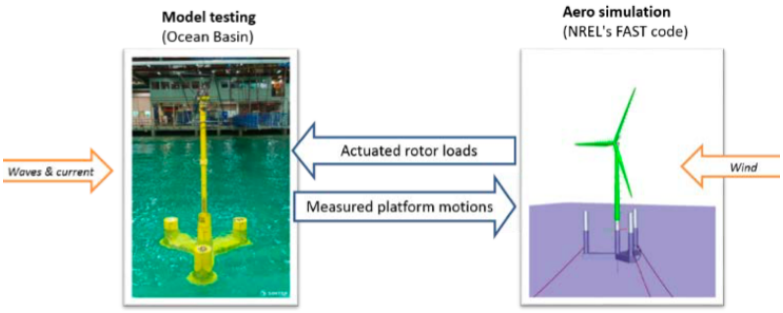

Figure 2.1: Setup of the hybrid tests in the ocean basin at SINTEF Ocean

Silva de Souza, Fonseca, et al. (2021) focused on the surge low-frequency motions and offers a hydrodynamic modeling technique and calibration procedure for the INO WINDMOOR 12 MW semi-submersible floating wind turbine. Model experiments were conducted in a variety of sea states, a platform hydrodynamic model was constructed and implemented in SIMA. The numerical model incorporated the wave drift coefficients acquired from the experiments. The combination of linear and quadratic terms was then assumed for low-frequency damping. WAMIT was used to determine added mass, damping, first- and second-order excitation in a potential flow study. Only the wave drift loads were computed for the second-order excitation, resulting in the usage of Newman's approximation as a quadratic transfer function. The numerical model's results closely matched the experimental data, and the most significant difference was found in the low frequency pitch motion. The empirical wave drift coefficients were larger than the WAMIT values and this difference was especially apparent at lower frequencies.

The results of the validation studies were not as successful as the verification of the codes. However, the studies demonstrated that validation was effective in many situations, especially through real-time hybrid tests. Furthermore, to build more inventive and cost-effective FWT systems, it will be necessary to improve experimental methodologies and include second-order effects into numerical codes.

2.2 Second-Order Effects

Through several mid-fidelity engineering models, including the OpenFAST tool developed by the National Renewable Energy Laboratory (NREL), Wang et al. (2022) noticed a continuous underprediction of the nonlinear, low-frequency responses of an offshore wind semi-submersible in the OC5 and OC6 projects. Severe underpredictions were observed from the low-frequency wave excitation in surge, pitch, and the resulting resonance motions. The authors improved the predictions of low-frequency wave loads and responses by making various changes to the OpenFAST model from the OC5/6 studies. All these changes were in the viscous drag force modeling. The recommended solutions improved the predictions of low-frequency surge, pitch wave loads on a fixed floater, and the resonance responses of a floating structure. The results were in good agreement with observations from the OC6 wave-basin experimental investigations.

Duarte et al. (2014) incorporated the second-order hydrodynamic loads in FAST with the quadratic transfer functions (QTF), and conducted a spectral analysis of the impact of second-order wave loads on the FWT OC3-Hywind. For the spectral analysis, four load cases were selected: two under operational conditions, one load case under extreme condition, and last load case under parked turbines condition with regular wind and sea state. The study consisted of first-order, Newman's approximation, difference-frequency full QTF, sum-frequency full QTF, and complete second-order analysis.

According to the results from the analyses without wind loads, Newman's approximation and sum-frequency underestimated the motions in surge, pitch and fairlead tension within their natural frequencies range as shown in Figure 2.2a. Due to the absent effect of second-order excitation forces during the simulation of operational conditions, the surge motion was dominated by wind loads. However, the difference-frequency effected the pitch motion, and the Newman's approximation underestimated the loads within the natural frequency range. The influence of second-order loads was apparent for surge and pitch motion, and fairlead tension for extreme wave loads, since Newman's approximation underestimates the effects within natural frequencies once more as displayed in Figure 2.2b.

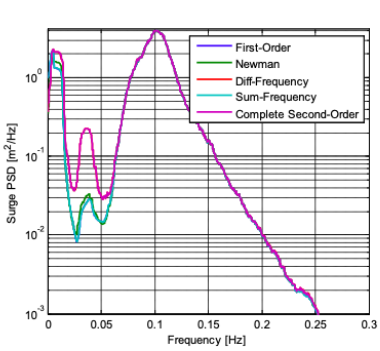

(a) Without wind loads

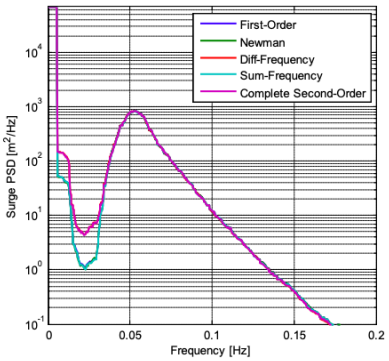

(b) With wind loads and extreme sea state.

Figure 2.2: Power spectral density of surge motion

A hydrodynamic analysis of three different semi-submersible FWTs, including second-order hydrodynamic effects was carried out by Zhang et al. (2020). It was conducted research investigations on a V-shaped semi-submersible, a braceless semi-submersible and the OC4-DeepCwind semi-submersible platform. The substructures were used to support the NREL 5 MW reference wind turbine. The primary objectives of this research were to analyze and evaluate the hydrodynamic responses of the three distinct semi-submersible floaters in two different water depths (100 m and 200 m) under several load conditions. The second-order wave loads effects on platform motions, mooring tension were investigated and compared by a variety of methodologies, including Newman´s approximation and full QTF (Quadratic transfer function). Additionally, the drag influence on the structural motion response was considered. When the Morison drag effect on the semi-submersible FWT column is neglected, the dynamic response of the floater is overestimated, and this was apparent in the results. The resonance of motion, especially for platform-pitch motion can be excited by second-order difference wave loads, which can lead to structural problems. To better replicate the realistic dynamic response of semi-submersible FWT, the full QTF approach should be employed to determine the second-order wave force.

Simos et al. (2018) investigated the second-order hydrodynamics of a semi-submersible FWT by assessing and proposing several options for calculating slow-drift motions during the design process. The case study consisted of experimental model tests and numerical model tests performed in WAMIT, neglecting aerodynamic loads. The study conducted experimental decay tests, experimental, numerical first-order, and second-order analysis in regular, irregular and bichromatic waves. From the tests; RAOs, mean drift forces, QTFs and response spectra were all obtained. The Slow-drift motions were calculated by WAMIT, using full second-order QTF. Both Newman's approximation and the white noise approach were computed and compared to the full QTF method. The mean, slow-drift movements and forces were studied and the results from experiments and models were compared. The white noise model retained the primary physics whereas the Newman's approximation underestimated the second-order response in some circumstances.

2.3 Heave Plate Effects

Two features are often introduced in the design of semi-submersible FWTs for reducing motions in waves; firstly, increasing the natural periods of motions in the vertical plane (associated with the floater's heave, roll and pitch motions). secondly, enlarging the hydrodynamic viscous damping related to these motions. Heave-plates can achieve both goals and as a result, this option has become typical for FWT designs with semi-submersible hulls, particularly for those without the use of horizontal pontoons (Mello et al. 2021).

Due to the substantial nonlinear nature of the heave plate problem and the importance of viscous forces, experiments and numerical calculations are required to estimate the added mass and damping. Heave plates are commonly used in the O&G industry and are favored in the design of FWT support structures, so several studies have been conducted on the subject. Experimental and numerical studies were undertaken throughout the development of the spar and semi-submersible FWT concepts to assess the effects of heave plates in terms of added mass, viscous damping, and the Keulegan-Carpenter (KC) number.

The non-dimensional parameters, Keulegan-Carpenter (KC) number and β are important parameters used in design of heave plates:

$$KC = \frac{2\pi\eta_3}{D_{hp}} \tag{2.1}$$

$$\beta = \frac{D_{hp}^2 f}{\nu} \tag{2.2}$$

where η_3 is the heave amplitude of oscillation, D_{hp} the diameter of the heave plate, f the frequency of oscillation and ν the kinematic viscosity. The Reynolds number can be defined as:

$$Re = KC \cdot \beta \tag{2.3}$$

The plate thickness-diameter ratio, the ratio between the diameters of the heave plate and the column it is attached to, the porosity, the oscillation amplitude and frequency are all factors that affect the hydrodynamic properties of a heave plate. Tao and Cai (2004) and Tao and Thiagarajan (2003), presents numerical calculations on a single column with a circular heave plate linked to the keel. The thickness-to-diameter ratio of the plate influenced the generation of vortices in regards for a very thin heave plate, the two edges operate as one sharp edge, resulting in a different flow field than for a thicker plate. Due to viscous effects, the experiments revealed a tendency of increased added mass and damping for decreasing thickness-diameter ratios, especially for low ratios and the viscous damping were the most affected. Furthermore, because less water was captured by the column connected to the heave plate, the impact of the heave plate on the column side was reduced, decreasing the added mass.

Lopez-Pavon and Souto-Iglesias (2015) investigated a design that consisted of three vertical columns connected by braces, each with a heave plate at the bottom. The experiments were limited to an isolated vertical column with an attached heave plate, disregarding any possible coupling with the braced structure. For a range of frequencies and KC-numbers, the authors compared results from an experimental study, a first-order WADAM analysis, and a CFD analysis. Figure 2.3 presents the added mass and damping coefficients for a plain disc configuration. The hydrodynamic coefficients are expressed in terms of added mass and damping in comparison to the theoretical added mass for the combined cylinder-plate-structure. The results showed that the coefficients are highly influenced by the KC-numbers, whereas the frequency has only a slight impact.

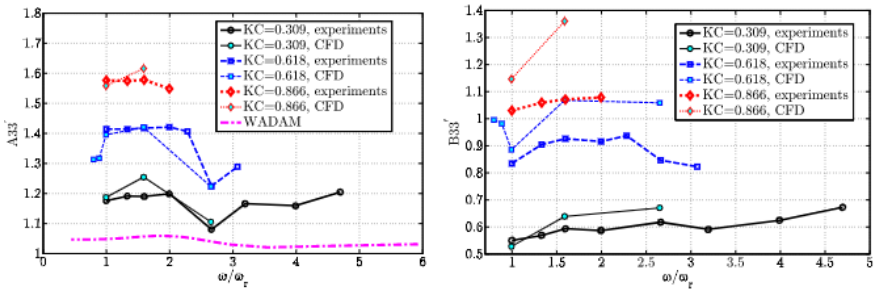

Figure 2.3: Added mass and damping coefficients for a plain disc configuration

Mello et al. (2021) published a set of results on the impact of heave plates with large skirts on the motions of a semi-submersible FWT. The heave plates were modeled using dipole panels, and the motions were computed in the frequency domain using a panel algorithm in WAMIT. The numerical predictions were compared against experimental results from model testing that consisted of decay tests, regular and white-noise waves. The results verified that modifications of plate diameter and skirt height caused significant changes in the floater's motions in waves, implying a parametric optimization of these variables could be a useful tool for hull design. A conventional frequency domain analysis could be used to obtain a reasonable prediction of first-order motions, however the results revealed that when considering mooring stiffness for pitch (or roll) motions as cancellation points in numerical RAOs, special precautions must be exercised due to viscous drag effects that can impose significant discrepancies on this range. According to the results for these set of heave plates investigated, although plate width was the dominant dimension in terms of added masses and viscous damping, variations in skirt height can contribute to fine tuning of the motions. Figure 2.4 shows the numerical RAOs in heave and pitch for each heave plate.

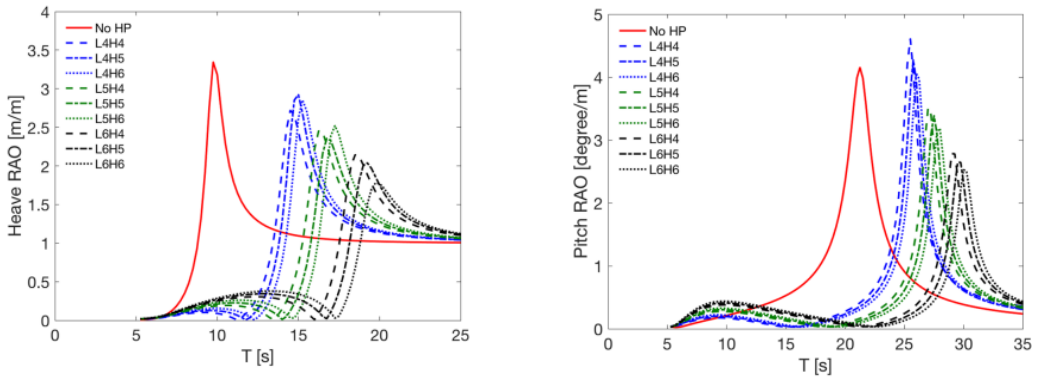

(a) Numerical heave RAOs

(b) Numerical pitch RAOs

Figure 2.4: Numerical RAOs for each heave plate

2.4 Wind Farm Layout Optimization

The layout design of a wind farm is an important aspect since it has a substantial impact on the project's profitability. The wind farm layout concept is ideally developed with the aim of minimizing the LCOE. However, for practical reasoning the layout design is required to follow certain rules and guidelines. These rules and guidelines are derived from international standards or site-specific regulations. They are constructed to improve safety, reduce environmental impart and with respect to marine traffic.

2.4.1 Aerodynamic Interaction

When energy is extracted from the air passing through a wind turbine, the properties of the air change. In addition to a decrease in wind velocity, the turbulence intensity of the air behind the rotor increases. This phenomenon is called the wake effect, and the wake region is the influenced area behind the turbine (Herbert-Acero et al. 2014).

Wakes that influence downstream turbines reduce wind potential, resulting in a wind farm's overall power loss. According to Sanderse et al. (2011), the power loss of a downstream turbine under full-wake conditions can exceed 40 %, depending on the layout and wind conditions of a wind farm. When averaged over different wind directions, onshore farms suffer losses of approximately 8 %, whereas offshore farms suffer losses of about 12 %. The wake loss is larger at wind speeds between the cut-in and rated wind velocity for a wind turbine. Furthermore, wakes can lead to fatigue stresses, resulting in higher operation and maintenance expenses causing a shorter lifespan for the wind turbines. Hence, one of the most essential elements in reducing power losses over the lifetime of a wind farm, is to optimize the position of turbines inside the wind farm in relation to wake effects (Herbert-Acero et al. 2014).

The near and far wake regions of a wind turbine's wake may be distinguished, however the transition between the regions is gradual (Vermeer et al. 2003). The length of the regions can be estimated in numerous ways. According to Herbert-Acero et al. (2014), the far wake zone typically begins between three and four times the rotor diameter (3D and 4D) downstream of a wind turbine. The length-extent of the wake, which is dependent on local air conditions, is used to calculate this distance. Several turbulence factors need to be included in models characterizing the near wake area and this is computationally intensive. To represent the far wake area, different modeling methodologies have been developed:

- CFD models based on Reynolds-Averaged Navier-Stokes equations or Large Eddy Simulations are utilized. They are effective tools for simulating the complex wind environment of a wind farm, but they are computationally costly (Sanderse et al. 2011).
- Engineering Wake Models (EWM) introduces simplified methodologies to describe the wake evolution and are less computationally expensive than CFD models (Vermeer et al. 2003).

Designing the optimal layout and thereby limiting the wake effects can enhance the predicted power production of offshore wind farms. The distance between each turbine in a wind farm is normally designed as a function of the rotor diameter to account for aerodynamic interactions from wake effects. Wind turbines are often installed in the far wake zone to reduce power loss due to wake effects. According to Hou et al. (2015), the turbine distance in the prevailing wind direction (between rows) should be 8–12D, whereas the crosswind direction (between lines) should be 3D to 5D. The crosswind turbine distance is wide enough that wake interactions do not emerge in each row and between rows. However, Ammara et al. (2002) observed that traditional design of 7-10D spacing between turbines resulted in overly sparse WT distributions, resulting in wind farms that underutilized the site's wind energy potential.

The research listed below have provided different WT layout optimization strategies based on various wake models. The ideal sites of WTs within wind farms were identified in these studies using objective functions that included greatest power generation and lowest LCOE.

- Mosetti et al. (1994) proposed a unique method for optimizing onshore large wind farms. The placement of wind turbines at a given location was optimized to extract the highest amount of energy for a reduced installation expense. A wake superposition-based wind farm simulation model is combined with a genetic search algorithm to achieve the optimization.
- Grady et al. (2005) revealed that genetic algorithms may effectively predict the best wind farm configuration.
- Marmidis et al. (2008) suggest that the Monte Carlo simulation method can provide a unique approach to the optimization tools that already exist. The results of the study were compared to those of genetic algorithms, which are obviously distinct from the Monte Carlo simulation technique. The study resulted in higher power outputs without necessarily requiring more turbines.
- Kusiak and Z. Song (2010) presented an approach for onshore wind farm layout optimization. Wind farm radius and turbine distance limitations were factored into the optimization model. The converted bi-criteria optimization issue is solved using a multi-objective evolutionary strategy approach that maximizes predicted energy output while minimizing constraint violations. The model increased energy output by strategically deploying wind turbines to minimize wake loss.
- Pookpunt and Ongsakul (2013) successfully employed the binary particle swarm optimization with time-varying acceleration coefficients (BPSO–TVAC) to discover the ideal location of wind turbines in a wind farm by extracting the highest power in a wind farm while minimizing investment costs. BPSO–TVAC was used to a wind farm test site with both uniform and non-uniform wind characteristics, using the linear wake model to predict downstream wind speed. When compared to genetic and evolutionary algorithms, results showed that BPSO–TVAC has the lowest investment cost per extracted power.

2.4.2 Wind Farm Patterns

According to Gao et al. (2014), the most common pattern in wind farms is the aligned WT arrangement. Existing large wind farms have used square configurations rather than parallelograms to balance energy production and reduce cabling costs. Simplified research by conducted Chamorro et al. (2011) concluded that staggered layouts were more efficient than aligned WT arrays for similar turbine separations in the downwind and crosswind directions. The results indicated that the staggered wind farm can generate 10 % more power output. WTs should not be deployed in grids, but spread around the farm, according to earlier optimization studies (2013, 2005, 1994). It has been claimed that a unique, asymmetric, site-specific wind farm pattern may best reflect the peculiarities of a certain wind resource area. However, several factors such as the seabed topography, wind speed, wind direction and turbine size all contribute to the decision of most suitable WT arrangement and spacing within a wind farm (Gao et al. 2014).

TOPFARM is a wind farm layout optimization software developed as part of an EU project lead by Risø National Laboratory with the aim of optimizing a project's total economic feasibility. Consequently, the balance between revenue from power generation and wind farm expenses including installation, operation, maintenance costs, and fatigue degradation are evaluated. The TOPFARM project is divided into eight work packages with each focusing on a different technical aspect among which, TOPFARM optimization platform's basic modules, sub-model verification, and optimization method for demonstration of onshore and offshore sites (G. C. Larsen and Réthoré 2013).

The TOPFARM optimization software has four basic modules:

- Wind farm flow field modelling.
- Aero-elastic modelling of wind turbines.
- Cost modelling.
- Optimization.

The first three modules are integrated in the last module to provide an optimal solution. This program contains a collection of various optimization techniques that are determined based on the problem's characteristics (G. C. Larsen and Réthoré 2013). In TOPFARM, a multi-fidelity technique with three degrees of fidelity is recommended for optimization. In this method, a rapid and approximate model can solve most of the challenge, while a comprehensive and accuracy orientated model is used to refine the search in particularly interesting regions.

2.4.3 Hydrodynamic Interactions

The hydrodynamic interactions due to wave scattering between the members of an array of stationary truncated circular cylinders representing the columns of an idealized TLP have been estimated using an approximate, computationally efficient technique (Williams and Demirbilek 1988). The solution approach is simply a large-spacing approximation that involves substituting similar plane waves for divergent dispersed waves, and non-planar correction components. The impact of various wave and structural characteristics on the hydrodynamic loading for a variety of cylinder designs has been demonstrated using numerical data. Even at relatively wide spacing's, considerable increases in hydrodynamic loading are projected for some parameter combinations compared to the loading that the cylinder would experience in isolation. According to these findings, designers and researchers developing TLPs should investigate the hydrodynamic interactions between surrounding columns.

Linton and Evans (1990) solved scattering of waves by an array of N bottom-mounted vertical circular cylinders based on Spring & Monkmeyer (1975), which devised a precise theory for the scattering of waves by N vertical circular cylinders. This was used to simplify the computation of forces and free-surface amplitudes. Improved formulations for the drift force on one of two cylinders in long waves are also proposed using the entire theory. When the number of cylinders, N, is big, the approach is demonstrated to be more efficient than the approximation method of McIver & Evans (1984). On the contrary, their methodology is applicable of a broader range of solution to problems, and the high quality of their estimate for the wave amplitude has been validated, as well as for closely spaced cylinders. The study (1990) provides examples of applications in the field of offshore structures. The current approach may also be used to solve acoustic radiation problems in two dimensions and to investigate the influence of incident waves on an endless row of identical evenly spaced vertical cylinders.

McIver (2002) states that wave interactions in an array can be broken down to a scattering problem and a sequence of radiation problems. For the scattering problem, each structure in the array is maintained in place and for the radiation problem in the absence of an incident wave, every structure is in turn forced to oscillate.

The linear scattering problem has dominated most wave interaction with arrays research. Nonlinear effects are difficult to examine in such complex geometries, however several notable nonlinear interaction effects were observed and identified in the study. Because scattered waves from several cylinders may arrive at the same place with the same phase in large regular arrays, interaction effects are amplified, resulting in substantial peaks in wave forces around specified wavelengths. In irregular arrays of structures, significant peaks caused by hydrodynamic interactions are seldom.

2.5 Energy Transmission and Storage

2.5.1 Energy Transmission

Electrifying offshore platforms has come a priority and the development of a renewable offshore energy hub could create unique opportunities for supplying ongoing marine operations and O&G installations.

As previously sated, Equinor along with their industry partners are developing world's first offshore wind farm providing renewable partially power the Snorre and Gullfaks O&G fields. This project was approved for an application for founding of up to 2.3 billion NOK by Enova and is expected to be operational within the third quarter of 2022 (Equinor 2019b). Hywind Tampen focuses on supplying renewable energy to O&G installations locally, with the aim of reducing CO_2/NO_x emissions by gradually replacing the energy produced from gas turbines. The FWT's will be connected in a loop by a 2.5 km-long, 66 kV dynamic inter-array cable system (Equinor 2019b). The wind farm is estimated to produce 35% (95 MW) of the power demand of the five O&G platforms.

The optimized design of electrical connection from the wind farm to the five petroleum installations utilized by the project is illustrated below.

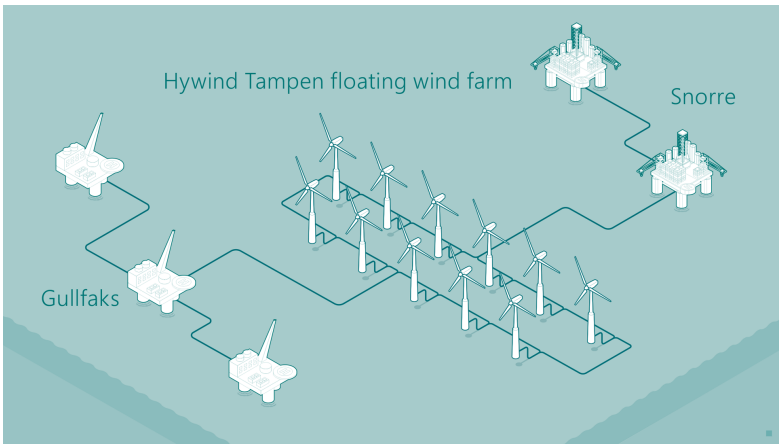

Figure 2.5: Wind farm layout illustrated by Equinor

This project is an actualisation of the much-researched topic: floating offshore wind in deep waters, let alone in the North Sea. However, Equinor's pursuit regarding this project is to further research for the technological advancement of sustainable energy production with less repercussions for future generations. The outcome of this project paves the way for a more sustainable hydrocarbon exploits, with an annual reduction of approximately 200,000 tonnes of CO_2 emissions (2019).

A parametric study of dynamic inter-array cable systems for floating offshore wind turbines was conducted and published in the Marine system & Ocean Technology journal (2020). The study aimed to contribute to the emerging development of offshore wind sector in connection with energy transmission and give an insight into the hydrostatic predesign of dynamic inter-array cable system by comparing two umbilical shapes, varying water depth and cable length via numerical analysis.

Figure 2.6 is a general depiction of an offshore wind farm producing power to shore. The dynamic inter-array cable system consists of inter-array cable of feeder, to terminal cable of feeder to offshore substation and continuing onto an export cable.

A collection substation is required to gather the generated power from each turbine of the wind farm. The collector substation is an offshore structure designed to receive electricity from wind turbines and increase the power voltage with a transformer. The necessity of such structure is based on the considerable distance from the offshore wind farm to shore and a converter substation provides efficiency to the transport process. The intent with a converter station is to transform electricity from High Voltage Alternating Current (HVAC) to High Voltage Direct Currents (HVDC), to increase efficiency for long distance power cables.

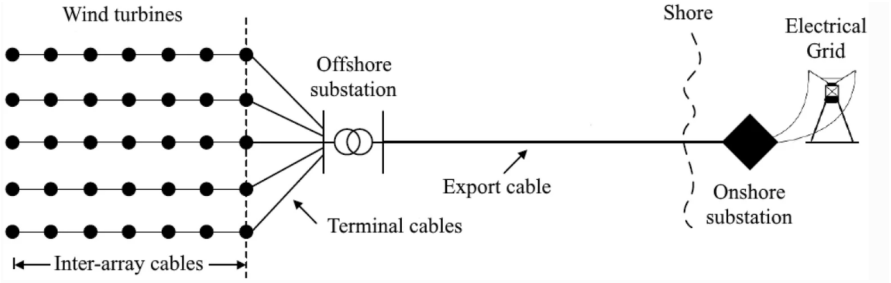

Figure 2.6: Energy transmission system of a floating offshore wind farm in top view.

The study concluded with hydrostatic analysis of the umbilical shapes; lazy wave shape is far superior to the catenary shape. Especially in water depth beyond 100 m, the catenary shape is not feasible due to the critical tension at the hang-off. Therefore, it would be economically sound to commission a sophisticated umbilical design to reduce the cable failure rate and prevent unintended costly maintenance.

2.5.2 Subsea Power Cables

The cabling system of offshore wind farms is a vital aspect to be considered. Power cables must be advanced and optimized as a consequence of technological advancements that are driving installations further from shore and into deeper seas. For an efficient and safe transport of electricity, cable designs must be optimized according to the location of the system, infrastructure, and technical properties. The electrical power system of an offshore wind farm can simply be subdivided into four phases: production, transportation, distribution and usage (2018). A wind turbine generates electricity using wind as a renewable energy source. Prior to entering the distribution network, electric power is transferred through a transmission network, then made available to various applications for use. Currently, the power generated from offshore wind turbines are consumed instantaneously and not stored. This is due to financial and technological constraints with storage alternatives for offshore wind energy.

Offshore wind farms are installed in a variety of configurations based on i.e., site conditions. However, offshore wind farms usually consists of several wind turbines in connection with a grid of subsea cables on the seabed. The wind turbines are connected by array cables, and if required, connected to an offshore substation which transforms the energy by increasing the voltage before being transported via export cables. According to Worzyk (2009) wind farms are commonly connected to onshore transmission grid by export cables. When the cable length exceeds 30 km, it is common to encounter the usage of HVAC (High Voltage Alternating Current) under 100 kV for export cables. However, for export cables HVDC is only an alternative if a converter station is in place (onshore and offshore). Thus, the power is converted from alternating current (AC) to direct current (DC) at the converter station. Due to the lack of mature technology and financial constraints most projects endure, the use of a converter station is only feasible when a significant amount of energy is produced. An inter-array cabling system of a wind farm is illustrated by DNV in Figure 2.7 (2022).

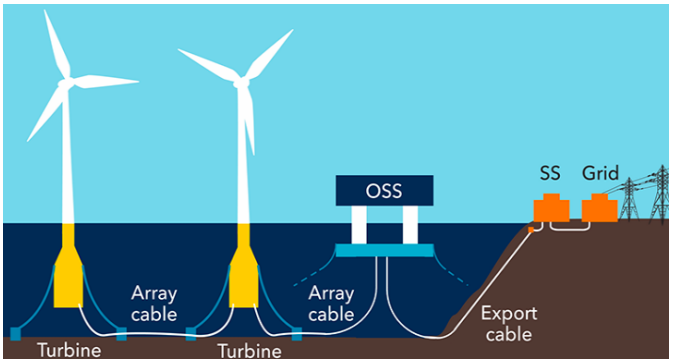

Figure 2.7: Offshore wind electrical system with array cables connected to an offshore substation

Cable Structure and Layers

The configuration of a subsea power cable is determined by what type of current is to be transported, alternating current (AC) or direct current (DC). AC cables typically consist of three conductors transporting the current in three phases, while DC cables incorporate a single conductor. The power generated by wind turbines is produced with alternating current, thus AC cables have been favoured within the offshore wind industry (2018).

The design of power cable is determined by the requirements of a project under development, whether it is a renewable or petroleum soured. The design requirements are dependent on; site condition, wind farm size, turbine size, necessity of converter, cable route, installation method and cable protection method. A cable is an assembly of mutable components consisting of individual/common screen/sheath, outer protection, assembly fillers and one or more power cores (conductor) (Resner and Paszkiewicz 2021). Optical fibers may be included in the cable depending on project requirements as it can be used for a variety of purposes, including temperature monitoring, data transfer, cable deformations (vibration/strain) measurement, and fault detection and location.

The majority of high voltage cables are individually designed per project specifications making repairs and maintenance challenging, nonetheless standardised requirements within the industry i.e. DNV standard (*Subsea power cables for wind power plants* 2016). A configuration of a common inter-array power cable is illustrated by Resner and Paszkiewicz (2021) in Figure 2.8.

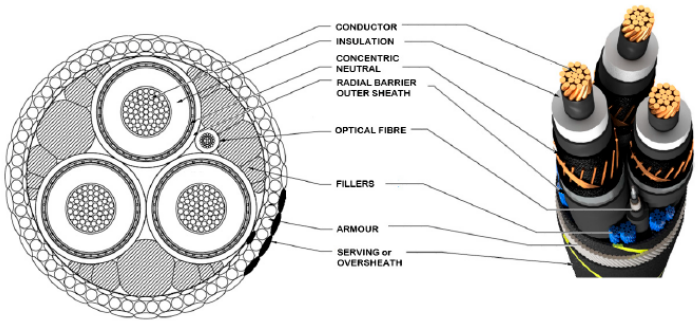

Figure 2.8: Configurations of a common inter-array cable

The following list describes some of the common components for a standard subsea power cable with a brief description of their functionalities to assure high reliability, strong abrasion and corrosion resistance, water resistance, and inherently reduce environmental impact.

- Conductor core: transfer of power (copper or aluminium).
- Insulation system: insulation on the conductor, equalizing stress in the electromagnetic field (oil-impregnated paper, cross-linked polyethylene, or ethylene propylene rubber).
- Sheath: water barrier, prevent fault currents.
- Armature: mechanical strength to prevent impact (Metallic, can consists of two layer of galvanised steel wire).
- Protection sheath: abrasion strength from outer layer of cable (polypropylene).

The development, construction, and optimization of a robust dynamic power cable for offshore floating wind turbines has to be prioritized. Worzyk (2009) states that the interaction of several loads including such wave, wind, and current are complex and therefore should be analyzed by a coupled model and experimental test for verification.

Cable Interface

Andersen et al. (2021) presented a concept description of the OO Star concept, where the goal is to design, build, install and test an the substructure supporting an 11 MW wind turbine. The report presents a preliminary design of the cable interface, but at the time of publication, no analysis of the dynamic HV cable had been completed. The cable interface consists of a HV cable hang-off flange together with a J-tube and bellmouth, as illustrated in Figure 2.9.

With a departure angle of 15 degrees towards vertical, the lower exit height was determined to be at bottom slab level. Between two corner columns, the azimuth angle is in the middle. Furthermore, the concept description explains that the minimum needed J-tube size is determined by the HV cable pull-in head, bend, weights, and support distances. The cable will be terminated at the top of the J-tube when the HV cable has been pulled in. On top of the J-tube, a cable weak link will be attached, which will remove the cable from its termination point if an accident happens. At the lower J-tube exit elevation, a bellmouth will be constructed to ensure an appropriate MBR (Minimum Bend Radius) for the HV cable. The bellmouth curvature will be appropriate for handling the angular displacements caused by the HV cable and will be determined by the final dynamic cable design.

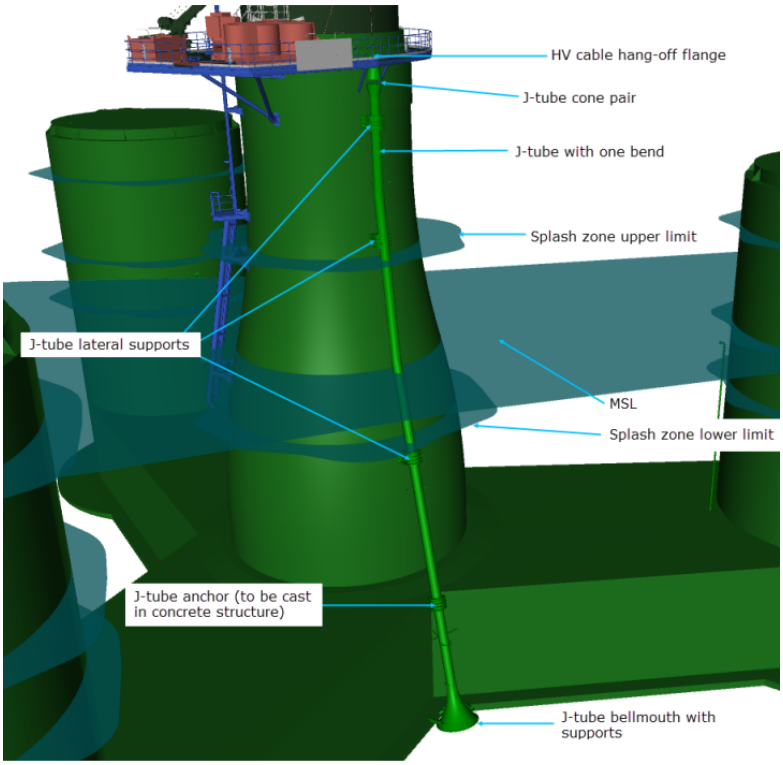

Figure 2.9: FLAGSSHIPS' cable interface proposal

2.5.3 Energy Storage

Energy storage has become a big topic in recent years in connection with the development of large-scale offshore wind turbines. The aim being storing stable energy and providing various approaches to managing power supply to create a long term and reliable energy infrastructure offshore.

The usage of energy storage integrates diverse energy resources and fluctuations caused by wind speed can be counterbalanced by storing excess energy. Simply put, energy storage allows electricity to be preserved for use when the demand is high. This method proved stability and reliability to the energy market by creating an efficient electrical grid. Simultaneously, such approaches can reduce greenhouse gas (GHG) emissions.

The most prominent proven technologies within energy storage are battery- and hydrogen storage. Batteries are a range of electrochemical storage solutions, which can include chemical batteries, flow batteries, and capacitors (Coppez et al. 2010). Hydrogen production uses excess power generated to convert into compressed hydrogen gas via electrolysis (Meier 2014). Figure 2.10 illustrated by SINTEF (2021) displaces an integrated energy system that consists of offshore wind power as the renewable source supplying industrial process or offshore O&G activities. The excess energy is stored in batteries and via electrolysis converted into compress hydrogen.

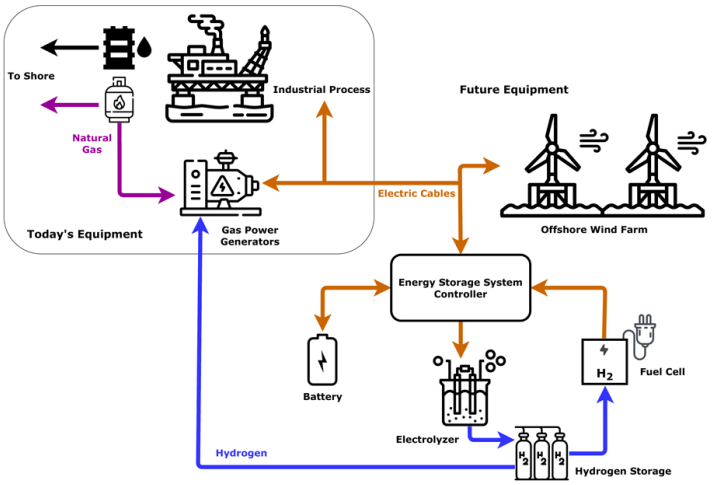

Figure 2.10: Integrated energy system from an offshore wind farm to an O&G platform.

Deep Purple is a research project conducted by TechnipFMC and their industry partners (2021). The pilot project aims to provide stable, renewable, and scalable energy based on proven technologies off-grid installations and remote islands, with hydrogen stored as a high-capacity battery and re-electrified (2021). The main objective being to store electricity produced from offshore wind turbines and convert it to hydrogen from seawater (electrolysis). The seawater is purified to fresh water for the electrolysis process through reverse osmosis. The hydrogen would be stored on the seabed for later use to provide renewable energy on-demand. Figure 2.11 displays an integrated energy system of offshore hydrogen production from wind energy.

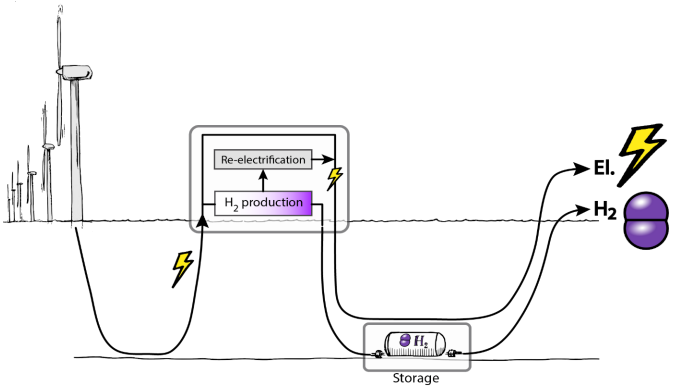

Figure 2.11: Simplified illustrations of the pilot project Deep Purple by TechnipFMC.

Hydrogen Production

The most recognized method of generation green hydrogen from renewable sourced energy is electrolysis. Thus, electrolysis has been an acknowledged part of the solution regarding climate research. The process of using electricity to split oxygen and hydrogen from water, which takes place in an electrolyzer. According to the office of energy efficiency and renewable energy (2022), the size of an electrolyzer can range from small to large applicable equipment based of the production facilities accommodations.

The figure below illustrates electrochemical reaction; electrolyzers like fuel cells consist of a cathode and an anode separated by an electrolyte and connected to electrical voltage. Due to the variety of electrolyte materials and ionic species, various electrolyzers function differently.

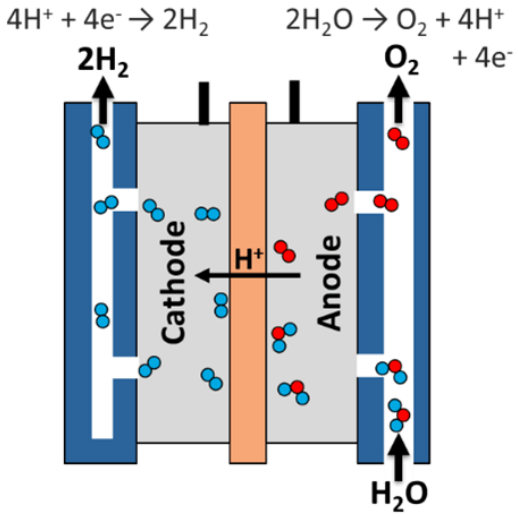

Figure 2.12: Electrochemical reaction, electrolysis.

Anode reaction:

$$2H_2O \longrightarrow O_2 + 4H^+ + 4e^- \tag{2.4}$$

Cathode reaction:

$$4H^+ + 4e^- \longrightarrow 2H_2 \tag{2.5}$$

For instance, a polymer electrolyte membrane electrolyzers consists of; a solid specialty plastic electrolyte in a polymer electrolyte membrane (PEM).

- The water reacts at anode to form oxygen and positively change hydrogen ions.
- The hydrogen ions flow through the PEM selectively to the cathode, while electrons flow through an external circuit.
- Hydrogen ions react with electrons from the external circuit to generate hydrogen gas at the cathode.

The water necessary for such reaction must be exceptionally pure. If electrolysis is to take place offshore, a reverse osmosis facility is necessary to purify the saltwater to fresh water (Meier 2014).

3 Theory

The following chapter provides the necessary theoretical and mathematical background for the numerical analysis of the feasibility study. A great deal of the theoretical background was taken from Sea Loads on ships and offshore structures, written by Prof. O.M Faltisen (1993).

3.1 Hydrodynamics

3.1.1 Linear Theory

First-order potential flow theory is used in HydroD to model the external flow around the semi-submersible FWT and is a simplified model of reality. The potential theory described by J. Newman (2018), is applied in HydroD, through WADAM to calculate first order radiation and diffraction effects on the FWT. There exists two kinematic requirements for potential flow:

- Incompressible and inviscid flow.
- Irrotational flow.

The first requirement means that the flow is assumed to be incompressible and inviscid:

$$\frac{\partial}{\partial t}V = 0 \tag{3.1}$$

The second requirement implies that the curl of the velocity field (i.e. vorticity vector) is zero everywhere in the fluid:

$$(\omega_x, \omega_y, \omega_z) = \vec{\omega} = \vec{\nabla} \times u = 0 \tag{3.2}$$

Due to the irrotational external flow, the velocity can be expressed as the gradient of a potential function, ϕ:

$$\nabla\vec{\phi} = \vec{u} \tag{3.3}$$

where,

$$\frac{\partial \phi}{\partial x} = u_x, \ \frac{\partial \phi}{\partial y} = u_y, \ \frac{\partial \phi}{\partial z} = u_z \tag{3.4}$$

Incompressible flow yields:

$$\vec{\nabla} \cdot \vec{u} = \frac{\partial u_x}{\partial x} + \frac{\partial u_y}{\partial y} + \frac{\partial u_z}{\partial z} = 0 \tag{3.5}$$

Hence, the potential is governed by a Laplace equation. The Laplace equation for the potential can be solved when given set of boundary conditions.

$$\left[\frac{\partial^2}{\partial x^2} + \frac{\partial^2}{\partial y^2} + \frac{\partial^2}{\partial z^2}\right] \phi = \nabla^2 \phi = 0 \tag{3.6}$$

Combining the assumptions with linear theory, the linear wave body interaction problem simplifies and the velocity potential, ϕ can be calculated. Figure 6.2 is an illustration of a marine vessel partially submerged in a liquid and illustrates the governing equations for the linear body wave body interaction problem in time-domain (Greco 2021).

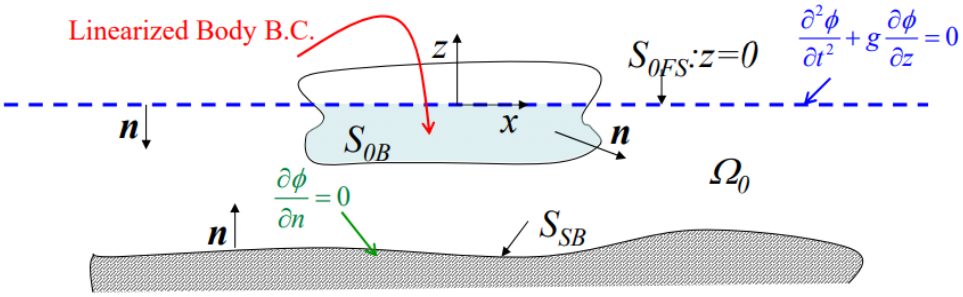

Figure 3.1: Illustration of a linear body wave body interaction problem

Ω_0 is the mean fluid volume, n is the normal vector pointing into the fluid, S_{0FS} is the mean free surface, S_{S0B} is the mean body wetted surface and S_SB is the seabed surface. The equations governing the problem in the Figure 6.2 are the following.

Sea bottom boundary condition, meaning no fluid can flow through the sea bed:

$$\frac{\partial \phi}{\partial n} = 0 \ \text{ on } S_{SB} \tag{3.7}$$

Laplace equation:

$$\nabla^2 \phi = 0 \ \text{ in } \Omega_0 \tag{3.8}$$

Body boundary condition:

$$\frac{\partial \phi}{\partial n} = V_B n \ \text{ on } S_{0B} \tag{3.9}$$

Combined free surface condition:

$$\frac{\partial^2 \phi}{\partial t^2} + g\frac{\partial \phi}{\partial z} = 0 \text{ on } z = 0 \tag{3.10}$$

In steady-state conditions, if the incident waves oscillate with circular frequency, ω, then the solution of the wave-body interaction problem oscillates with ω, and the combined free surface condition becomes:

$$-\omega^2 \phi + g\frac{\partial \phi}{\partial z} = 0 \text{ on } z = 0 \tag{3.11}$$

This becomes the basis of the frequency-domain analysis performed in HydroD.

Assuming that the floater is stationed in deep water, the velocity potential and wave elevation can be defined as:

$$\phi = \frac{g\zeta_a}{\omega} e^{kz} \cos(\omega t - kx) \tag{3.12}$$

$$\zeta = \zeta_a \sin(\omega t - kx) \tag{3.13}$$

where ζ_a is the wave amplitude, k the wave number and ω the angular wave frequency. The dispersion relation for deep sea waves in Equation 3.14 relates the wave number to the frequency.

$$\omega^2 = kg \tag{3.14}$$

3.1.2 Short Term Wave Statistics

To simulate an irregular sea, linear waves are utilized and this is accomplished by calculating statistical estimates of a sea state made up of multiple linear waves. Individual linear waves are superposed to produce the wave elevation of the long-crested irregular sea, as presented in Equation 3.15

$$\zeta = \sum_{j=1}^{N} \zeta_j \sin(\omega_j t - k_j x + \epsilon_j) \tag{3.15}$$

where ζ_j is the wave amplitude, ω_j the circular frequency, k_j the wave number and ϵ_j a random phase angle of wave component j.

3.1.3 Wave Spectrum

A wave spectrum, which depicts wave energy in the frequency domain, is frequently used to characterize the state of the sea. The wave amplitude can be represented by the by spectrum ($S(\omega)$) and the difference frequency ($\delta\omega$), as presented in Equation 3.16.

$$\frac{1}{2}\zeta_j^2 = S(\omega_i)\delta\omega \tag{3.16}$$

Wave spectra can be estimated through wave measurements and in general, every location has a different wave spectrum since the sea state varies. Standarized spectras, such as the Pierson-Moskowitz (PM) and JONSWAP (Joint North Sea Wave Project) are created to accurately represent sea states.

3.1.4 Response in Regular Waves

The response of a large volume subjected to hydrodynamic waves can be linearly superposed as the sum of the response due to individual wave components, in first-order wave theory. The hydrodynamic problem can be divided into two sub-problems in regular waves, per Faltisen's definition (1993):

1. "The forces and moments on the body when the structure is restrained from oscillating and there are incident regular waves. The hydrodynamic loads are called **waves excitation loads** and composed of so-called Froude-Kriloff and diffraction forces and moments."
2. "The forces and moments on the body when the structure is forced to oscillate with the wave excitation frequency in any rigid-body motion mode. There are no incident waves. The hydrodynamic loads are identical as **added mass**, **damping** and **restoring** terms."

The diffraction problem is defined in 1), by integrating the incident wave and diffraction dynamic pressure with the mean wetted hull surface, the two force components can be obtained. The radiation problem is defined in 2), added mass (A) and damping (B) terms are in connection with the dynamic pressure, while restoring (C) terms are in connection with the hydrostatic pressure.

The hydrodynamic problem can be formulated as Equation 3.17 when the hydrodynamic properties have been obtained. Through the requirement of an equilibrium between the two isolated problems in 1), 2) and considering the excitation forces and moments in direction j as the real component of the complex load function $F_{jk}^{-i\omega t}$.

$$F_j e^{-i\omega t} = \sum_{k=1}^{6}[(M_{jk} + A_{jk})\ddot{\eta}_k + B_{jk}\dot{\eta}_k + C_{jk}\eta_k] \tag{3.17}$$

The 6-DOF equation of motion for a rigid body in water is given by the equation above, where $\ddot{\eta}_k$, $\dot{\eta}_k$, η_k are the body motion, velocity, and acceleration. Numerical simulations in HydroD (WADAM) and SIMA can be utilized to calculate the response of the FWT concept presented in this thesis.

3.1.5 Non-Linear Effects

Second-order effects are of interest for moored semi-submersibles, due to the high natural periods in surge, sway and yaw deriving from the mooring system (Faltinsen 1993). The instantaneous position of the floating body is explained by second-order potential theory. When solving a second-order problem, the solution become more precise than a linear problem, nonetheless it is not an exact solution. The solution includes a linear solution, mean forces and forces oscillating with difference- and sum-frequencies. The terms involved in the problem are proportional to ζ_a or ζ_a^2, where ζ_a is the wave amplitude.

For floating wind turbines with slacked mooring lines, difference-frequency forces and moments are important as a result of the high natural periods. The term depending on the difference-frequency is essential for a moored semi-submersible because it may reach near the structure's natural periods in surge, sway, and yaw and excite large oscillations.

Mean Drift Loads

According to Faltinsen (1993), mean wave drift forces in a potential flow model are due to "floating body's ability to create waves". For surface-piercing structures subjected to regular waves, the relative vertical motion between the floating body and the waves creates a non-zero mean pressure, which results in a mean wave force.

Due to the pressure obtained from the second-order velocity potential has zero mean, it does not contribute to the mean drift forces. Therefore, the mean drift loads can be calculated using only the first-order velocity potential. The mean wave forces can be calculated in WADAM using the following two different techinques:

- Conservation of momentum (three horizontal DoFs).
- Direct pressure integration (six DoFs).

The following is the equation for the mean drift load derived from conservation of momentum:

$$\overline{F_i} = -\overline{\int\int_{S_\infty} [pn_i + \rho V_i V_n] ds} \qquad i = 1, 2, 6 \tag{3.18}$$

Where $\overline{F_i}$ is the resulting mean force on the body, V_i the fluid velocity, V_n the normal component of the fluid velocity at the body surface, S_∞ the time-dependent wetted surface, ρ the water density and p the pressure normal to S_∞.

When utilizing direct pressure integration to calculate mean drift forces, the complete Bernoulli's equation is used and integrated over the exact wetted surface. The mean drift load can be written as:

$$\overline{F_i} = \frac{\rho g \zeta_a^2}{2} \int_{L_1} \sin^2(\theta + \beta) \eta_i dl \tag{3.19}$$

Where ζ_a is the wave amplitude, L_1 the the non-shadow part of the water plane curve, θ the angle of the hull and β the wave propagation direction.

Slow Drift Motions

Slow-drift motions are defined by Faltinsen (1993) as "resonance oscillations excited by non-linear interaction effects between the waves and the body motions". For moored-structures, difference-frequency forces and moments excite slow-drift motions in surge, sway and yaw. For slow-drift excitation loads, a contribution from the second-order velocity potential is required. F_i^{SV} is the slow-drift force or moment presented in Equation 3.20.

$$F_i^{SV} = \sum_{j=2}^{N} \sum_{k=2}^{N} \zeta_j \zeta_k \left[T_{jk}^{ic} \cos\{(\omega_k - \omega_j)t + (\epsilon_k - \epsilon_j)\} + T_{jk}^{is} \sin\{(\omega_k - \omega_j)t + (\epsilon_k - \epsilon_j)\} \right] \tag{3.20}$$

Where ζ_j and ζ_k are the wave amplitudes, ω_j and ω_k are the wave frequency and ϵ_k and ϵ_j are random phase angles for the waves. T_{jk}^{ic} and T_{jk}^{is} are the second-order transfer functions (quadratic transfer functions), dependent on the wave frequencies.

The diagonal components of the second-order transfer function correspond to the mean drift force, and F_i^{SV} can be calculated in all 6 DoFs.

Newman's Approximation

The full quadratic transfer functions for a large frequency domain are computationally costly to calculate. Newman's approximation is a simplified technique used for calculating the second-order slow-drift motions. Faltinsen (1993) states that the Newman's approximation is based on the assumption that T_{jk}^{ic} and T_{jk}^{is} can be approximated by T_{jj}^{ic}, T_{kk}^{ic} and T_{jj}^{is}. This is possible because T_{jk}^{ic} and T_{jk}^{is} do not change substantially with frequency. The second-order transfer functions can be approximated to their values on the line $\omega_j = \omega_k$ due to the difference-frequencies that are near to the resonance oscillation frequencies are usually small. This implies that the QTFs are calculated using simply the mean drift forces. The second-order transfer functions T_{jk}^{ic} and T_{jk}^{is} are defined as:

$$T_{jk}^{ic} = T_{kj}^{ic} = 0.5 \cdot (T_{jj}^{ic} + T_{kk}^{ic}) \tag{3.21}$$

$$T_{jk}^{is} = T_{kj}^{is} = 0 \tag{3.22}$$

These equations can be inserted into Equation 3.20. Furthermore, the square of a series can replace the double summation to simplify the equation. Thus, the slow-drift force with Newman's approximation can be written as:

$$F_i^{SV} = 2 \cdot \left(\sum_{j=1}^{N} \zeta_j (T_{jj}^{ic})^{\frac{1}{2}} \cos(\omega_j t + \epsilon_j) \right)^2 \tag{3.23}$$

Wave Drift Damping

The slow-drift motion in surge, sway, and yaw causes wave drift damping, which is defined as "the first-order correction in terms of slow-drift velocity of the mean wave drift force" (Finne et al. 2000). It functions as a damping force in the equation of motion and is proportionate to body speed. The wave drift damping can be expressed in a 3x3 matrix (B) due to the connection between the slow-drift movements in the horizontal plane. The coefficients of the matrix can be obtained from the momentum conservation equations.

Viscous Effects

When viscous forces are of importance, the Morison's equation 3.24 can be used to calculate the wave loads on circular cylindrical structural members of fixed offshore structure, such as semi-submersibles (Faltinsen 1993). The equation is a semi-empirical formula and is used for the in-line force, meaning normal to the cylinder axis and along the wave direction (Clauss et al. 2002). The different parts of the semi-submersible body are assumed slim and elongated, such that and strip theory can be utilized. In order to calculate the 3D force, integration along the body of the elementary force, dF, from the strip dz must be performed (Faltinsen 1993). This is given by the sum of the two following contributions:

$$dF = dF_{mass} + dF_{drag} = \frac{\rho\pi}{4} D^2 C_M a_1 + \frac{1}{2} \rho D C_D u|u|)dz \tag{3.24}$$

where the different terms of the Morison's equation is:

- ρ = mass density of the water.
- D = cylinder diameter.
- C_M = mass coefficient.
- a_1 = acceleration of the midpoint of the strip.
- C_D = drag coefficient.
- u = horizontal undisturbed fluid velocity.

The damping force which acts on the structure is not a part of the potential flow theory. From the Morison's equation, the drag force, dF_{drag} for a fixed cylinder with a diameter of D is calculated as:

$$dF_{drag} = \frac{1}{2}\rho D C_D |u - \dot{\eta}|(u - \dot{\eta}) \tag{3.25}$$

3.2 Aerodynamics

While wind resources have been utilised for energy production since the late 1800s, offshore wind is a rather recent phenomenon. Since the development of the first offshore wind farm in 1991, Vindeby, the industry has grown dynamically the last 10 years. Offshore wind has gained significant momentum in the past decade. This is due to wind resources at sea are generally superior to those on shore. Moreover, the location results in a lower visual impact and less noise creation than with turbines on land (Ladenburg and Dubgaard 2009).

The aerodynamic loads acting on a wind turbine originates from wind and are divided into short- and long-term variations. For aerodynamic loads on a wind turbine, the short-term wind condition is of particular interest. Associate Professor at the Department of Wind Energy at DTU, Martin Otto Laver Hansen published the book: "*Aerodynamics of Wind Turbines*"(2015), which provided most of the aerodynamics theory.

When analysing the aerodynamics of a wind turbine, the turbine rotor, nacelle and tower are subjected to different loads. The loads acting on the nacelle and tower can be assumed to be drag force, while the rotor experience both lift and drag force. The aerodynamic forces can be calculated using several different methods and accuracy levels. However the blade element momentum theory (BEM) is widely used for numerical tools. SIMA utilizes BEM to calculate the aerodynamic forces on wind turbine blades. BEM theory can be used to calculate steady loads, thrust and power on the turbine blades for a variety of wind speeds and pitch angles. The thrust T and torque Q from BEM theory are defined in the equations below:

$$dT = 4a(1-a)\frac{1}{2}\rho v_0^2 s\pi r dr \tag{3.26}$$

$$dQ = 4a'(1-a)\frac{1}{2}\rho v_0 \omega r^2 2\pi r dr \tag{3.27}$$

Where a and a' are induction factors, defined as velocity reduction on the disc relative to incoming velocity, v_0 and ω is the angular rotor velocity. The forces normal to the rotor plane (p_N and p_T) can be found based on lift force, L, drag force, D and angle ϕ, seen in Figure 3.2 (M. Hansen 2015).

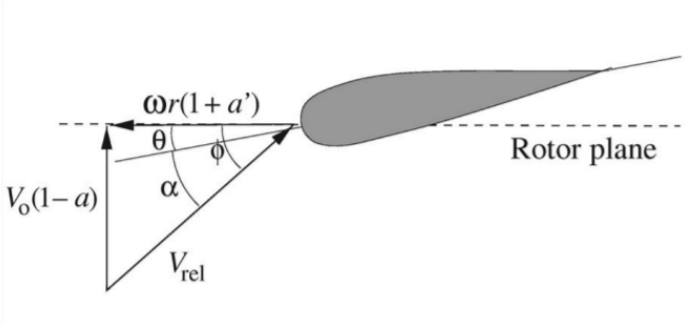

Figure 3.2: Forces normal to the rotor plane

Equation 3.26 and 3.27 can be rewritten into:

$$dT = Bp_N dr = B(L\cos\phi + D\sin\phi)dr \tag{3.28}$$

and

$$dQ = Brp_T dr = Br(L\sin\phi - D\cos\phi)dr \tag{3.29}$$

Where B is the number of blades.

3.2.1 Corrections of BEM

In order to obtain reliable results, several corrections to the BEM theory must be applied in SIMA. This section explains these corrections.

Prandtl's Tip Loss Factor

The fact that the original BEM theory ignores the effect of tip loss is one of its key inaccuracies. Another essential assumption in BEM theory is that turbines run with an unlimited number of blades. This is corrected by Prandtl's tip loss factor (Bachynski-Polić 2021).

Glauert Correction for High Values of *a*

For an axial induction factor (a) greater than 0.5, BEM theory is not applicable. The rotor reaches the so-called "turbulent wake state" when turbines operate at high tip speed ratios, meaning constant speed turbine at low wind velocities. The flow behind the rotor slows down in this situation, while the thrust on the rotor disk continues to increase. The Gluert correction factor is used in SIMA for these instances (M. Hansen 2015).

Dynamic Wake

Dynamic wakes will be present for the rotor blades in realistic scenarios. This effect is caused by a time lag in induced velocities due to shedding and downstream vorticity convection. A method of filtering the induced velocity has been developed in SIMA to account for this impact (Bachynski-Polić 2021).

Dynamic Stall

For a particular angle of attack, the drag and lift coefficients (C_D and C_L) supplied to BEM theory may be characterized as static lift and drag curves. However, in the actual world, while altering the angle of attack, the flow can suddenly connect and detach, causing the coefficients to deviate from the static curves. Transient loads may be considerable as a result of the dynamic stall effect, since the blade may still have a high lift coefficient after a rapid rise in wind speed (Bachynski-Polić 2021). The Stig Øye model is used in SIMA as a way to simulating dynamic stall effects (M. Hansen 2015).

Other Corrections of BEM in SIMA

SIMA also includes the tower shadow effect. When the blades rotates by the tower, the incoming flow is affected, leading to thrust variations that can cause fatigue damage. In addition, skewed inflow corrections provide for the possibility of rotor tilt or yaw angle between the rotor and entering wind. Lastly, hub losses adjust for the existence of the turbine's hub (Ormberg and E. E. Bachynski 2012).

3.3 Coupled time-domain analysis

3.3.1 Time-Domain Solution

The results of the frequency domain computations performed using HydroD are loaded into SIMA to perform time-domain simulations. The convolution integral is used to solve the frequency dependent equation of motion in SIMA (SINTEF 2017). The equation of motion can be represented in matrix form (Equation 3.30).

$$[\boldsymbol{M} + \boldsymbol{A}(\omega)]\,\ddot{\boldsymbol{\eta}} + \boldsymbol{B}(\omega)\dot{\boldsymbol{\eta}} + \boldsymbol{C}\boldsymbol{\eta} = \boldsymbol{f}(t) \tag{3.30}$$

$$\boldsymbol{A}(\omega)\ddot{\boldsymbol{\eta}} + \boldsymbol{B}(\omega)\dot{\boldsymbol{\eta}} = \boldsymbol{f}(t) - \boldsymbol{M}\ddot{\boldsymbol{\eta}} - \boldsymbol{C}\boldsymbol{\eta} \tag{3.31}$$

where:

$$\boldsymbol{A}(\omega) = \boldsymbol{A}_\infty + \boldsymbol{a}(\omega) \tag{3.32}$$

$$\boldsymbol{B}(\omega) = \boldsymbol{B}_\infty + \boldsymbol{b}(\omega) \tag{3.33}$$

Since $\boldsymbol{A}_\infty = \boldsymbol{A}(\omega = \infty)$ and $\boldsymbol{B}_\infty = \boldsymbol{B}(\omega = \infty) = 0$, Equation 3.31 can be rewritten into:

$$-\omega^2 \boldsymbol{A}_\infty \boldsymbol{\eta}(\omega) + [i\omega \boldsymbol{a}(\omega) + \boldsymbol{b}(\omega)]\, i\omega \boldsymbol{\eta}(\omega) = \boldsymbol{F}(\omega) \tag{3.34}$$

Furthermore, an inverse Fourier transform is applied to convert the equation from frequency-domain to time-domain:

$$\boldsymbol{A}_\infty \ddot{\eta} + \int_\infty^t \boldsymbol{h}(t - \tau)\boldsymbol{\eta} d\tau = \boldsymbol{f}(t) \tag{3.35}$$

The full time-domain equation is then:

$$[\boldsymbol{M} + \boldsymbol{A_\infty}]\, \ddot{\boldsymbol{\eta}} + \boldsymbol{C\eta} + \int_0^t \boldsymbol{h}(t - \tau)\dot{\boldsymbol{\eta}}(\tau) d\tau = \boldsymbol{q(t, \eta, \dot{\eta})} \tag{3.36}$$

where a transform of the frequency dependent added mass and damping yields the retardation function, $\boldsymbol{h}(\tau)$. The vector $\boldsymbol{q}$ consists of:

- $\boldsymbol{q^{(1)}}$: first order wave excitation loads calculated in HydroD.
- $\boldsymbol{q^{(2)}}$: second order wave loads obtained from QTF functions with free surface model in HydroD.
- $\boldsymbol{q_{drag}}$: nonlinear quadratic drag force obtained with the drag term of the Morison's equation and strip theory.
- $\boldsymbol{q_{wind}}$: obtained with SIMO/RIFLEX.
- $\boldsymbol{q_{current}}$: obtained with SIMO/RIFLEX.
- $\boldsymbol{q_{mooring}}$: obtained with SIMO/RIFLEX.

3.3.2 Non-Linear FEM

As previously stated, FWT response is solved in time domain for each time step. SIMA is used to define external loads, whereas RIFLEX is used to compute structural aerodynamic and hydrodynamic loads of slender, flexible elements (Ormberg and E. E. Bachynski 2012). The non-linear finite element method, which can account for large deformations and displacements, is used for the latter. Additionally, it can be used to compute accurate responses for cases with changing boundary conditions, these characteristics are significant useful in FWT analysis. This is due to non-linearities in turbine rotor blades induced by significant deformations, and the quadratic behavior of thrust and drag forces (Kvittem 2014).

The global system is discretized according to the location of each node and element in the non-linear FEM. According to the governing equation 3.37, the mass, damping, and stiffness properties of each element are combined into global matrices. The turbine tower is considered to be a rigid structure for this thesis, and the global mass, damping, and stiffness matrices contain data on the floating body (which can be computed) in HydroD, rotor blades, rotor hub, and mooring components. The contributions of external forces are compiled in the global matrix R_{ext}.

$$M_g\ddot{D} + B_g\dot{D} + R_{int} = R_{ext} \tag{3.37}$$

Where R_{ext} is the exertion induced by external load equal to the exertion induced by inertial, dissipative and internal forces, respectively $M_g\ddot{D}$,$B_g\dot{D}$ and R_{int}. D is the nodal displacements.

3.4 Mooring Line Loads

Catenary Theory

A mooring system consisting of three catenary anchor wires secures the floating wind turbine to the seabed. Because of the weight of the chains, these anchor lines provide stiffness to the platform, and it is critical to design a mooring system that is stiff enough to minimize excessive offsets. Due to the anchors inability to take on vertical stresses, the part of the mooring lines closest to the anchors lies horizontally on the seabed. Hence, the system is accessible to move. The catenary equations described below are taken from Faltinsen's Sea Loads (1993).

Figure 3.4 shows how a catenary shaped mooring line is shaped below the structure (Faltinsen 1993). A floating structure is generally moored with 3 or 4 cables anchored to the sea bed. From Figure 3.3, motions of a moored floating structure is illustrated. The influence of waves, wind and current can be seen and how the structure moves from an original position to a new (mean) position. The structure is moored and the mooring system provides stiffness to the structure. The mooring system provides tension, which forces the structure to an initial position and acts as non-linear springs.

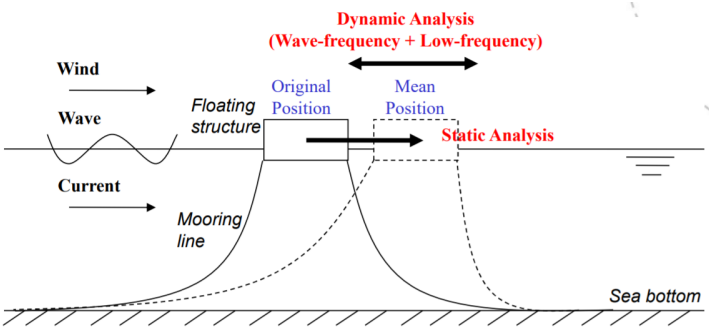

Figure 3.3: Motions of a moored structure

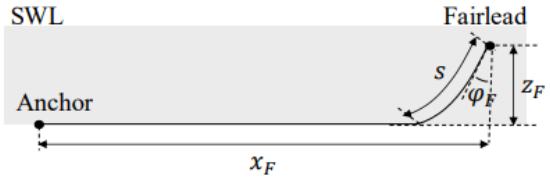

Figure 3.4: Side view of mooring line

Figure 3.5 illustrates the static loads on a mooring element:

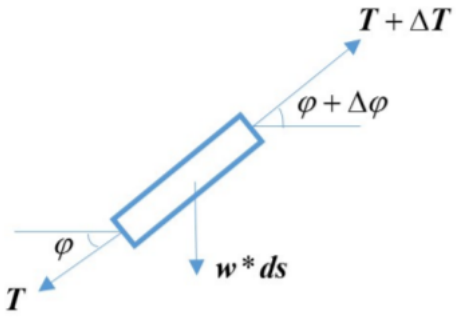

Figure 3.5: Static loads on a mooring element

where $T + dT$ and T are tensions at the top and bottom ends of the element and $w \cdot ds$ is the effective weight. With regards to the figure above, it was assumed only gravity and buoyancy forces acting on the mooring lines. It was also assumed that the mooring lines remain in an xy plane.

Furthermore, when the platform gains motion, the line characteristics are represented by the force-displacement curve ($\Delta F_x - \Delta X$). This can be seen from Figure 3.6:

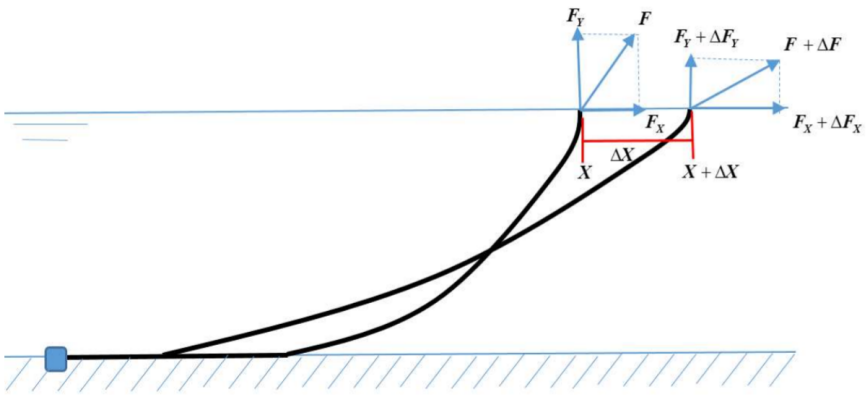

Figure 3.6: Line characteristics of the mooring line

When the platform experiences motion and displaces from the equilibrium position, a force in the horizontal direction develops. This force generates a restoring effect on the platform motions, given by the stiffness, K:

$$K = \frac{\Delta F_x}{\Delta X} \tag{3.38}$$

From the catenary inelastic equation, where elasticity is neglected, the length of the suspended line, l_s, and the vertically span, h, can be defined as:

$$l_s = \left(\frac{T_H}{\omega}\right) \sinh\left(\frac{\omega x}{T_H}\right) \tag{3.39}$$

and

$$h = \frac{T_H}{\omega}\left[\cosh\left(\frac{\omega x}{T_H}\right) - 1\right] \tag{3.40}$$

where T_H is the horizontal tension at the fairlead, ω the mooring line weight (N/m) and x the horizontal length of the suspended line. The suspended line length can be defined when combining the equations above:

$$l_s^2 = h^2 + 2h\frac{T_H}{\omega} \tag{3.41}$$

The horizontal distance between the fairlead and the anchor is defined as the variable, X. This is defined as:

$$X = l - l_s + x \tag{3.42}$$

where l is the total length of the line.

Furthermore, X, can written as a function of T_H, such that the mean position of the floating structure can be found for various loading conditions. Equation 3.43 combines Equation 3.41 and Equation 3.42 so that the anchor position can be found for a pre-determined pre-tension T_H:

$$X = l - h\sqrt{1 + \frac{2T_H}{\omega}} + \frac{T_H}{\omega} arccosh\left(1 + \frac{h\omega}{T_H}\right) \tag{3.43}$$

4 FWT Concept

The FWT system was modelled in SIMA and based on the data from the Dr. Techn. Olav Olsen and described in the LIFES50+ (2018) and Flagship projects (2021).

4.1 OO Star Wind Floater

The floating structure tested numerically in this project is the semi-submersible substructure, OO-Star wind floater, which acts as a foundation for floating wind turbines. The structure is designed to have a 10 MW wind turbine installed in the center cylinder. Figure 4.1 is a structural drawing of the OO Star 10 MW Wind Floater Semi (Yu et al. 2018).

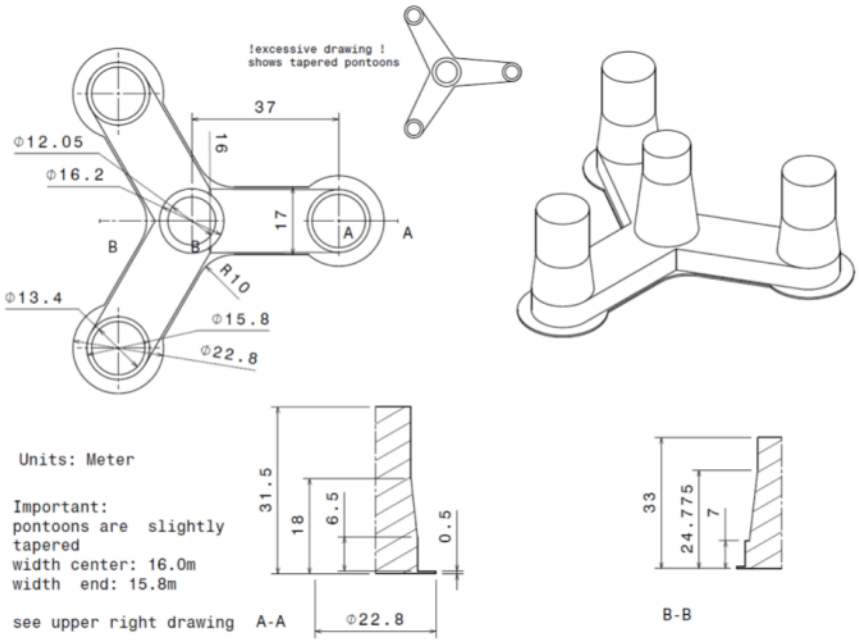

Figure 4.1: Structural drawing of the OO Star 10 MW Wind Floater Semi

Table 4.1 provides information about the structural properties of the full-scale OO Star 10 MW Wind Floater Semi (Yu et al. 2018).

Table 4.1: Main properties of the OO-Star floating platform

Property	**Unit**	**Value**
Total substructure mass	[kg]	2.1709e+07
Tower base	[m]	11
Draft	[m]	22
Freeboard	[m]	11
Center of buoyancy	[m]	-14.236
Angle between pontoons	[°]	120
Material	[-]	Post-tensioned concrete

Table 4.2 provides information about the modelling properties used for input in the analyses.

Table 4.2: Properties used in the analyses

Property	**Unit**	**Value**
Water depth	[m]	130
Sea water density	$[kg/m^3]$	1025
Gravitational acceleration	$[m/s^2]$	9.8070

4.1.1 Wind Turbine Dimension

The wind turbine selected for the analysis in this project was the DTU 10 MW reference turbine. The turbine is developed by the department of Wind Energy at Technical University of Denmark and is a 10 MW horizontal axis wind turbine. It has three blades, variable-speed and is collective pitch controlled. The drivetrain is medium speed and has a multiple stage gearbox. The turbine blades have a prebend to ensure tower clearance (Bak et al. 2013).

Table 4.3: Key properties of the 10MW turbine

Parameter	**Unit**	**DTU 10 MW**
Power rating	[MW]	10
Specific power	$[W/m^2]$	401
Rotor orientation	[-]	Upwind
Number of blades	[-]	3
Cut-in wind speed	[m/s]	4
Rated wind speed	[m/s]	11.4
Cut-out wind speed	[m/s]	25
Rotor diameter	[m]	178.3
Hub diameter	[m]	5.6
Hub height	[m]	119
Rotor precone	[°]	-2.5
Shaft tilt	[°]	5
Blade prebend	[m]	3.3
Cut-in rotor speed	[RPM]	6
Rated rotor speed	[RPM]	9.6
Blade mass	[tons]	3×41

4.1.2 Mooring System

The mooring system was based on the design presented by Yu et al. (2018) in the LIFES50+ project and constructed in SIMA. The mooring system's configuration is displayed in Figure 4.2. It consists of three chains with a horizontal angle of 120° between each. All three lines have a clump mass linked to them, which divides the line into two parts. The upper part is 160 meters long and connects to the fairlead. The bottom part measures 543 meters in length. The horizontal lenght from anchor point to fairlead is 689 m. Table 4.4 summarizes the paramount mooring system parameters. For the sections above and below the clump mass, the chain characteristics are identical.

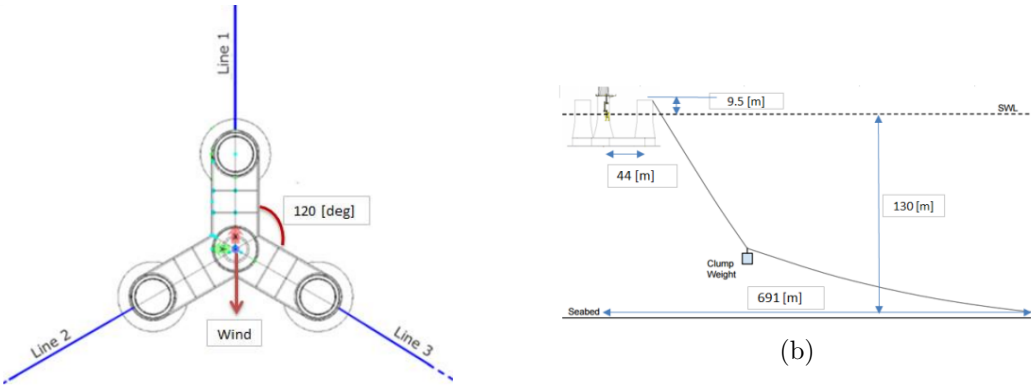

(a) (b)

Figure 4.2: Mooring line configuration, top and side view

Table 4.4: Mooring system properties for the OO-Star Wind Floater Semi 10MW based on the LIFES50+ report

Property	**Unit**	**Value**
Number of lines	[-]	3
Angle between adjacent mooring lines	[°]	120
Total mass clump weight	[kg]	51025
Location of fairleads above MSL	[m]	9.5
Pre-tension	[N]	1.67E+06
Extensional stiffness EA	[N]	1.506E+09
Physical chain diameter	[m]	0.137
Hydrodynamic added mass coefficient	[-]	0.8
Hydrodynamic drag coefficient	[-]	2.0
Equivalent mass per length in air	[kg/m]	375.38
Equivalent weight per length in water	[N/m]	3200.6
Type	[-]	Studless Grade R3

5 Environmental Conditions of Site Location

5.1 Site

Due to an unexpected cancellation of partnership with a Norwegian energy company, the site of the wind farm has been altered to a hypothetical case for legal purposes. However, the installation site remains in the central part of the Norwegian North Sea, approximately 190 km west of Stavanger. (The location is a part of the geological formation, Utsira High). The power demand of the O&G installations is approximately 35 MW and expected to increase over the coming years due to subsea tie-in projects.

The environmental conditions at the site were studied to ensure durability and survivability of the floating wind turbines. The met-ocean data for the site were provided Prof. Kjell Larsen at NTNU. The water depth at this region ranges from 115 - 150 m, and the average wind speed is 8.78 m/s. Thus, a wind turbine installed at 130 m water depth with a rated wind speed of 11.4 m/s is deemed suitable. The maps in Figure 5.1 illustrate the site location (Directorate 2022) & (De Hauwere 2016).

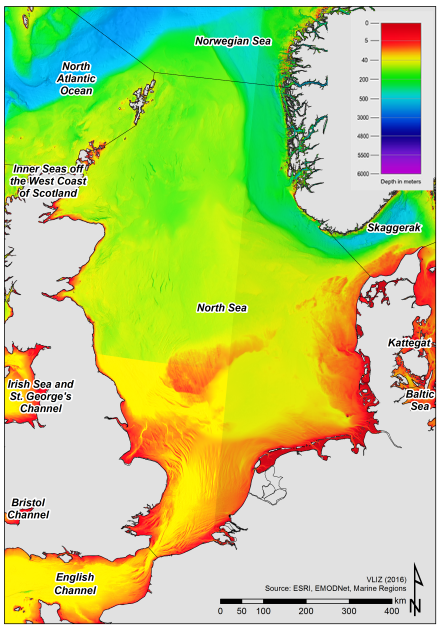

(a) Bathymetry of the North Sea

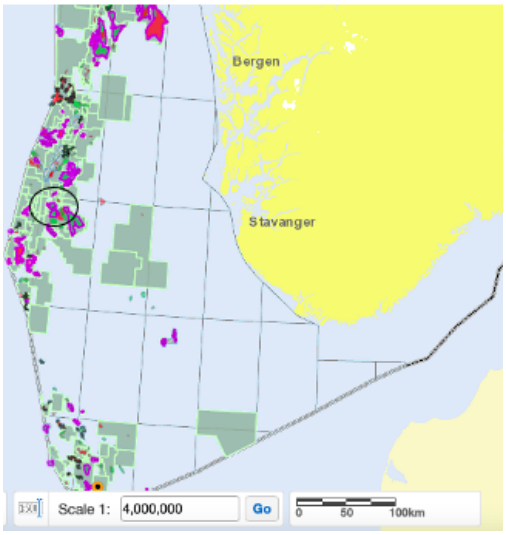

(b) Map of the North Sea from the Norwegian petroleum directorate.

Figure 5.1: The selected site of the wind farm.

5.2 Wind Loads

From the article *Joint distribution of environmental condition at five European offshore sites for design of combined wind and wave energy devices* (2015) it was determined that the power law wind velocity profile can be used at the location in the North Sea:

$$U_W(z) = U_{10}\left(\frac{z}{10}\right)^{\alpha} \tag{5.1}$$

where α is the wind shear exponent and can be set to 0.1 for this exact location, U_{10} is the mean wind velocity at 10 m above sea level and z is the vertical coordinate (z=0 is the still water level).

In the SIMA workspace, the power law profile was selected and the input parameters were:

- Horizontal velocity.
- Wind direction.
- Reference height.
- Wind shear exponent, α.

From Equinor's *Snorre Field Metocean Design Basis* (2016), the annual mean wind velocity at 10 m above sea level was found. The Snorre Field is an oil and gas field located in the northern part of the North Sea and is assumed to have similar metocean properties as the site location selected in this thesis. The environmental load conditions correspond to three different sets of wind velocities:

- Annual mean wind velocity.
- Wind velocity at cut-out.
- Extreme wind velocity with a 100 year return period.

The annual mean wind velocity represents the wind velocity that the wind turbine is most likely to encounter 10 m above sea level and by following the Snorre Metocean Design (2016). it was determined to be 8.78 m/s at z = 10 m. The velocity at cut-out is 25 m/s and is the highest wind velocity the turbine will experience in operational conditions. In the extreme condition the wind turbine is parked, because the wind velocity ascends the cut-out value. Table 5.1 shows the wind velocities at hub-height and at z = 10 m, calculated with Equation 5.1:

Table 5.1: Wind velocities at 10 m and hub-height used in time-domain simulations

Operational condition	U_{10} [m/s]	U_{119} [m/s]
Mean annual	8.78	11.25
Cut-out	19.51	25
Extreme	35	27.32

Wind Distribution Model

In order to capture realistic wind conditions, factors such as wind gusts and turbulence was introduced. The stochastic, full-field, turbulent-wind simulator, TurbSim, was used to incorporate this into the wind simulations. This program generates numerical turbulent wind flow simulations that can be loaded into programs like SIMA.

The standard: *IEC 61400 - Part 3: Design Requirements for Offshore Wind Turbines*, presents various wind models that can be utilized in this thesis and it was decided to apply the Normal Turbulence Model (NTM) for the operational wind velocities (J. Jonkman 2007). For the vertical distribution of the average wind velocity, the wind model uses the power law distribution. The power law coefficient, α, turbulence intensity, I, and standard deviation σ_1 are deducted from IEC 2019. Equation 5.2 presents the standard deviation of the NTM, with $\alpha = 0.1$.

$$\sigma_1 = I_{ref}(0.75\, U_{hub} \ + \ 5.6) \tag{5.2}$$

The extreme turbulence model (ETM) was employed under extreme conditions. This was similarly built with TurbSim and the standard deviation of the ETM is:

$$\sigma_1 = 2I_{ref}\left(0.072\left(\frac{U_{avg}}{2} \ + \ 3\right) \cdot \left(\frac{U_{hub}}{2} \ - \ 4\right) \ + \ 10\right) \tag{5.3}$$

5.3 Wave Loads

5.3.1 Short Term Statistics

Wave Spectrum

The time-domain analysis in SIMA, where the operational conditions were simulated required significant wave height, peak period and direction values. From Equinor's *Snorre Field Metocean Design Basis* (2016), the wave spectres in the short-term sea state analysis are advised to be:

- Torsethaugen frequency spectrum, which is a modified JONSWAP spectra representing swell and wind seas contributions, respectively.
- The JONSWAP spectrum can be used to describe pure wind seas.

The JONSWAP wind-generated wave spectrum was decided to be used in the time-domain analysis for this location in the North Sea based on research from Li et al. (2015). It is assumed that the waves are mostly generated from wind in the selected location.

5.3.2 Long Term Statistics

Based on research from Johannessen et al. (2001) and Li et al. (2015), the two-parameter Weibull distribution was decided to be used as the conditional distribution of significant wave height, H_s for given wind speeds, U_w.

It is necessary to use a joint distribution of the wind velocity (U_w), wave height (H_s) and peak period (T_p) to calculate the wave height and wind period for known wind velocities. The joint distribution was described by Li et al. 2015. The conditional probability density function of H_s is given as a two-parameter Weibull distribution:

$$f_{H_s|U_w}(h|u) = \frac{\alpha_{HC}}{\beta_{HC}} \left(\frac{h}{\beta_{HC}}\right)^{\alpha_{HC}-1} \cdot exp\left[-\left(\frac{h}{\beta_{HC}}\right)^{\alpha_{HC}-1}\right] \tag{5.4}$$

where α_{HC} and β_{HC} are shape and scale parameters which can be determined from:

$$\alpha_{HC} = a_1 \ + \ a_2 \cdot u^{a_3} \tag{5.5}$$

$$\beta_{HC} = b_1 \ + \ b_2 \cdot u^{b_3} \tag{5.6}$$

where a_1, a_2, a_3, b_1, b_2 and b_3 are the parameters estimated from the raw data from the environmental conditions in the Central North Sea.

Table 5.2: Parameters used when calculating the expected value of H_s for a given U_w

Parameter	a_1	a_2	a_3	b_1	b_2	b_3
Value	1.755	0.184	1.0	0.534	0.07	1.435

For a given U_w, the expected value of H_s is:

$$E[H_S|U_w] = \beta_{HC}\Gamma\left(1 \ + \ \frac{1}{\alpha_{HC}}\right) \tag{5.7}$$

Furthermore, Li et al. (2015) describes that the conditional distribution of T_p given H_s and U_w, is based on the lognormal conditional distribution, presented in Equation 5.8.

$$f_{T_p|U_w,H_s}(t|u,h) = \frac{1}{\sqrt{2\pi}\sigma_{ln(T_p)}t} \cdot \exp\left(-\frac{1}{2}\left(\frac{ln(t) - \mu_{ln(T_p)}}{\sigma_{ln(T_p)}}\right)\right) \tag{5.8}$$

and Johannessen et al. (2001) suggested that the mean value of T_p can be modeled using the Equation 5.9.

$$\mu_{T_p}\bar{t}(u,h) = \bar{t}(h) \cdot \left[1 + \theta\left(\frac{u - \bar{u}(h)}{\bar{u}(h)}\right)^{\gamma}\right] \tag{5.9}$$

$t(\bar{h})$ and $u(\bar{h})$ are the expected spectral peak period and mean wind speed for a given value of H_s, presented in Equation 5.10 and 5.11. γ and θ are fitting coefficients.

$$t(\bar{h}) = e_1 + e_2 \cdot h^{e_3} \tag{5.10}$$

$$u(\bar{h}) = f_1 + f_2 \cdot h^{f_3} \tag{5.11}$$

where e_1, e_2, e_3, f_1, f_2 and f_3 are parameters from nonlinear curve fitting taken from Li et al. (2015) and the Central North Sea area. The fitting coefficients, γ and θ, and the nonlinear curve fitting parameters are presented in Table 5.3.

Table 5.3: Values used in the calculation of T_p taken from Li et al. (2015)

Parameter	θ	γ	e_1	e_2	e_3	f_1	f_2	f_3
Value	-0.477	1.0	5.563	0.798	1.0	3.5	3.592	0.735

5.4 Current Loads

The floating wind turbine is subjected to current loads, composed of wind-generated and tidal current. DNV's *Recommended Practice on Environmental Conditions and Environmental Loads* (2010), introduces the total current profile and is expressed as the sum of the wind current and the tidal current components.

$$U_c = U_c^{wind} + U_c^{tidal} \tag{5.12}$$

Furthermore, the wind current and tidal current profiles can be defined as:

$$U_c^{wind} = U_c^{wind}(0)\left(\frac{d_0 + z}{d_0}\right) \tag{5.13}$$

$$U_c^{tidal} = U_c^{tidal}(0)\left(\frac{d + z}{d}\right)^{1.7} \tag{5.14}$$

where

- U_c^{wind} and U_c^{tidal}: current velocities at the mean surface line.
- d_0: reference depth for wind-generated current.
- d: total water depth at the respective location.

Information about the current data was obtained from Equinor's met-ocean data design of the Snorre field (2016). The mean annual current at a water depth of 5 m were selected because the Metocean data provide a joint distribution for wind and current. At a water depth of 5 m, the mean annual current speed is 0.2 m/s. The extreme current value was taken as the current velocity with a 100 year return period. From (2016), this value was 1.38 m/s.

5.5 Load Cases

Six different load cases were established based on the environmental conditions. The first load case (1.OP) is based on met-ocean data from Equinor (2016) and are operational conditions. The second load case (2.OP) included the same H_s and T_p as 1.OP,but the wind was neglected. The third load case (1.NC) includes wind velocity at the cut-out speed. The directions for wind, wave and current were all set to 0°, as presented in Figure 4.2. The expected H_s and T_p for 1.OP and 1.NC were calculated in python using the equations described in Section 5.3.2. 1.EX used extreme values with a return period of 100 years for U_w, H_s and T_p based on the met-ocean data from Equinor (2016).

Table 5.4: Environmental load cases for the simulations

	Wind			Waves			Current	
Load Case	Model	$U_{W,119}$ [m/s]	Dir. [°]	H_s [m]	T_+ [s]	Dir. [°]	$U_{c,z=-5}$ [cm/s]	Dir. [°]
1.OP	NTM	11.25	0	1.90	7.25	0	0.20	0
2.OP	-	0	-	1.90	7.25	0	0.20	0
1.NC	NTM	25	0	5.08	8.38	0	0.20	0
2.NC	-	0	-	5.08	8.38	0	0.20	0
1.EX	ETM	35	0	15.5	16.9	0	1.38	0
2.EX	-	0	-	15.5	16.9	0	1.38	0

6 Methodology

6.1 Coordinate System

The global (earth-fixed) coordinate system is defined in Figure 6.1 and the local (body-fixed) coordinate system is defined in Figure 6.2 (Yu et al. 2018). The mean water level coincides with the xy-plane, with the z-axis being positive upwards. An incidence direction of 0° for waves, wind and current corresponds to the positive x-direction.

The body-fixed coordinate system is fixed to the body and translates/rotates along with the body. The calculations of load and motion response refer to the body-fixed coordinate system.

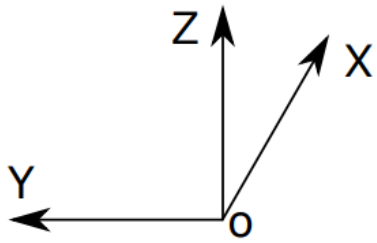

Figure 6.1: Global (Earth-fixed) coordinate system

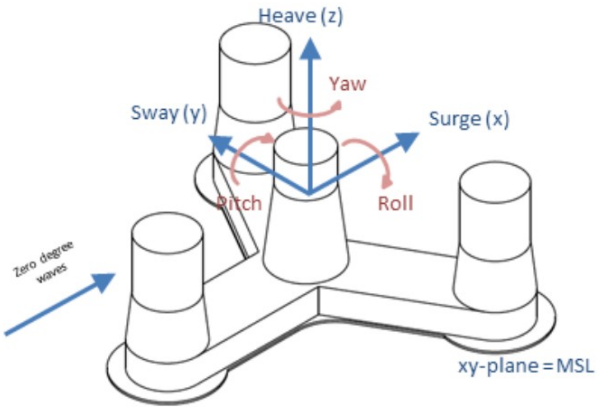

Figure 6.2: Local (body-fixed) coordinate system

6.2 Computational Programs

The flow diagram for the numerical analysis of the floating wind turbine is given in Figure 6.3. State-of-the-art software was used in order to set up a numerical model of the FWT.

- GeniE was used for modelling the geometry of the FWT and generating FEM panel model.
- HydroD was used for hydrodynamic analysis with the WADAM application. The panel models from GeniE was imported into HydroD.
- SIMA was utilized for coupled time-domain aero-hydro-servo-elastic analysis by using a SIMO/RIFLEX-coupling.

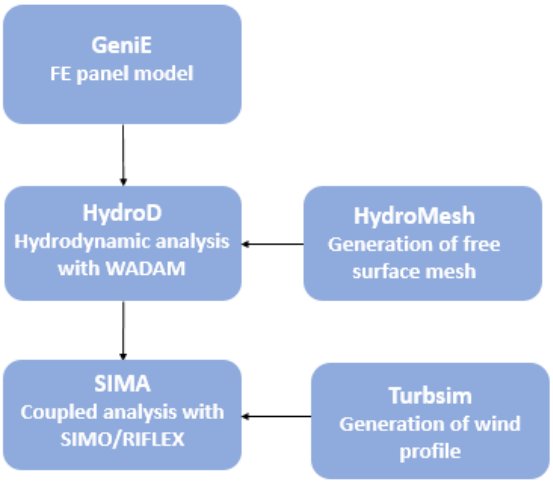

Figure 6.3: Flow diagram of the computational programs used in the numerical modelling.

6.2.1 GeniE

GeniE is a DNV software and part of the Sesam package. GeniE is a structural design analysis tool and can be used for modelling for various structures, i.e. floating semi-submersible platforms or bottom-fixed structures. The program combines beam, plate and shell modelling, which yields analyses of finite element mesh and load calculation.

In this project a discretized panel model of the floating substructure were made and imported into HydroD.

6.2.2 HydroD

In order to compute hydrostatics, stability, wave loads and motion response of the offshore structure, HydroD can be utilized. The program is an interactive application used for hydrostatic and hydrodynamics analyses and can be operated in frequency and time domain. HydroD is fully integrated with finite element analysis and consists of two sub-features; WADAM and WASIM. WADAM can be used to calculate general hydrodynamic problems for floating and fixed structures. It is used to calculate wave loads with first and second-order 3D potential flow theory and Morison's equation in the frequency domain. WASIM is an application which also implements Morison's equation, however it provides the possibility to solve 3D diffraction problems by a Rankine panel method. WASIM can be utilized for analyses in frequency- and time-domain.

The WADAM application was used in this project in order to perform a frequency domain analysis of the floating semi-submersible. The WADAM code run a panel method dependent on potential flow theory to acquire frequency dependent added mass and radiation damping. It is also possible to get the frequency dependent force and motion transfer function, in addition to restoring, mass and retardation functions from WADAM.

6.2.3 SIMA

SIMA is an integrated simulation workbench designed for analyses of marine operations and floating systems. SIMA workbench includes the numerical codes SIMO and RIFLEX, which is used for coupled analyses of floating platforms. SIMO is an abbreviation of Simulation of Marine Operations and is used as a time-domain program to model offshore structures. The application used for modelling of static and dynamic analysis of slender marine bodies, is called RIFLEX. This is a nonlinear finite element model code and can model systems such as mooring lines, wind turbine blades and towers. SIMO and RIFLEX are coupled together to model FWTs in various environmental conditions. Blade Element Momentum theory (BEM) is used to calculate the aerodynamic forces in SIMA. This includes corrections for wakes and dynamic stall (Atcheson et al. 2016).

For this project, SIMA was utilized for numerical simulations of the dynamic behavior of the FWT in time-domain. Environmental modelling was conducted and the following aspects were considered:

- Current and wind profiles.
- Wave and wind input.
- Seafloor properties, including stiffness and friction.
- Specific data for the site location i.e., water depth, gravity, water density and seabed topography.
- Irregular time conditions i.e., wind data, wind generated wave data and current.

When analyzing and simulating the FWT in SIMA, the turbine, blades and control system can be specified in the program or be given via link to an external program. The mooring system can be defined in SIMA and the hydrodynamics of the floating foundation can be read from general hydrodynamic analysis programs. A time domain analysis by a fully coupled method can analyse the whole floating system, with mooring lines.

The hydrodynamic coefficients will be read from HydroD. Additionally, wind and current coefficients, vessel damping coefficients and viscous force elements to calculate the Morison forces are relevant parameters for the simulation.

6.2.4 TurbSim

TurbSim is a stochastic, full-field, turbulent-wind simulator, used to generate numerical turbulent wind flow simulations that can be loaded into SIMA. In order to capture realistic wind conditions, factors such as wind gusts and turbulence was introduced. The software was developed by B. J. Jonkman (2009) and the wind input files in the program are generated as a box containing 2D-grids of the incoming wind's instantaneous velocity.

6.3 Panel Models

6.3.1 Floating Structure Model

The panel models of the OO Star 10MW Wind Floater Semi was created in GeniE. The model was based on the dimensions presented in Figure 4.1, from the LIFES50+ report 2018. The model included no structural properties and was constructed by shell elements and discretized into panels. The panel model was only half of the necessary body, however WADAM let the user apply symmetry about the xz-axis. Linear frequency domain analysis considered the submerged part of the body, however the panel model included the whole body in order to be able to conduct a second-order frequency-domain analysis. Figure 6.4 illustrates the FEM model made in GeniE and imported into HydroD:

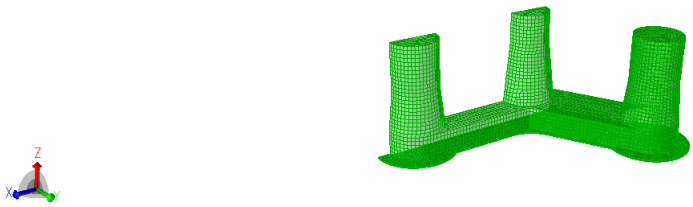

Figure 6.4: Panel model of the OO-Star floater made in Genie

High quality numerical models must always strike a compromise between efficiency and precision. Models with very large panel elements do not provide a very accurate portrayal of the body's geometry or fluid pressure fluctuations across the element, while models with very small panel elements increase computation time and cost. The aim was to create the most efficient model that can deliver the required level of precision. For the purpose of finding the most efficient model, four different panel models were investigated in the first-order frequency domain analysis. Each panel model had a different element size on the surfaces of the body. The main method of comparison was the resulting added mass coefficients and heave RAOs.

Figure 6.5 is a comparison between the surge added mass of the four different panel models, with varying element length. The figure is a zoomed in plot of the surge added mass from the first-order frequency domain analysis. The four different models do not show any significant difference in the values for A_{11}.

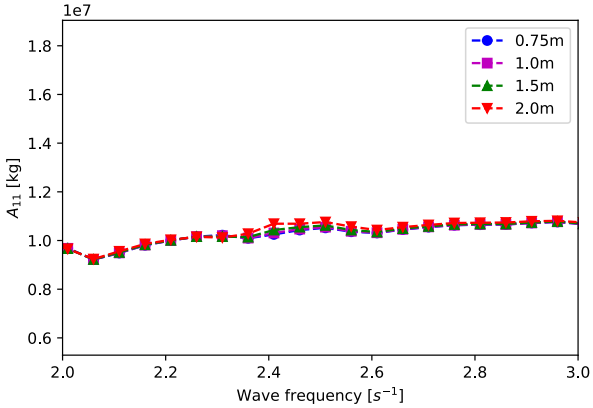

Figure 6.5: Surge added mass comparison of different element sizes.

Figure 6.6 presents the RAOs of the four different panel models, with varying element sizes. The plot is zoomed in on the peak at $\omega = 0.3\ s^{-1}$, where difference can be seen in the coarse and fine models. The difference between the model with element size of 0.75 m and 2.0 m is 22 %.

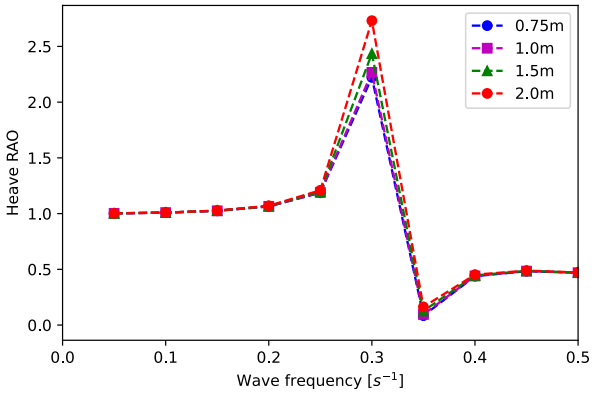

Figure 6.6: Heave RAO comparison of different element sizes obtained from HydroD.

Table 6.1 shows the run time of the four different panel models during the first-order frequency domain analysis from 0 to 4 s^{-1}.

Table 6.1: First-order panel model comparison of computation duration.

Element size [m]	**Number of elements**	**Run time [s]**
0.75	10249	2242
1.0	6148	730
1.5	3018	172
2.0	1874	72

From the table above, the computation time increases exponentially with the number of elements. This suggests that an increase in number of elements does not necessarily equate to superior results, especially if the panel models with a coarser mesh presents a tiny margin of error. The element size of 1.0 m was selected to be further investigated and the results from the first-order frequency domain analysis are presented in Section 6.4.

6.3.2 Free Surface Model

A finite element model of the free surface mesh was defined in order to run the second order analysis in HydroD. This can either be done in GenieE or in HydroD via HydroMesh.

The free surface model was designed with a hydro pressure load case in a negative z-direction. Furthermore, the free surface model was designed as a half-circle with the same symmetry as the floating structure. The model was designed with cut-outs for the surface-piercing components.

- Maximum panels: 10 000.
- No triangular elements allowed.
- According to the WADAM user manual (2019, the radii R_1 and R_2 of the outer boundaries of the free surface should be determined according to the decaying rate of local waves. In addition, the free surface radius is advised to be at least 50 % of the water depth.

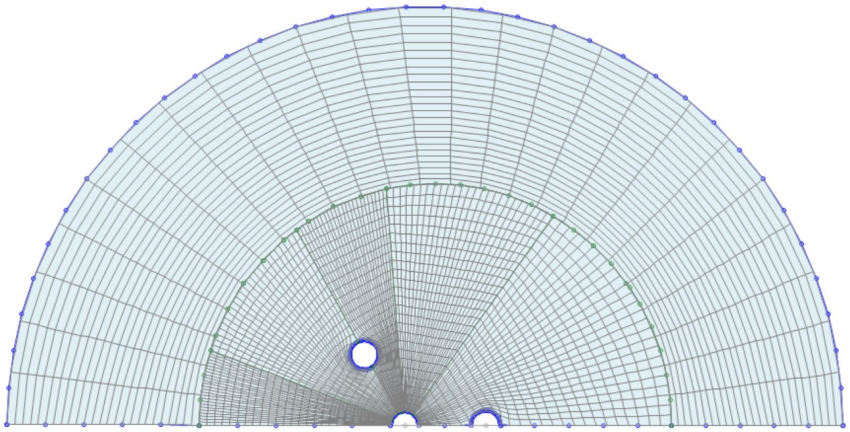

Figure 6.7: Free surface mesh in HydroMesh

The free surface mesh included 3750 number of panels. Figure 6.8 illustrates the free surface mesh and the panel model of the OO Star semi-submersible in the HydroD interface.

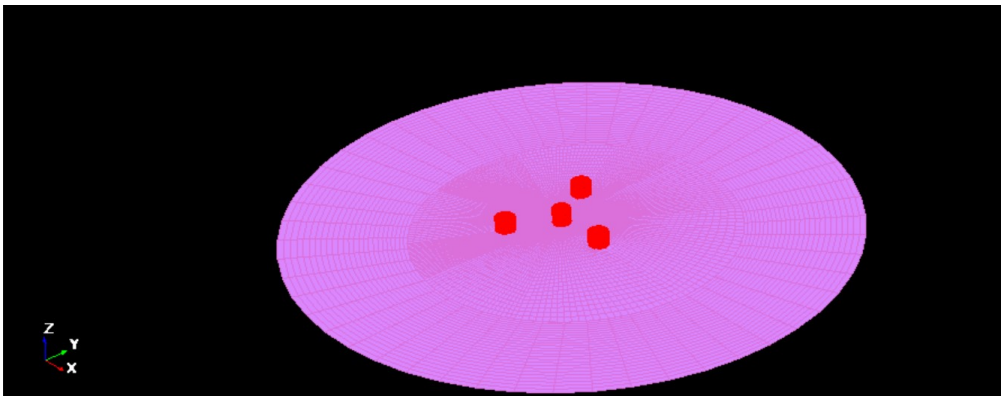

Figure 6.8: Capture of the free surface mesh and the panel model in HydroD

6.4 Frequency Domain Analysis

The frequency-domain analyses of the floating offshore wind turbine was based on potential flow theory. The goal of the analyses were to obtain the hydrodynamic characteristics of the structure and to verify the numerical model. The WADAM application in HydroD was used for the frequency-domain analysis, and it used a panel method to obtain the hydrodynamic properties. The output of the frequency domain analyses was the following properties of the OO-Star floater:

- Frequency dependent added mass and radiation damping.
- Mass matrix and hydrostatic stiffness.

- Total excitation forces and moments.
- First-order response amplitude operator (RAO).
- Horizontal mean drift forces and moments in surge, sway and yaw.
- Wave drift damping in surge, sway and yaw.
- Quadratic transfer function (QTF) for difference-frequency forces and moment in surge, heave and pitch.

The frequency-domain analyses examined the submerged part of the hull of the floating structure. As a part of the post-processing, a python script was constructed to visualize the results from the first- and second-order frequency domain analyses.

6.4.1 First-Order Frequency Domain Analysis

The first-order frequency domain analysis consisted of 25 number of waves from 0 - 360 degrees with wave frequencies ranging from 0.01 s^{-1} to 4 s^{-1}. The results from the analysis computed with WADAM in HydroD was given in large structured query report file, where the output consisted of the following properties:

- Matrix of the added mass coefficient.
- Matrix of the damping coefficients.
- Matrix of the excitation forces and moments from the Haskind relation (Diffraction problem).
- First-order response amplitude operator (RAO) for surge, heave and pitch.

The output of the first-order analysis in HydroD consisted of matrices of the added mass coefficients, damping coefficients, excitation forces and moments and the response amplitude operators (RAO).

As a part of verifying the numerical model, the frequency dependent added mass, damping and excitation forces of the numerical models, with varying element size, were compared with the public LIFES50+ results (2018).

6.4.2 Second-Order Frequency Domain Analysis

In addition to the linear frequency domain analysis described above, a second-order hydrodynamic analysis was performed in HydroD. This analysis made it possible to obtain the difference-frequency excitation forces and moment in surge, heave and pitch. As a part of the second-order hydrodynamic study, the mean wave drift forces and wave drift damping were also calculated. Pressure integration and conservation of fluid momentum were used to calculate mean drift forces, whereas conservation of fluid momentum was used to calculate wave drift damping. The QTFs can be obtained by two different methods in the second-order frequency analysis.

The transfer function can be calculated using Newman's approximation, where the second-order velocity potential is not employed, and mean drift forces are used instead. The other method is performed by pressure integration of the body, which takes into account contributions from all difference frequencies. The second-order velocity potential is required for this approach, as well as a panel model of the free surface. Since the difference-frequency effect occurs when two frequencies differ, all possible combinations of the frequency input were included for investigation.

Once the free surface mesh was created and included, WADAM can be modified to include results for the difference frequencies. The frequency range was set between 0.5 s^{-1} and 1.5 s^{-1}, with a $\delta\omega$ of 0.03 s. This range was smaller than the first-order analysis, however this is justified since computational time increases with the square of the number of frequencies.

The approximation's validity is predicated on the assumption that the frequency difference is modest due to the included error of order $O(\delta\omega^2)$ (Duarte et al. 2014). As a result, when calculating difference-frequency forces for large offshore systems in deep waters with natural periods above 100 s, Newman's approximation is usually valid. Lower natural periods can result in undesirable design outcomes due to the errors involved.

6.5 Coupled Dynamic Analysis

6.5.1 Coupled Model

In the SIMA-workbench, the models for hydro-aero-servo-elastic analysis was completed. The hydrodynamic data from the frequency domain analysis was imported to SIMA, as a SIMO body. Hence, the output from WADAM was imported as a nodal component. The floating substructure was attached to the wind turbine and the mooring lines through the master-slave technique. The mooring fairleads and the top of the turbine tower were characterized as slaved nodes, while the floating structure defined as their master.

Three different models were created in the SIMA-workbench to investigate what impact the different hydrodynamical load models had on the results. A RIFLEX model of the DTU 10 MW wind turbine and its respective control system was imported to the workbench for each model. In addition, a RIFLEX model of the mooring system was attached with the platform. The three models investigated in the thesis were:

- First-order frequency domain analysis model (**1.M**).
- Second-order frequency domain analysis with wave drift damping calculated with wave loads calculated with Newman's approximation (**2.M**).
- Second-order frequency domain analysis with full QTF (**3.M**).

The first model (1.M) included the results from the first-order frequency domain analysis and neglects second-order effects. The second model (2.M) considered the first- and second-order frequency domain effects, but includes the wave-drift force. The wave loads in this model were obtained by the Newman's approximation. The third model (3.M) considered the first- and second-order frequency domain effects and the difference-frequency wave force transfer function was included in the SIMO body.

6.5.2 Viscous Effects

The Morison equation was used to predict viscous effects on the OO-Star Semi floating substructure during. The drag coefficient, C_D, of the cylindrical bodies of the semi, was based on the LIFES50+ report (2018). The drag coefficient from the Morison equation (C_D) and quadratic drag (Q_D) are presented in Table 6.2. The approach for calculating the quadratic drag terms are presented in Equation 6.1. To compensate for viscous damping, the coupled model in SIMA were separated into slender components and the viscous drag coefficients were included.

Because the floating substructure was deemed brand new, no marine growth impacts were addressed. However they are important factors to be be included during design of a full scale model (Pegalajar-Jurado et al. 2018).

$$Q_D = \frac{1}{2}\,\rho\, C_D\, D \tag{6.1}$$

Table 6.2: Viscous coefficients on the SIMA model of the OO-Star Semi floating substructure

Slender element of semi	D [m]	C_D [-]	Q_D $[Ns^2/m^3]$
Upper central column	12.05	0.729	4502
Center central column	14.13	0.717	5192
Upper outer column	13.4	0.720	4945
Center outer column	14.6	0.713	5335
Rectangular pontoon	7	2.05	7354
Cylindrical pontoon	15.8	0.706	5717
Heave plates	15.8	10.0	80975

6.5.3 Mooring System Design

The mooring system was based on the design from the LIFES50+ project. A node was added to the fairlead and anchor positions in SIMA to define the mooring system. The mooring system is defined in Chapter 4.1.2 and is made up of chains with a horizontal angle of 120° between them. Each line has a clump mass with equivalent weight in water of 51025 kg linked to it, which divides the line into two parts. The upper part is 160 meters long and connects to the fairlead.

The minimum breaking strength of the mooring lines were calculated based on DNV (2015)'s Equation 6.2:

$$MBS_{R3} = 0.0223d^2 \cdot (44 - 0.08d) \tag{6.2}$$

where d is the chain diameter in mm.

6.5.4 Control System and Wind Input

A file supplying input for the wind turbine control system was imported into SIMA. This control system input file was provided by Prof. Erin Bachynski-Polić and is the updated control system developed in the LIFES50+ project (2018). Wind turbines are most efficient at the rated wind speeds. Below the rated wind speed, the purpose of the controller is to maximize power capture, while above the rated wind speed, the purpose is to regulate generator speed. This is achieved through two sub-systems:

- Generator-torque controller.
- Variable speed-collective blade-pitch controller.

They are independent systems and the generator-torque controller works below rated wind speed and the blade-pitch controller works above rated wind speed (M. H. Hansen and Henriksen 2013).

Furthermore, the turbulent-wind simulator TurbSim was employed when creating turbulent wind input files to the time-domain simulations. The wind files are based on the environmental load cases presented in Section 5.5. B. J. Jonkman (2009) explains that the wind input files in the program are generated as a box containing 2D-grids of the incoming wind's instantaneous velocity. The hub and rotor are considered to be horizontally centred on the grid, and each grid includes the entire rotor area. Because the rotor radius is 89.15 meters, the grid size is defined as a 200 m x 200 m box. Every grid has a 3D velocity vector and a matrix of 32 grid points vertically and horizontally.

6.6 Wind Farm Layout

The layout design of a wind farm is an important aspect since it has a substantial impact on the project's profitability. The wind farm layout concept is ideally developed with the aim of minimizing the LCOE. However, for practical reasoning the layout design is required to follow certain rules and guidelines. The existing rules and guidelines are derived from international standards or site-specific regulations. They are constructed to improve safety, reduce environmental impart and with respect to marine traffic.

Exact layout is out of the scope of this thesis, however three layout concepts are suggested on how the floating wind turbines can be installed. The layout of the hypothetical wind farm consisting of four 10 MW wind turbines, installed on the OO Star Wind Floater was based on the design of WindFloat Atlantic (2018), Hywind Tampen (2019) and other research studies, evaluated in the Literature review (2.4.2). This small wind farm will be producing power to the O&G installation 5 km away. Three different layouts was proposed and will be further investigated in Chapter 9. The layout concepts included one rectangular pattern, one single row and one "scattered" pattern.

7 Verification of Numerical Model

7.1 Hydrodynamic Analysis

7.1.1 First-Order Frequency Domain

The results from the first-order analysis performed in HydroD are presented in the following sections.

The figures on the left (a) are the results obtained with the panel model created in this thesis. The results are compared with the values from the LIFES50+ project 2018 presented on the right (b).

Added Mass

The frequency domain analysis shows satisfactory agreement with the added mass values from the LIFES50+ report.

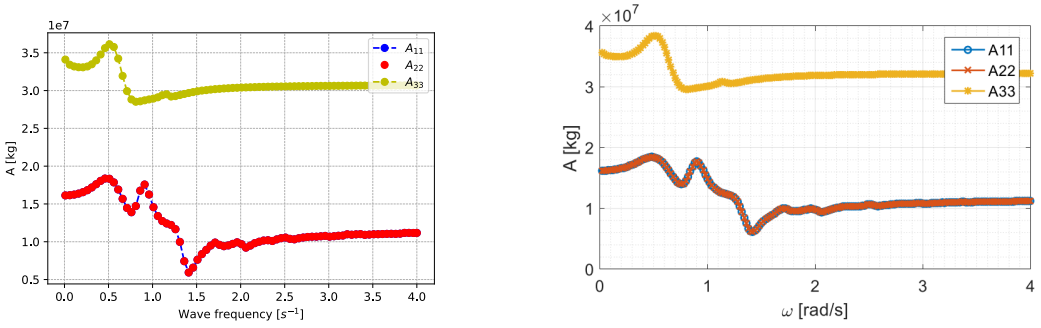

(a) (b)

Figure 7.1: Frequency dependent added mass in surge, sway and heave compared with the LIFES50+ results

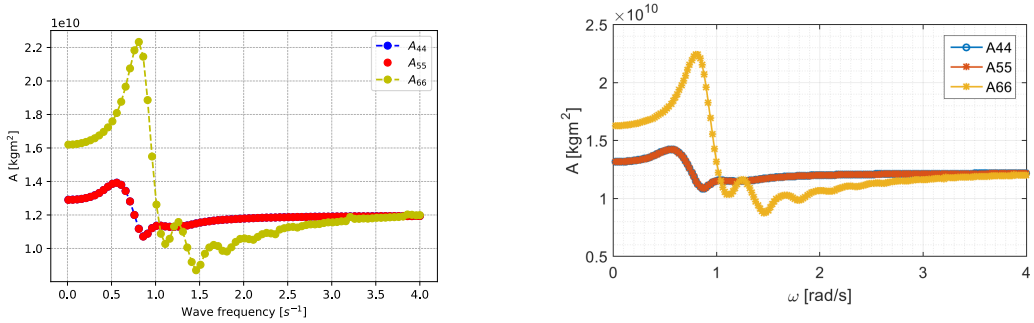

(a) (b)

Figure 7.2: Frequency dependent added mass in roll, pitch and yaw compared with the LIFES50+ results

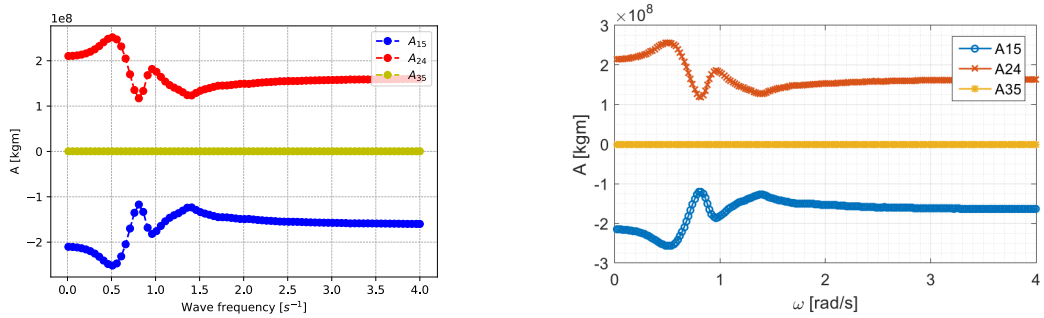

(a) (b)

Figure 7.3: Frequency dependent coupled added mass compared with the LIFES50+ results

Damping

The frequency domain analysis show satisfactory agreement with the damping mass values in surge and sway from the LIFES50+ report. However, for heave the numerical model underestimates the damping values compared to the projects.

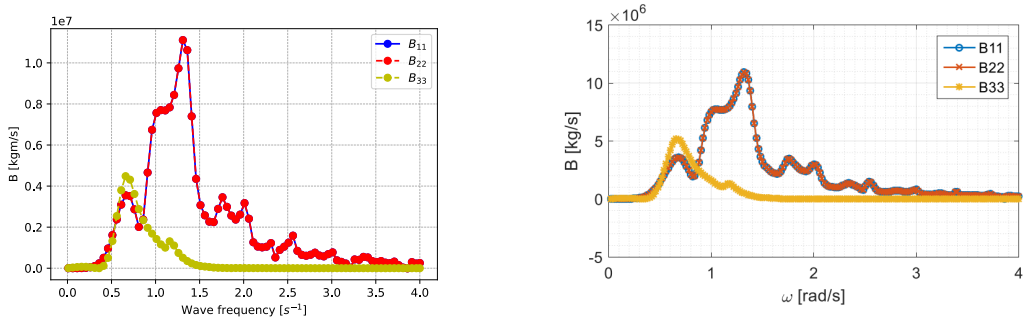

(a) (b)

Figure 7.4: Frequency dependent damping in surge, sway and heave compared with the LIFES50+ results

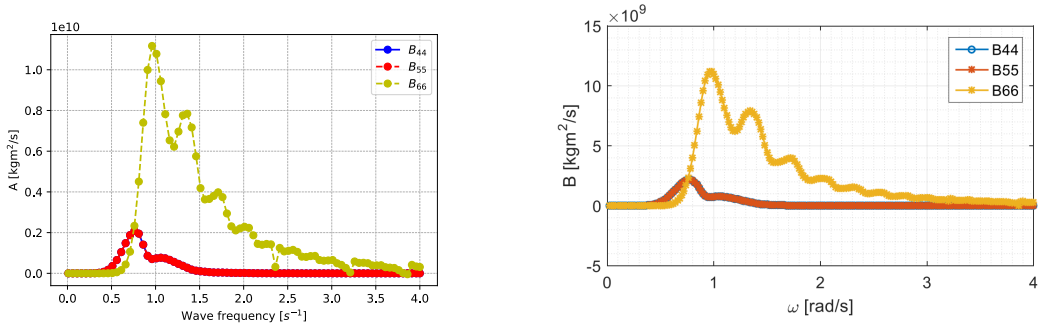

(a) (b)

Figure 7.5: Frequency dependent damping in roll, pitch and yaw compared with the LIFES50+ results

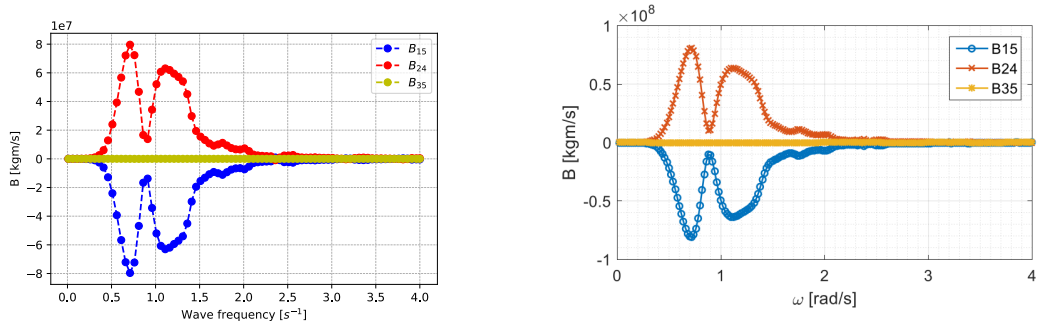

(a) (b)

Figure 7.6: Frequency dependent coupled damping compared with the LIFES50+ results

7.1.2 Second-Order Frequency Domain

Quadratic Transfer Functions

The difference-frequency excitation forces in surge, heave and moment in pitch are calculated with full QTF and Newman's approximation and presented in Figure 7.7, 7.8 & 7.9.

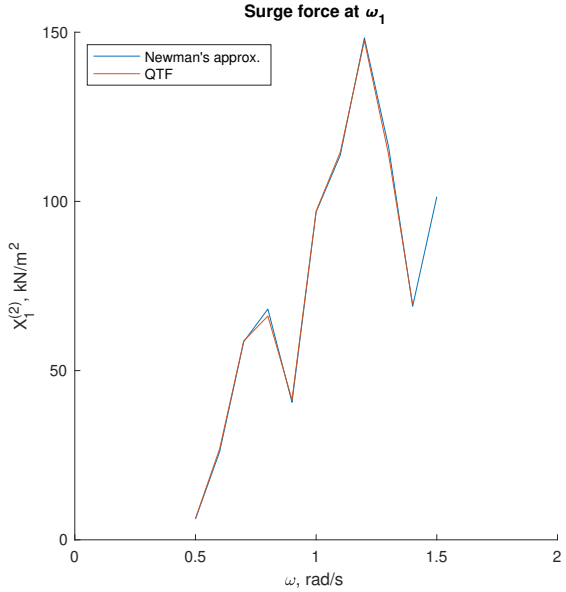

Figure 7.7: Surge QTF

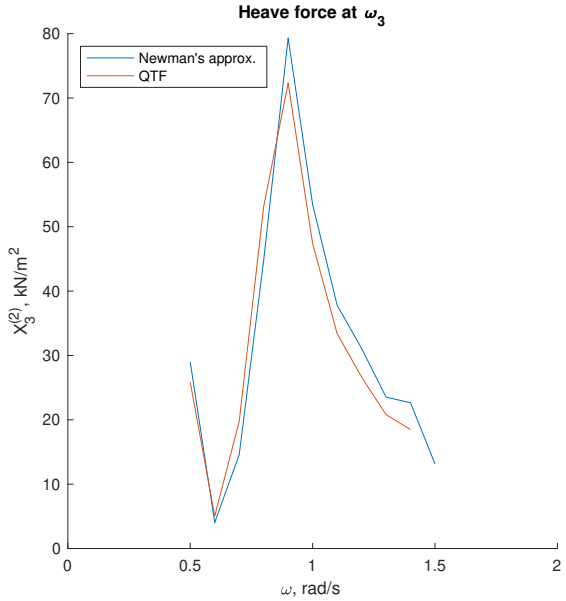

Figure 7.8: Heave QTF

The Newman's approximation was expected to underestimate the force, moment in heave and pitch due to the natural periods of the floater are lower than 100 s in these directions. The underestimation can be observed for the difference-frequency excitation moment in pitch in Figure 7.9.

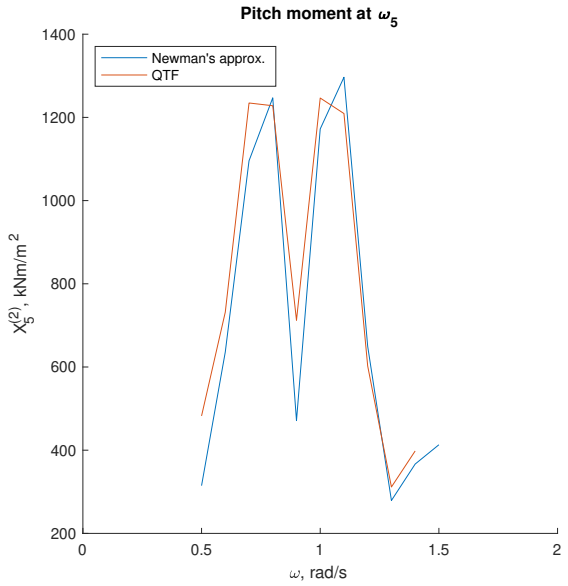

Figure 7.9: Pitch QTF

7.1.3 Mean Drift Forces

The mean drift forces was calculated in WADAM, using direct pressure integration and conservation of fluid momentum. The accuracy of the panel model can be identified by comparing the results of the two methods. The mesh is acceptable if there is a minor difference. The non dimensional mean drift force determined by the two approaches in surge is shown in Figure 7.10. The results from the two different approaches follow the same trend, however the difference between the two approaches is greater for large wave periods than short periods. The computed inaccuracy could be a source of error for further investigations. However, the mesh was deemed sufficient enough to be utilized in the analyses.

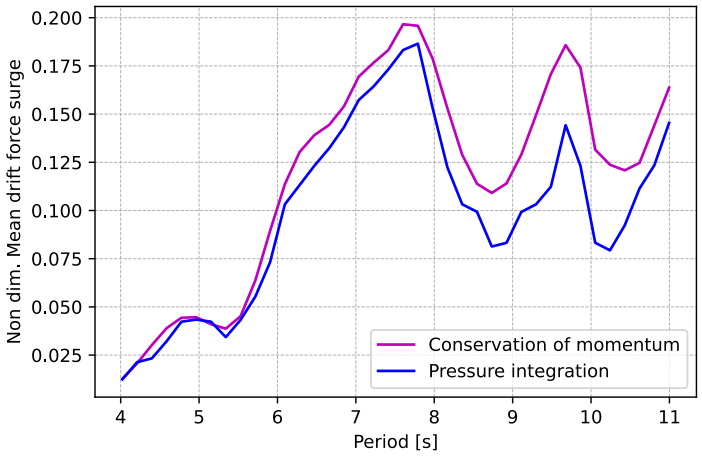

Figure 7.10: Comparison of non dimensional mean drift force in surge calculated by pressure integration and conservation of momentum

7.2 Decay Tests

Decay tests were performed in surge, heave, pitch, and yaw to determine the system's natural period. A numerical model of the substructure, turbine and mooring lines (the system) were analyzed in SIMA. For surge and heave, the decay tests were performed by applying a force in the desired motion. The force was administered in two stages: a ramp force for 100 seconds and a constant force for 200 s. The wind turbine began to oscillate with its natural frequency in the given degree of freedom when the force was released. Furthermore, by applying moments in the desired motion, the same method was repeated in pitch and yaw. The wind turbine was set in parked condition during the decay test, to prevent rotation of the blades. The significant wave height (H_s) was set to 0.01 m and the peak period (T_p) to 20 s. Table 7.1 presents information about the decay test parameters and Figure A.1 in the appendix shows the global response from the free decay tests in surge, heave, pitch and yaw.

Table 7.1: Decay test simulation parameters

Motion	**Force/Moment**	**Sim. length (s)**	**Ramp dur. (s)**	**Const. dur. (s)**
Surge	1000 kN	1200	100	200
Heave	10000 kN	1200	100	200
Pitch	180000 kNm	1200	100	200
Yaw	17000 kNm	1200	100	200

The system's natural period in surge, heave, pitch, and yaw were determined from the free decay simulations. The natural periods of the SIMA model are compared to the results from the LIFES50+ report (2018) in Table 7.2. The natural periods in surge, heave and pitch show agreement with the LIFES50+ results. However the largest difference is observed in yaw, where the natural period from LIFES50+ is 50.28 % higher than the SIMA model created in this thesis.

Table 7.2: Natural periods of the SIMA model compared to the LIFES50+ results

Motion	T_n**(SIMA)** [s]	T_n**(LIFES50+)** [s]	**Difference** [%]
Surge	182.4	185.19	1.52
Heave	20.3	20.92	3.05
Pitch	31.61	31.65	0.127
Yaw	68.6	103.09	50.28

7.3 Wind Turbine Performance

Verification of the wind turbine controller was performed through a constant wind test. This test verified the wind turbine's operation and determined which wind speeds resulted in the greatest surge and pitch offset. For 12 different wind speeds, 800 s time-domain simulations with constant wind were run. Simulations for wind speeds 4 m/s, 6 m/s, 10 m/s, 11.4 m/s, 12 m/s, 14 m/s, 16 m/s, 20 m/s, 22 m/s, and 24 m/s was carried out, as presented in Figure 7.11.

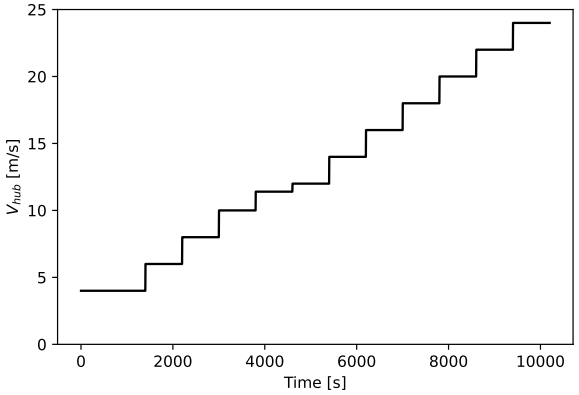

Figure 7.11: Step wind file covering the required wind speeds for the turbine

The wind was stationary with a shear profile, and the horizontal wind velocity was measured at the turbine's hub height. In order to eliminate the effects of incoming waves, the significant wave height was adjusted to 0.01 m and the peak period to 20 s.

Figure 7.12 shows performance curves of the wind turbine as a function of wind speed. The generator power and generator torque are constant after the rated wind speed is achieved.

Figure 7.13 presents the time series of the rotor speed and rotor thrust. The thrust on the rotor varies as the wind speed increases, and the floating substructure moves to its new equilibrium location, describing oscillations that decrease with time. In each DoF, these oscillations occur at the natural frequency. When the wind speed is changed to a higher wind speed, the structure continues to oscillate in surge due to the long surge natural period.

These events were also observed in the LIFES50+ project (2018) and they explain it as although the controller was calibrated to give positive damping in pitch in the full-load region, the surge motion appears to be less damped for wind speeds over rated wind speed. Further research indicated that the aerodynamic damping in surge for these wind speeds is negative or zero, due to the controller. However, it was also mentioned that hydrodynamic damping leads to a positive global damping of the surge mode under real environmental situations with wind, waves and current.

It was decided to lower the natural frequency of the pitch controller to a value below the pitch natural frequency of the FWT. This value was decided to be $\omega = 0.03$ Hz, in accordance with T. J. Larsen and Hanson (2007). As a result, the blade-pitch controller proportional (K_P) and integral gain (K_I) was set to 2.6224E-01 and 3.35308E-02, respectively. It was also decided to lower the values of the blade pitch angle for every wind speed above rated wind speed with 1 degree. This reduced the fluctuations of the rotor speed and pitch motions. However, it seems like the FWT regardless encounter negative damping. Further control measures can almost certainly lead to higher performance, and this is something that should be pursued in the future. The performance of the FWT was deemed acceptable, however it can be a source of error in the study in operational conditions.

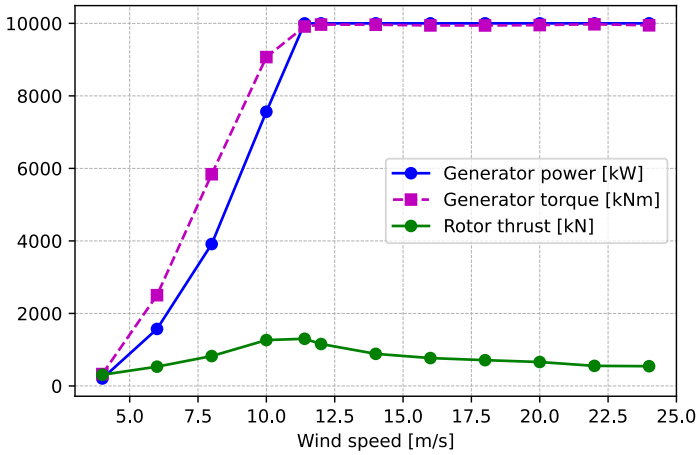

Figure 7.12: Wind turbine performance curves

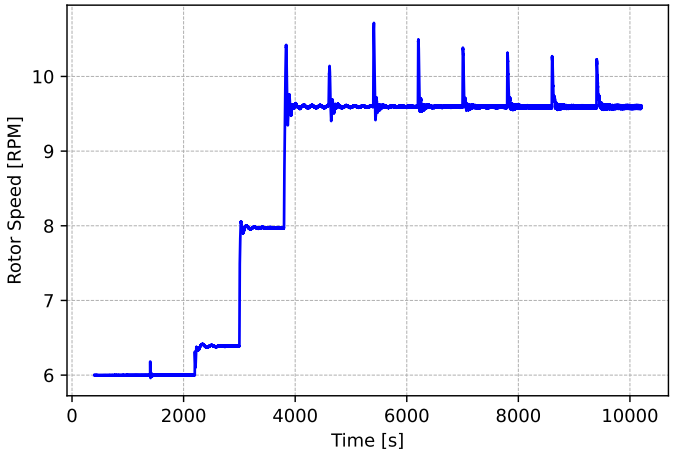

Figure 7.13: Rotor speed as a function of time

Figure 7.14 shows the offsets in surge and pitch as a function of time. The results from the constant wind time-series are presented to the left and compared to the results from the LIFES50+ project. From the results it can be seen that the mean offset was largest at the rated wind speed (approximately 4000 s). The incoming wind was input at 0°.

The surge and pitch offsets was slightly larger for the results in this thesis compared to the Lifes50+ project.

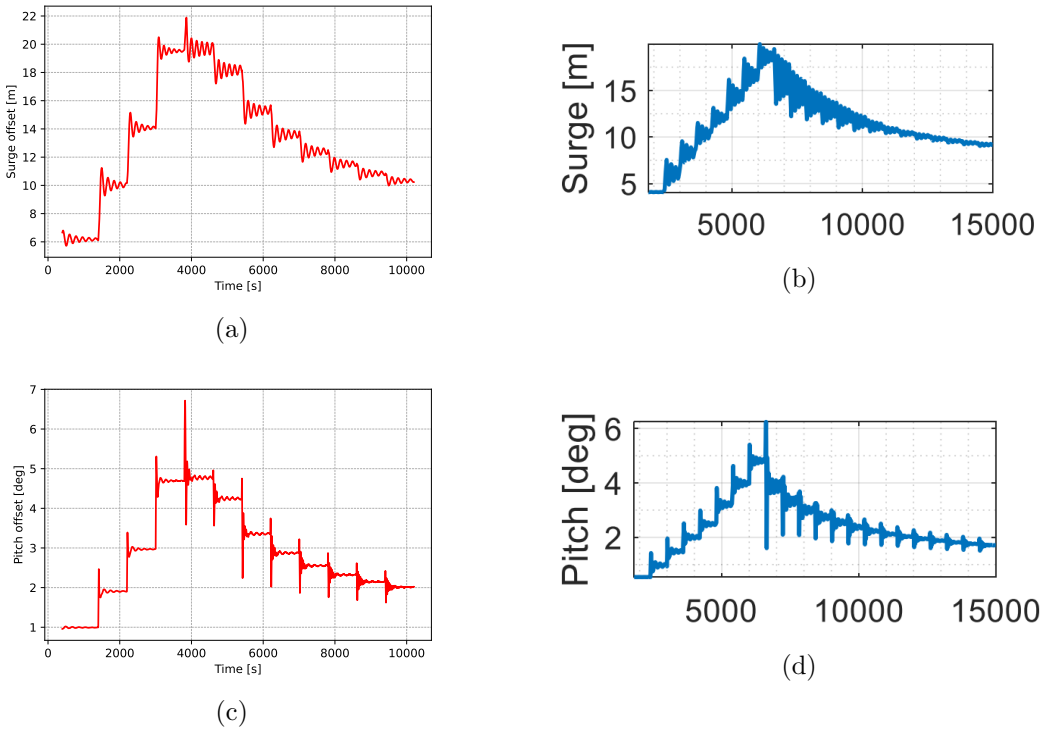

(a) (b) (c) (d)

Figure 7.14: Surge and pitch offsets compared to the LIFES50+ results

8 Study of OO Star Wind Floater in Operational and Extreme Conditions

The investigation of the floating wind turbines under six environmental load conditions are presented in this section. The FWT was analysed in SIMA under the environmental load cases presented in Table 5.4. All analyses were performed on the following three models with and without wind loads:

- First-order frequency domain model (1.M).
- Second-order wave drift force with Newman's approximation (2.M).
- Second-order difference-frequency wave force with full QTF (3.M).

The simulations were run for a duration of 4000 second, i.e., one-hour and 12 minutes each simulation. The first 1000 s for the time-domain simulation in SIMA were neglected to exclude the transient phase prior to the statistical analyses. This section presents the FWTs behaviour under operational (1.OP & 2.OP), near cut-out (1.NC & 2.NC) and extreme (1.EX & 2.EX) conditions with and without wind loads.

8.1 Motion Response

The standard deviation of the rigid body movements in surge, heave, and pitch, were determined using statistical analysis when the wave's direction was 0 degrees. Additionally, the response spectra and maximum values in surge are presented. The first-order model (1.M) and the two second-order models (2.M and 3.M) were simulated, and comparison of results followed by discussion were carried out. The response of the linear model is compared with the difference-frequency full QTF model. Furthermore, a comparison of the results from the second order wave drift calculated with Newman's approximation (2.M) and full QTF model was conducted.

8.1.1 Comparison of Linear (1.M) and Full QTF (3.M) Models

The response of the linear model is compared with the full QTF model. The standard deviation of platform motions in surge, heave, and pitch for all six environmental load cases are presented in Table 8.1, respectively. Load case 1.OP and 2.OP represent operational condition, where the mean annual wind speed was $8.75 m/s$.

These load cases correspond to the most probable environmental conditions that the FWT would encounter. The analysis conducted with wind and wave loads presents a complete agreement between the first-order model (1.M) and the full QTF model (3.M). The analysis conducted without wind loads presents a difference of 69.57 % in surge between the first-order model and the model accounting for second-order effects, the full QTF model (3.M). This highlights the importance of considering such effects when analysing the motions of a semi-submersible.

Load case 1.NC and 2.NC represent near cut-out condition, which are still within the operational conditions of the FWT. The wind speed at hub-height is close to the cut-off speed. The standard deviations of the motions are presented in Table 8.1 below load cases for operational condition. The difference between the standard deviations of the load cases with (1.NC) and without wind (2.NC) are considerably small in comparison with load cases 1.OP and 2.OP. However, the responses are larger and the difference between the first-order model (1.M) and the full QTF (3.M) accounting for the second-order effects are larger for the motions in surge and pitch than in heave.

Load case 1.EX and 2.EX represent extreme condition with and without wind loads. As anticipated, the platforms motion responses increase with increasing environmental conditions. Consequently, it was observed increased responses for all DoFs in extreme environmental conditions. The motion responses for surge and pitch of load case 1.EX and 2.EX are larger than near cut-out load cases (1.NC & 2.NC). The standard deviation of surge motions does not experience notable change from load case 1.EX to 2.EX for both models. According to the literature study conducted on second-order effects, difference-frequency loads have limited impact under extreme environmental conditions (2.2).

Table 8.1: Standard deviation of platform motions in surge, heave and pitch Linear and Full QTF models

Load Case	**Model**		**Difference [%]**
1.OP	Linear 1.M	Full QTF 3.M	
Surge [m]	0.99	0.99	0
Heave [m]	0.06	0.06	0
Pitch [deg]	1.17	1.17	0
2.OP	Linear 1.M	Full QTF 3.M	Difference [%]
Surge [m]	0.23	0.39	69.57
Heave [m]	0.04	0.05	25
Pitch [deg]	0.07	0.08	14.29
1.NC	Linear 1.M	Full QTF 3.M	Difference [%]
Surge [m]	0.97	1.37	41.24
Heave [m]	0.20	0.21	4.99
Pitch [deg]	0.51	0.54	5.88
2.NC	Linear 1.M	Full QTF 3.M	Difference [%]
Surge [m]	1.18	1.68	42.37
Heave [m]	0.20	0.20	0
Pitch [deg]	0.39	0.47	20.51
1.EX	Linear 1.M	Full QTF 3.M	Difference [%]
Surge [m]	4.23	4.41	4.26
Heave [m]	4.71	4.40	-6.58
Pitch [deg]	4.29	4.74	10.49
2.EX	Linear 1.M	Full QTF 3.M	Difference [%]
Surge [m]	4.26	4.60	7.98
Heave [m]	4.72	4.83	2.33
Pitch [deg]	4.32	5.29	22.45

The maximum and mean value in the surge motion for all load cases with and without wind loads are presented in Table 8.2. The maximum value for surge motion with wind for load case operational condition (1.OP), for the first-order model (1.M) is 27.64 m, with a 1.34 % difference between the full QTF (3.M), which is equivalent to 0.37 m. The maximum value of the surge offset for the load case wind for the full QTF model accounting for second-order effects (3.M), is 43.3 % larger than the same model without wind load. This corresponds to 15.66 m, indicating that the wind loads are a significant factor in determining the offset in surge motion for this environmental condition.

The mean values for the linear model (1.M) and full QTF model (3.M) in near cut-out load cases, display a decrease of surge motion offset from load case 1.NC to 2.NC for the linear (1.M) and the full QTF (3.M) models. The decrease of mean surge motion is by 27 %, 5.96 m for linear model (1.M) and a decrease of 20 %, 4.99 m for the full QTF model (3.M) from load case 1.NC to 2.NC. Additionally, the full QTF model exhibits a slight increase in maximum values in comparison to the linear model.

The mean and maximum values of the surge offset for load cases of 1.EX and 2.EX are relatively unchanged for both the linear and full QTF model. The slight discrepancy lies with the full QTF model accounting for second-order effects, underestimating the linear models mean surge response by 0.61 %.

Table 8.2: Maximum and mean values of platform motions in surge Linear and Full QTF models

Load Case	**Model**		**Difference [%]**
	Linear 1.M	Full QTF 3.M	
1.OP - Max [m]	27.64	28.01	1.34
2.OP - Max [m]	11.98	13.70	14.36
1.NC - Max [m]	25.61	29.65	15.78
2.NC - Max [m]	20.02	25.21	25.92
1.EX - Max [m]	45.61	45.71	0.22
2.EX - Max [m]	45.41	46.30	1.96
	Linear 1.M	Full QTF 3.M	Difference [%]
1.OP - Mean [m]	25.57	25.85	1.10
2.OP - Mean [m]	11.20	12.52	11.79
1.NC - Mean [m]	22.10	24.80	11.71
2.NC - Mean [m]	16.14	19.81	22.74
1.EX - Mean [m]	31.62	31.43	-0.60
2.EX - Mean [m]	31.29	31.10	-0.61

8.1.2 Comparison of Full QTF (3.M) and Newman's Approximation (2.M) Models

The responses of the second-order wave drift calculated with Newman's approximation (2.M) and second-order full QTF model (3.M) in all environmental conditions considered with and without wind loads were compared. The standard deviation of the platform motions in surge, heave, and pitch for all load cases are presented in Table 8.1.

Load cases under operational condition with and without wind loads (1.OP & 2.OP), the motion responses from the second-order wave drift calculated with Newman's approximation model (2.M) coincides perfectly with the full QTF model (3.M). This gives an indication that Newman‘s approximations for slow-drift effects and Morison model for quadratic damping gives a reasonable predication of hydrodynamic responses. However, there is a significant increase in motion response in surge and pitch for the second-order effects calculated with Newman's approximation model (2.M) and the full QTF model (3.M) in load case 1.OP compared to 2.OP. The significant increase in motion response of surge both models is 60.6 % compared from load case 2.OP, without wind loads to 1.OP.

Load cases for near cut-out (1.NC & 2.NC) motion responses display a relatively strong agreement between the full QTF and Newman´s approximation. The largest difference between the two models is in the standard deviation of surge motion of 7.14 % for load case 2.NC without wind loads. However this only corresponds to 0.12 m. The only slight misalignment between the two models in the extreme load cases (1.EX & 2.EX) is in pitch motion with an increase of 10.97 % for the second-order effects considered by the full QTF model (3.M) as presented in Table 8.1.

Table 8.3: Standard deviation of platform motions in surge, heave and pitch Full QTF and Newman's models

Load Case	**Model**		**Difference [%]**
1.OP	Full QTF 3.M	Newman's 2.M	
Surge [m]	0.99	0.99	0
Heave [m]	0.06	0.06	0
Pitch [deg]	1.17	1.18	0.85
2.OP	Full QTF 3.M	Newman's 2.M	Difference [%]
Surge [m]	0.39	0.39	0
Heave [m]	0.05	0.05	0
Pitch [deg]	0.08	0.08	0
1.NC	Full QTF 3.M	Newman's 2.M	Difference [%]
Surge [m]	1.37	1.38	0.73
Heave [m]	0.21	0.20	-4.76
Pitch [deg]	0.54	0.57	5.56
2.NC	Full QTF 3.M	Newman's 2.M	Difference [%]
Surge [m]	1.68	1.80	7.14
Heave [m]	0.20	0.20	0
Pitch [deg]	0.47	0.49	4.26
1.EX	Full QTF 3.M	Newman's 2.M	Difference [%]
Surge [m]	4.41	4.57	3.63
Heave [m]	4.40	4.82	9.55
Pitch [deg]	4.74	5.26	10.97
2.EX	Full QTF 3.M	Newman's 2.M	Difference [%]
Surge [m]	4.60	4.61	0.22
Heave [m]	4.83	4.86	0.62
Pitch [deg]	5.29	5.34	0.95

The maximum and mean values of surge motion for the second-order wave drift with Newman's approximation (2.M) and full QTF model (3.M) are presented in Table 8.2. The maximum values of offset in surge for each load case are important to take into consideration due to correlation with the mooring line tension. The largest difference between maximum values is an underestimation of 28.9 % under extreme load case (1.NC), which corresponds to 18.85 m. Implying, a significant increase in surge motion for the full QTF model (3.M).

Due to the alignment of wave and wind loads the responses generated for maximum values are larger. Thus, in a case of misalignment loads the wind speed is expected to be substantially lower.

Table 8.4: Maximum and mean values of platform motions in surge Full QTF and Newman's models

Load Case	**Model**		**Difference [%]**
	Full QTF 3.M	Newman's 2.M	
1.OP - Max [m]	28.01	28.02	0.04
2.OP - Max [m]	13.70	13.67	-0.22
1.NC - Max [m]	29.65	29.80	0.51
2.NC - Max [m]	25.21	25.70	1.94
1.EX - Max [m]	65.31	46.46	-28.9
2.EX - Max [m]	46.30	46.33	0.06
	Full QTF 3.M	Newman's 2.M	Difference [%]
1.OP - Mean [m]	25.85	25.85	0
2.OP - Mean [m]	12.52	12.53	0.08
1.NC - Mean [m]	24.80	24.80	0
2.NC - Mean [m]	19.81	19.72	-0.45
1.EX - Mean [m]	31.43	31.30	-0.41
2.EX - Mean [m]	31.10	31.15	0.16

8.1.3 Response spectra

In order to assess the contribution from the hydrodynamic and aerodynamic loads, the power spectral density (PSD) of the loads and FWT responses are presented. The platform responses have been analysed for load cases OP (1 & 2), NC (1 & 2) and EX (1 & 2) and the PSD for heave, pitch and surge motions of the FWT presented in Figures 8.1 - 8.5, respectively.

The influence of second-order forces on the FWTs responses and forces were reviewed in the literature review in Chapter 2.2. Several research projects have explored the influence of the QTF and Newman's approximation. Generally, the slow-drift forces and responses for the relevant DoF's natural frequency are underestimated by Newman's approximation.

Load Case: 1.OP

The time series and power spectral density (PSD) in surge, heave, and pitch motions of the first-order model (1.M), second-order effects calculated with Newman´s approximation (2.M) and full QTF model (3.M) for operational condition with and without wind loads (1.OP & 2.OP), are presented in Figure 8.1 - 8.2. The wind speed at hub height ($U_{W,119}$) was 35 m/s and the waves had a significant wave height of (H_s) of 1.90 m and peak period (T_p) of 7.25 s. Thus, the peak wave frequency is 0.86 rad/s.

The motions at low frequencies are underestimated by linear model apart from surge and heave natural frequencies presumably being excited by the dominating wind loads leading to an overestimation by the linear model in load case 1.OP. Motions in surge have one large peak at $\omega = 0.03$ rad/s and this coincides with the natural frequency of the motion.

The heave motion is greatly influenced by the wave loads, but it is also excited at the natural frequency $\omega = 0.31$ rad/s. The influence of second-order loads was apparent for surge and pitch motion, in accordance with Duarte et al. (2014). However, it appears that the linear model also takes inot account some of the second-order effetcs. This behavior was not expected and may be due to numerical errors in the coupled time-domain analysis.

The pitch motion has a single peak before it reaches the natural frequency and is coupled with surge. This behavior was not expected and several measures were taken to counteract and eliminate these effects, but due to time limitations this was not solved. A possible solution was to adjust the fairleads to a position below the free surface. This lead to a double peak pitch PSD in the near-cut off condition 1.NC, with one of the peaks located at the natural frequency. However, this did not change the behavior at the operational conditions 1.OP and 2.OP. It was expected that the natural frequency in pitch would be excited and the error sources may be numerical modelling or simulation errors. Thus, it was decided to present the results from the model with mooring lines attached above the free surface. It is strongly suggested to perform investigations into these discrepancies during further work.

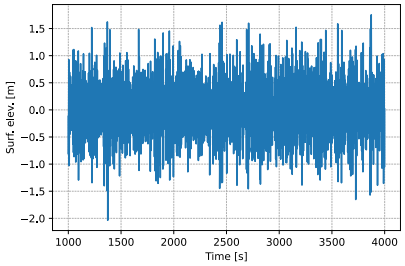

(a) Wave elev. time series 1.OP

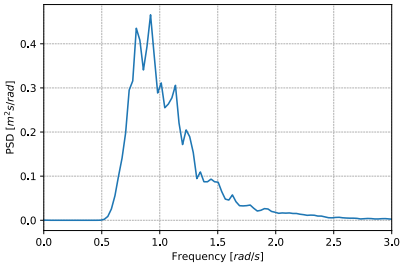

(b) Wave elev. PSD 1.OP

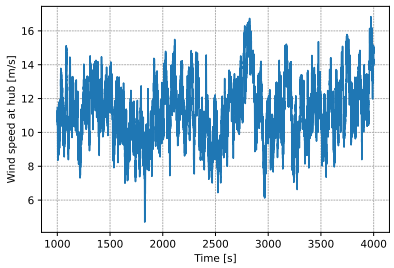

(c) Wind speed time series 1.OP

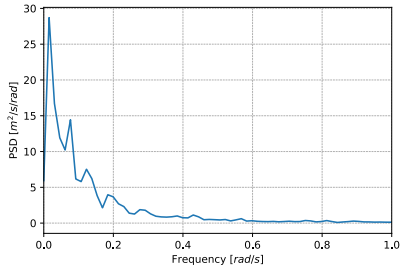

(d) Wind speed PSD 1.OP

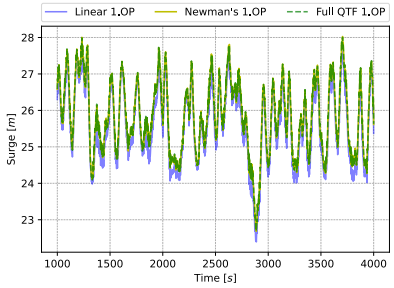

(e) Surge time series 1.OP

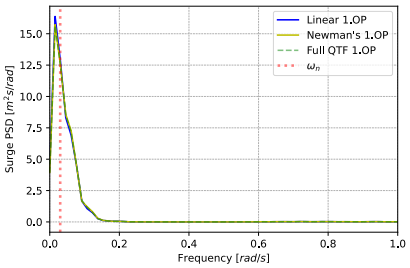

(f) Surge PSD 1.OP

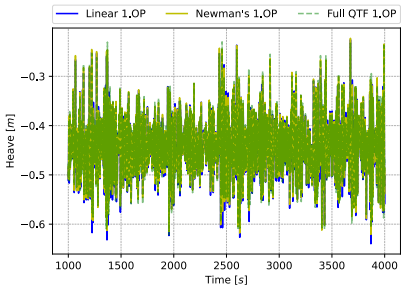

(g) Heave time series 1.OP

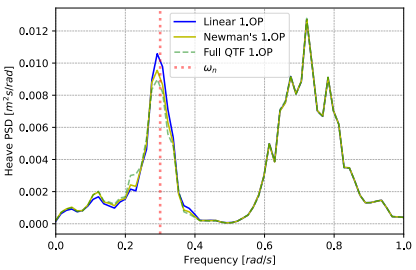

(h) Heave PSD 1.OP

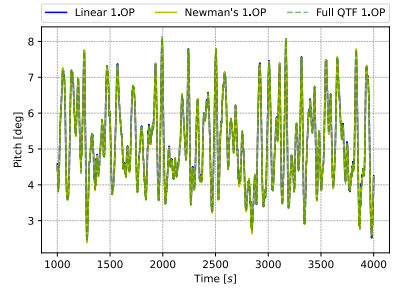

(i) Pitch time series 1.OP

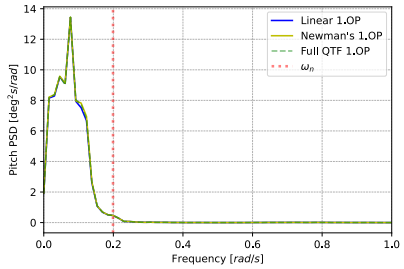

(j) Pitch PSD 1.OP

Figure 8.1: Response to load case 1.OP

Load Case: 2.OP

The response PSDs and time series of surge, heave and pitch of load case 2.OP are presented in Figure 8.2. The motion responses for this load case are considerably lower than 1.OP due to removal of wind loads. At low frequencies, Newman's approximation underestimates the heave response slightly, as expected. The pitch spectra for load case 2.OP presents a lower response than for load case 1.OP. Correspondingly, the spectra for heave and surge motions of load case 2.OP result in lower values on the than case 1.OP, demonstrating the influence wind load have on these motions regardless of heave motions being only influenced by wave loads.

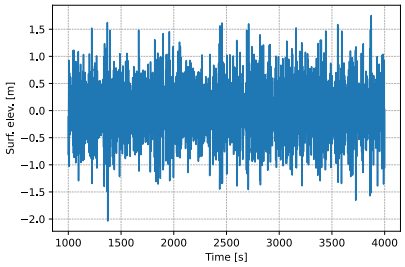

(a) Wave elev. time series 2.OP

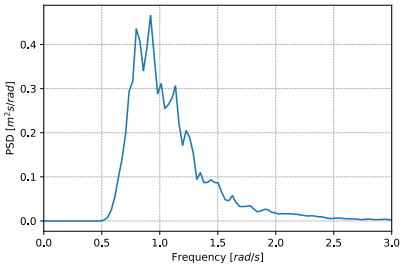

(b) Wave elev. PSD 2.OP

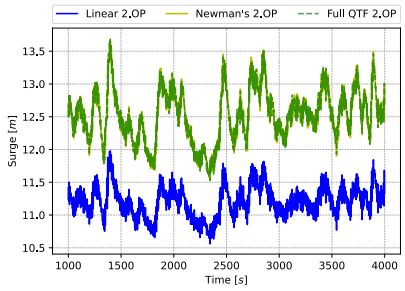

(c) Surge time series 2.OP

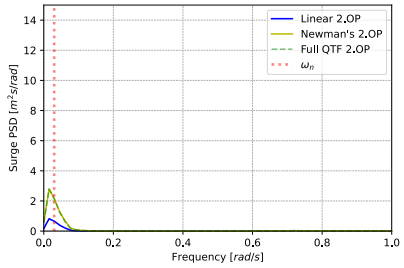

(d) Surge PSD 2.OP

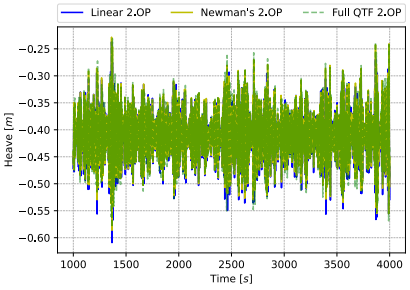

(e) Heave time series 2.OP

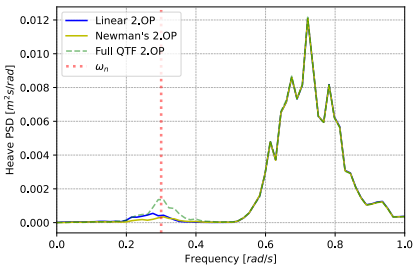

(f) Heave PSD 2.OP

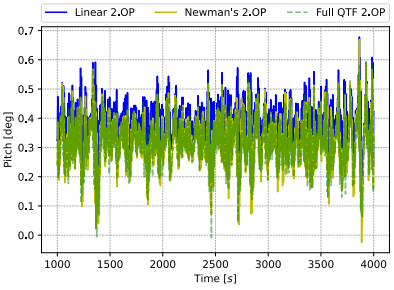

(g) Pitch time series 2.OP

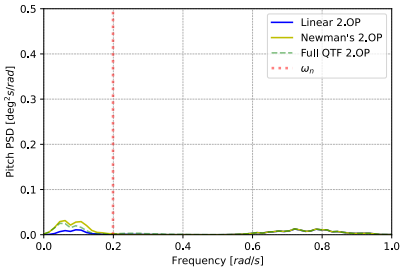

(h) Pitch PSD 2.OP

Figure 8.2: Response to load case 2.OP

Load Case: 1.NC

The time series and power spectral density of surge, heave and pitch motions of the three models for near cut-out conditions under conditions (1.NC and 2.NC) are presented in Figures 8.3 - 8.4. The wind speed at hub height was 25 m/s, the wave had a significant wave height of 5.08 m and peak period of 8.38 s. The surge and heave spectra display a correlation with load case 1.OP by following the same trend. The wind loads excited the natural frequencies of surge and heave and the wave loads dominate majority of the substructure's movements. However, the spectra displays a considerable increase in magnitude of both surge and heave motions in y-axis in comparison to load case 1.OP. The pitch motion displays a single peak, with an underestimation by the linear model, which does not account for second-order effects. This is consistent with the review presented in literature study in Chapter 2.2.

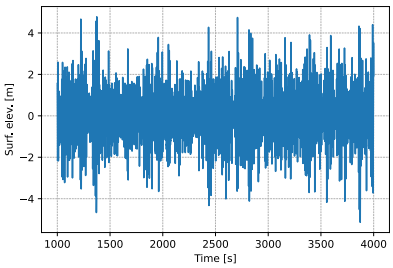

(a) Wave elev. time series 1.NC

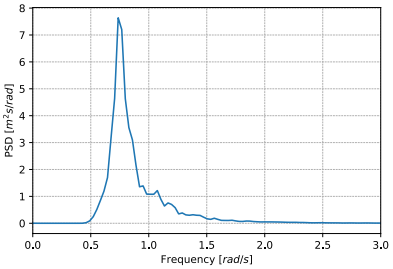

(b) Wave elev. PSD 1.NC

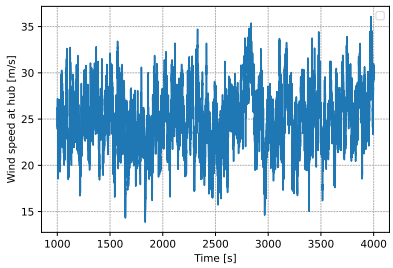

(c) Wind speed time series 1.NC

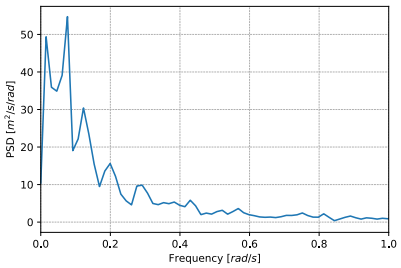

(d) Wind speed PSD 1.NC

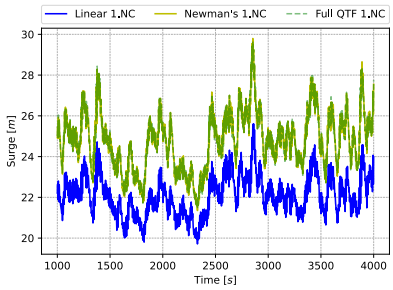

(e) Surge time series 1.NC

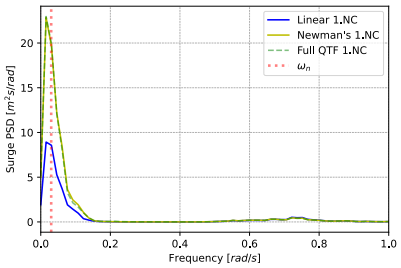

(f) Surge PSD 1.NC

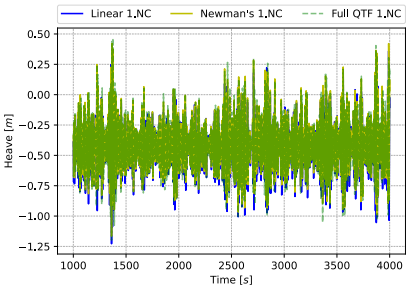

(g) Heave time series 1.NC

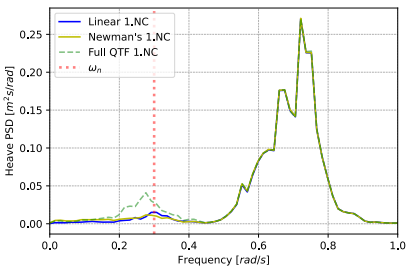

(h) Heave PSD 1.NC

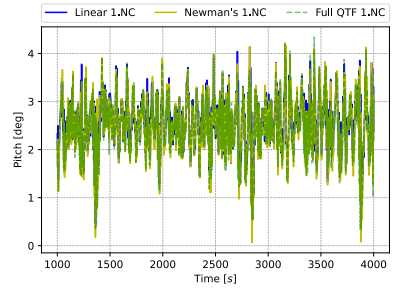

(i) Pitch time series 1.NC

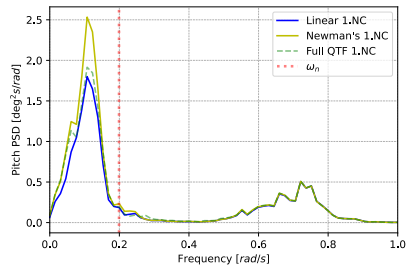

(j) Pitch PSD 1.NC

Figure 8.3: Response to load case 1.NC

Load Case: 2.NC

The response PSDs and time series of surge, heave and pitch of load case 2.NC are presented in Figure 8.4. The motion responses for this load cases follow the same trend as case 1.NC, with a reduced magnitude. Additionally, Newman's approximation underestimates responses in pitch and surge as expected.

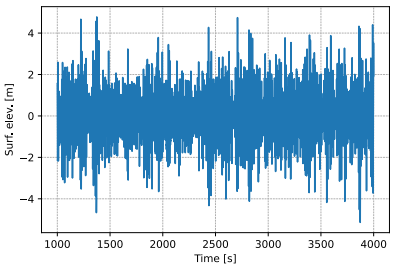

(a) Wave elev. time series 2.NC

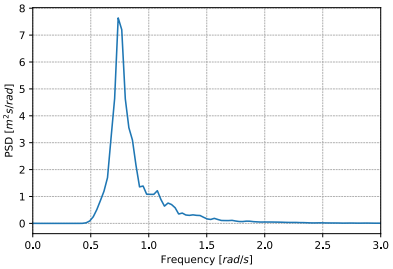

(b) Wave elev. PSD 2.NC

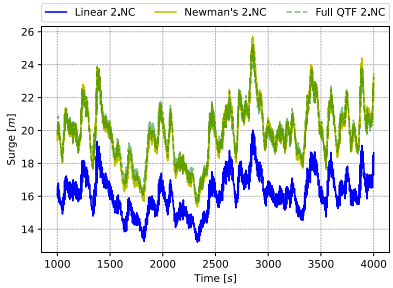

(c) Surge time series 2.NC

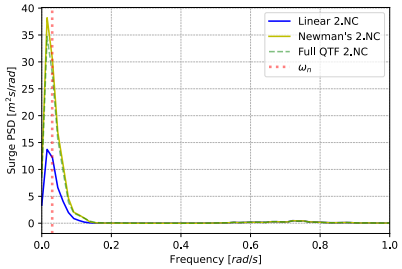

(d) Surge PSD 2.NC

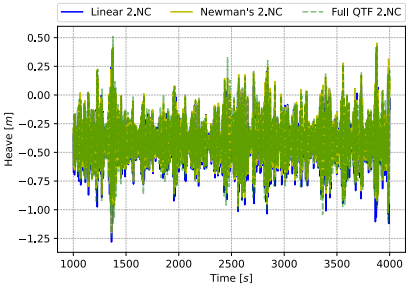

(e) Heave time series 2.NC

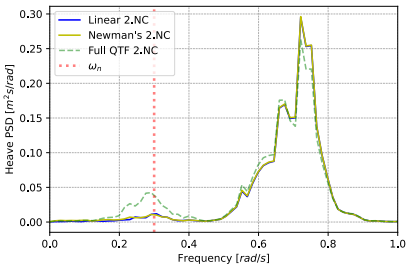

(f) Heave PSD 2.NC

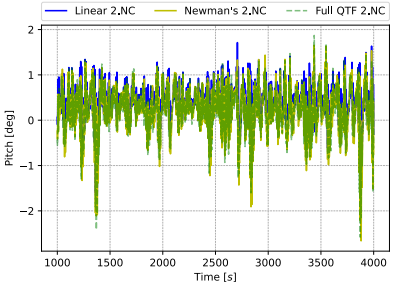

(g) Pitch time series 2.NC

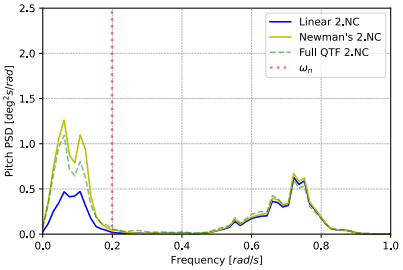

(h) Pitch PSD 2.NC

Figure 8.4: Response to load case 2.NC

Load Case: 1.EX

The time series and power spectral densities of surge, heave and pitch motions of all three models under extreme conditions are presented in Figures 8.5 - 8.6. The wind speed was $U_{W,119} = 35$ m/s and the wave had a significant wave height was 15.5 m and a peak period of $T_p = 16.9$ s. The turbine blades are feathered, thus not able to rotate due to parked condition under such substantial loads. The purpose of pitching the turbine's rotor blades is to minimize thrust and preserve the turbine during extreme conditions. The angle of attack on the air foils decreases as the blades are pitched, and as a result, the lift force reduces. The lift force is mainly accountable for the thrust force as presented in Chapter 3.2.

As observed in the spectra all motions are larger in magnitude for both load cases. The peaks of all motions in the spectra coincide well with the natural frequency of the respective motions as displayed in all figures with a red dotted vertical line. The full QTF and Newman's approximation models displays a considerable deviation from the linear models in surge and pitch motions. As predicted, the linear model displays an underestimation of the response in surge and pitch. However, it shows an overestimation in heave. The results obtained for extreme load cases 2.EX coincide with load case 1.EX.

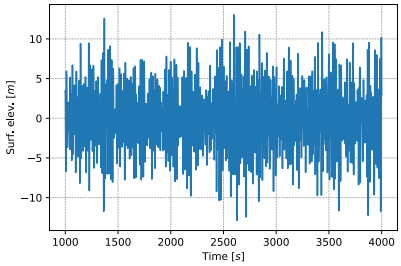

(a) Wave elev. time series 1.EX

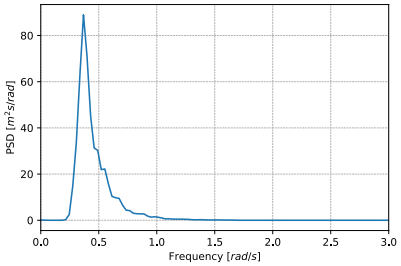

(b) Wave elev. PSD 1.EX

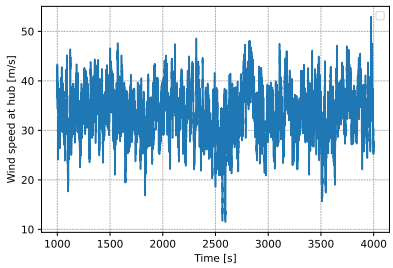

(c) Wind speed time series 1.EX

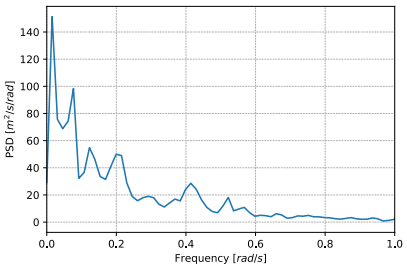

(d) Wind speed PSD 1.EX

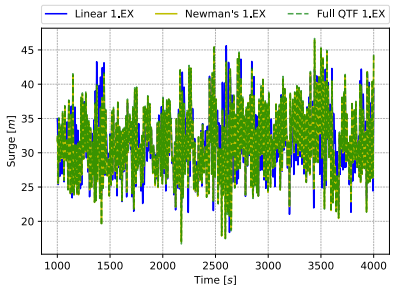

(e) Surge time series 1.EX

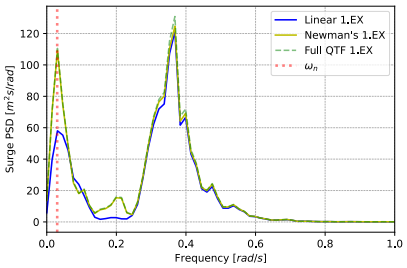

(f) Surge PSD 1.EX

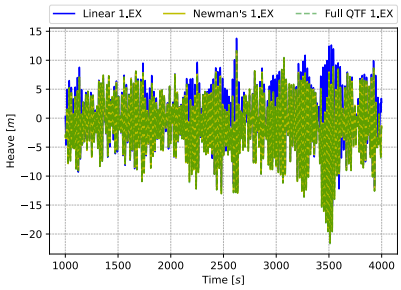

(g) Heave time series 1.EX

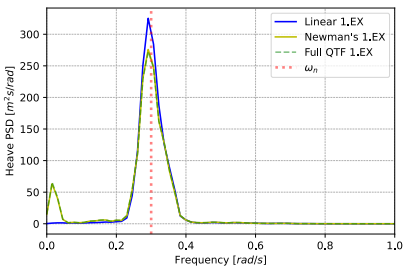

(h) Heave PSD 1.EX

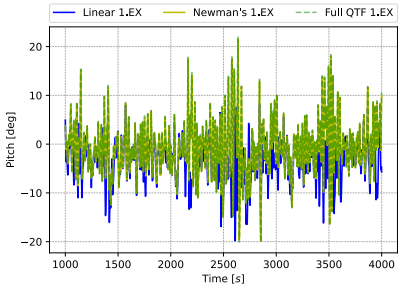

(i) Pitch time series 1.EX

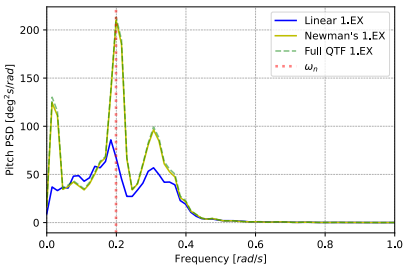

(j) Pitch PSD 1.EX

Figure 8.5: Response to load case 1.EX

Load Case: 2.EX

The response PSDs and time series of surge, heave and pitch of load case 2.EX are presented in Figure 8.6.

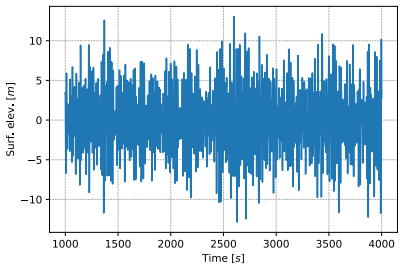

(a) Wave elev. time series 2.EX

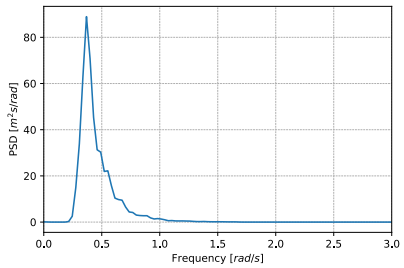

(b) Wave elev. PSD 2.EX

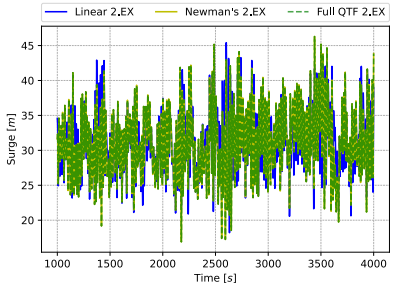

(c) Surge time series 2.EX

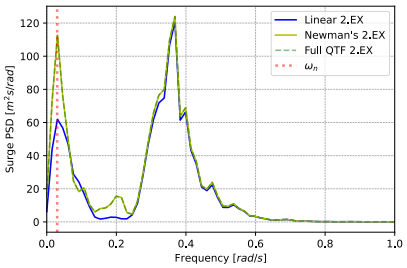

(d) Surge PSD 2.EX

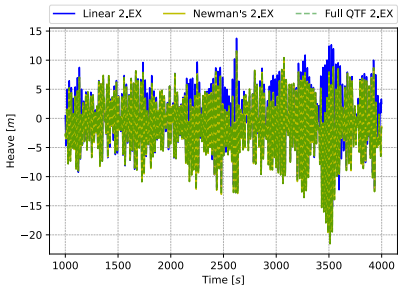

(e) Heave time series 2.EX

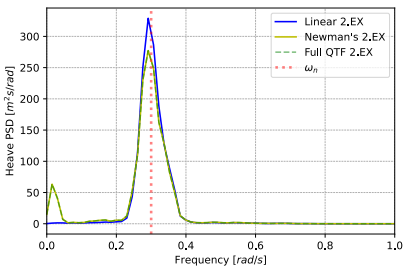

(f) Heave PSD 2.EX

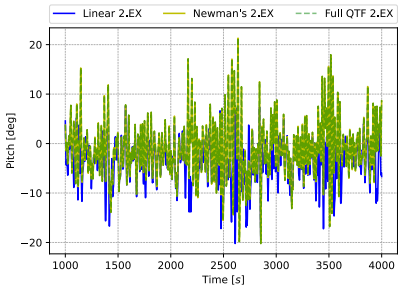

(g) Pitch time series 2.EX

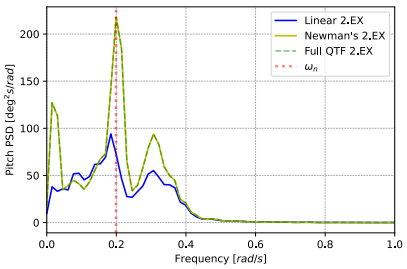

(h) Pitch PSD 2.EX

Figure 8.6: Response to load case 2.EX

8.2 Aerodynamic Loads

The standard deviation of the aerodynamic loads acting along the shaft of the wind turbine in three environmental load cases for the difference-frequency full QTF model (3.M). The standard deviations are presented in Table 8.5. The aerodynamic force acts in the x-direction, while the aerodynamic moments act in y-direction and both at the shaft of the turbine. These loads contribute to surge and pitch response, as evidenced by the difference in response values between the load cases with and without wind. The forces at work are considerably smaller in comparison to first-order wave loads, thus only the full QTF model is presented. The aerodynamic forces increase with increasingly wind speed, wave height and peak period. However, the difference between operational and extreme condition is noticeable.

Table 8.5: Standard deviation of the aerodynamic loads operating on the wind turbine

Load case	**Aerodynamic force**	**Aerodynamic moment**
	[kN]	[kNm]
1.OP	260.4	4902
1.NC	141.9	8202
1. EX	24.90	187.8

8.3 Hydrodynamic loads

Additional to structural and aerodynamics loads accessed above, hydrodynamic loads on the floating substructure were analysed. The standard deviation deviation and maximum values of 1^{st} and 2^{nd} order wave loads in surge, heave and pitch are presented in Table 8.6 and 8.7. The 1^{st} order wave, 2^{nd} order wave drift and 2^{nd} order QTF wave loads in surge, heave and pitch was investigated for the three different load models.

For load case 1.OP, the 2^{nd} order wave drift load is 1.2 % of the 1^{st} order wave load in surge. The 2^{nd} order QTF wave load in surge is 2.5 % of the 1^{st} order wave load. In heave, the fraction is approximately the same and in pitch, the 2^{nd} order wave drift load is 0.66 % of the 1^{st} order wave load. In addition, the 2^{nd} order QTF wave load in pitch is 2.8 % of the nth1 order wave load.

For load case 1.NC, the trend from load case 1.OP is followed, with the 2^{nd} order values in surge, heave and pitch being under 6 % of the 1^{st} order wave loads.

For load case 1.EX, the 2^{nd} order wave drift and QTF loads are 2.0 % and 2.1 % of the 1^{st} order wave load in surge. In heave, however the values are 60 % and 61 % 1^{st} order wave load, respectively. In pitch, the 2^{nd} wave loads also increased in comparison to 1.OP and 1.NC, being 21 % of the nth1 order wave load.

Table 8.6: Standard deviation of 1. and 2. order wave loads in surge, heave and pitch

Load Case	**Wave force**		
1.OP	1^{st} order	2^{nd} order wave drift	2^{nd} order QTF
Surge [kN]	2833	34.58	70.84
Heave [kN]	1445	21.03	42.70
Pitch [kNm]	37501	249.2	1038
1.NC	1^{st} order	2^{nd} order wave drift	2^{nd} order QTF
Surge [kN]	7411	176.4	407.8
Heave [kN]	5699	163.7	285.4
Pitch [kNm]	137802	2004	7015
1.EX	1^{st} order	2^{nd} order wave drift	2^{nd} order QTF
Surge [kN]	22202	452.4	460.0
Heave [kN]	12755	7742	7874
Pitch [kNm]	319717	67360	68478

Table 8.7: Maximum values of 1. and 2. order wave loads in surge, heave and pitch

Load Case	**Wave force**		
1.OP	1^{st} order	2^{nd} order wave drift	2^{nd} order QTF
Surge [kN]	10766	283.2	438.0
Heave [kN]	5718	145.4	348.4
Pitch [kNm]	147098	1675	4416
1.NC	1^{st} order	2^{nd} order wave drift	2^{nd} order QTF
Surge [kN]	31910	1327	3516
Heave [kN]	22651	1133	1800
Pitch [kNm]	541797	15683	25899
1.EX	1^{st} order	2^{nd} order wave drift	2^{nd} order QTF
Surge [kN]	74869	2554	2595
Heave [kN]	49397	6178	6276
Pitch [kNm]	1231930	422521	430285

8.3.1 Force Spectra

The time series and power spectral densities of the wave loads in surge, heave, and pitch for load case 1.OP, 1.NC and 1.EX are presented in Figure 8.7 - 8.9. According to these results obtained the contribution of second-order wave loads is minimal. Despite the fact that second-order loads are moderate in comparison to first-order loads, they are considered important to state. Large movements of the body were detected at shorter wavelengths, as indicated in the preceding section. This is related to second-order difference-frequency contributions, which cause oscillatory movements at the resonance frequency. However, this was not the case at the pitch natural frequency, as discussed in previous section.

Load Case 1: 1.OP

The PSDs of the wave loads under operational condition are presented in Figure 8.7. The second-order loads are considerably smaller than the first-order loads, thus the second-order forces are multiplied by ten.

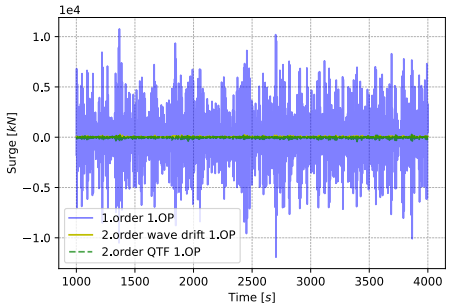

(a) Surge wave loads time series 1.OP

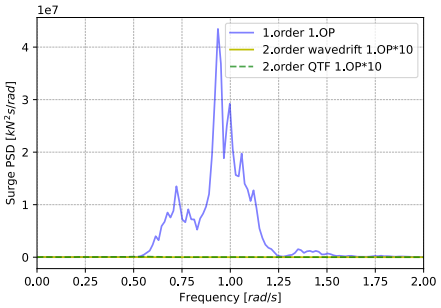

(b) Surge wave loads PSD 1.OP

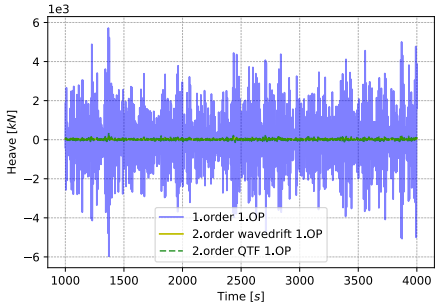

(c) Heave wave loads time series 1.OP

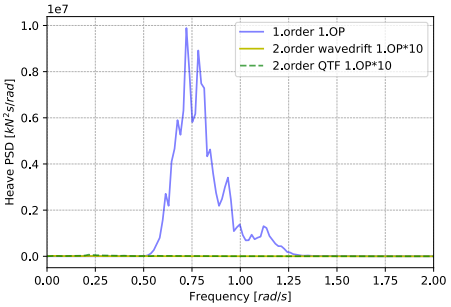

(d) Heave wave loads PSD 1.OP

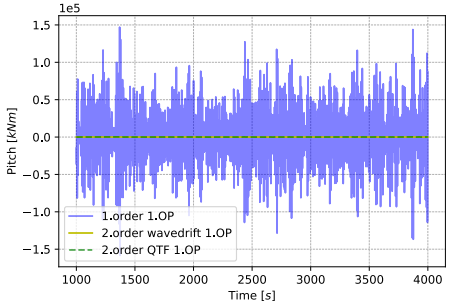

(e) Pitch wave loads time series 1.OP

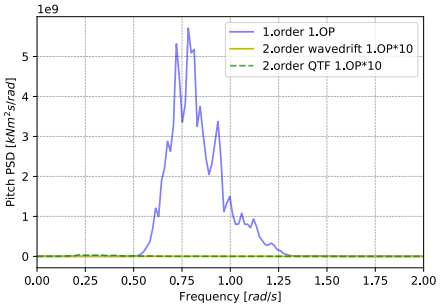

(f) Pitch wave loads PSD 1.OP

Figure 8.7: Wave loads 1.OP

Load Case 2: 1.NC

The PSDs of the wave loads are presented in Figure 8.8. Following the same trend as 1.OP, the second-order loads are significantly smaller than the first-order loads. The peak at the first-order wave load is located at 0.75 rad/s, which corresponds to the peak period 8.38 s (0.75 rad/s).

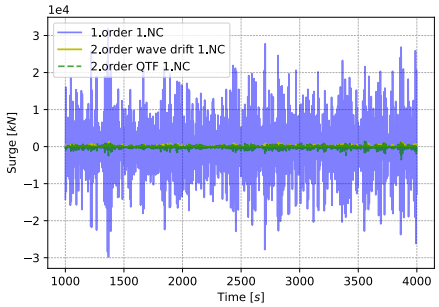

(a) Surge wave loads time series 1.NC

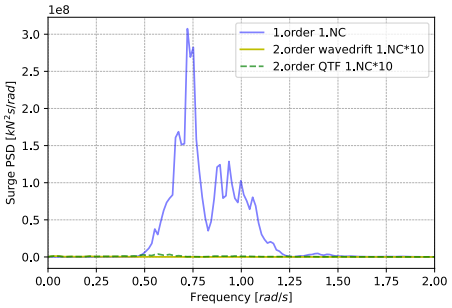

(b) Surge wave loads PSD 1.NC

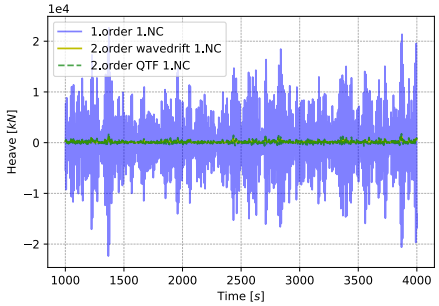

(c) Heave wave loads time series 1.NC

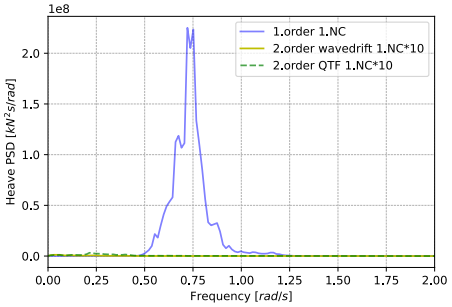

(d) Heave wave loads PSD 1.NC

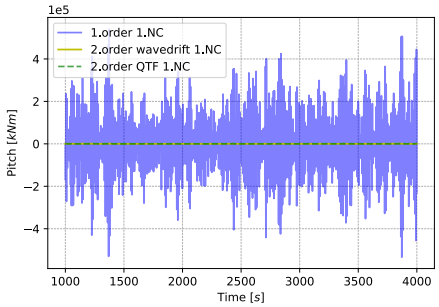

(e) Pitch wave loads time series 1.NC

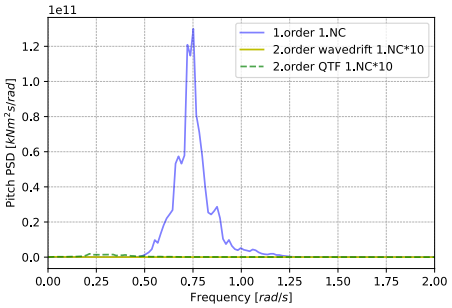

(f) Pitch wave loads PSD 1.NC

Figure 8.8: Wave loads 1.NC

Load Case 3: 1.EX

The PSDs of the wave loads for load case 1.EX is presented in Figure 8.9. The contribution from second-order wave loads is larger for heave and pitch motions. The low-frequency areas are dominated by second-order wave loads in both surge, heave and pitch, which induce substantial motions. The heave spectra display a large single peak at low frequencies for the second-order models, whereas the linear model do not experience this behavior. This outcome of large second-order forces in heave was not seen in 1.OP or 2.OP and are presumed to derive from a numerical error in the coupled time-domain analysis.

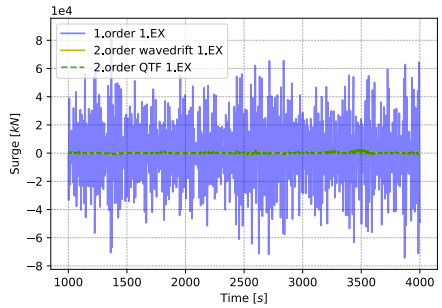

(a) Surge wave loads time series 1.EX

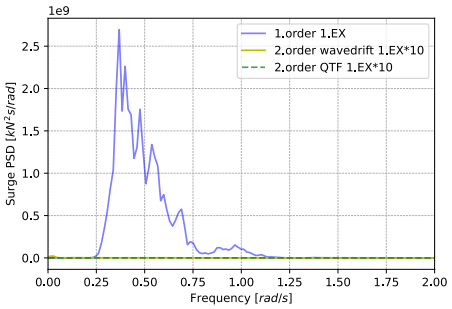

(b) Surge wave loads PSD 1.EX

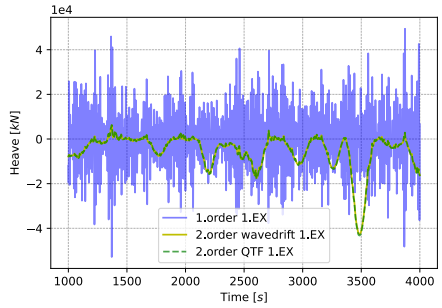

(c) Heave wave loads time series 1.EX

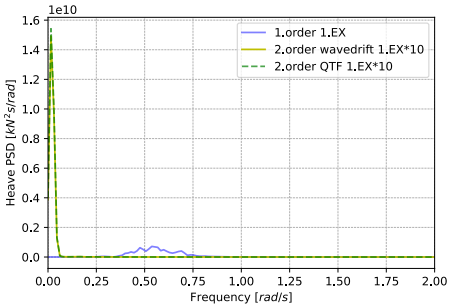

(d) Heave wave loads PSD 1.EX

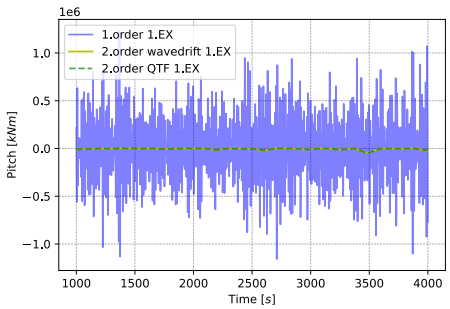

(e) Pitch wave loads time series 1.EX

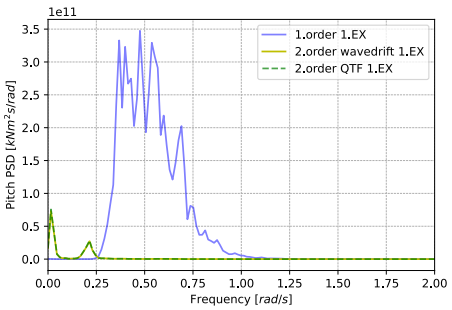

(f) Pitch wave loads PSD 1.EX

Figure 8.9: Wave loads 1.EX

8.4 Mooring Line Tensions

The minimum breaking strength, MBS, was calculated using Equation 6.2. For the studless grade R3 mooring lines, the minimum breaking strength was found to be:

$$MBS_{R3} = 13829\ kN$$

8.4.1 Comparison of Linear (1.M) and Full QTF (3.M) Models

The standard deviations of the mooring line tensions for line 1, 2 and 3 for load case 1.OP, 1.NC and 1. EX for the linear and full QTF models are presented in Table 8.8. The difference between the linear model and the model considering the second-order effects is apparent under extreme conditions. The difference between the linear and Full QTF model is 24 % for line 1, 9.31 % for line 2 and 9.89 % for line 3.

Table 8.8: Standard deviation of mooring line tension for line 1, 2 and 3 Linear and Full QTF models

Load Case	**Model**		
1.OP	Linear 1.M	Full QTF 3.M	Difference [%]
Line 1 [kN]	328	329	0.30
Line 2 [kN]	124.4	124.1	-0.24
Line 3 [kN]	131.9	131.1	-0.61
1.NC	Linear 1.M	Full QTF 3.M	Difference [%]
Line 1 [kN]	1028	1060	3.11
Line 2 [kN]	498.7	506.0	1.46
Line 3 [kN]	622.6	626.4	0.61
1.EX	Linear 1.M	Full QTF 3.M	Difference [%]
Line 1 [kN]	2575	3193	24.0
Line 2 [kN]	170.8	186.7	9.31
Line 3 [kN]	169.8	186.7	9.89

The maximum values of the mooring line tension are underestimated using linear potential theory for load case 1.EX. The difference was 27.67 % for line 1, 11.20 % for line 2 and 11.02 % for line 3 as presented in Table 8.9. In theory, this is due to the linear model not accounting for second-order effects in low-frequency motions, hence the second-order effects were determined to be particularly relevant to consider. However, these effects do not occur in load cases 1.OP and 1.NC. When examining a moored structure, the repercussions of failing to account for second-order effects can be disastrous.

The maximum mooring lines tension for line 1, load case 1.EX exceeds the MBS with 41 % for the linear model and 80 % for the Full QTF model. Indicating, the numerical model requires redesign of the mooring system with an increased stiffness and a higher MBS.

Table 8.9: Maximum values of mooring line tension for line 1, 2 and 3 Linear and Full QTF models

Load Case	**Model**		**Difference [%]**
1.OP	Linear 1.M	Full QTF 3.M	
Line 1 [kN]	4844	4882	0.78
Line 2 [kN]	3298	3303	0.15
Line 3 [kN]	3379	3346	-0.98
1.NC	Linear 1.M	Full QTF 3.M	Difference [%]
Line 1 [kN]	9208	9438	2.50
Line 2 [kN]	5404	5464	1.11
Line 3 [kN]	6350	6235	-1.81
1.EX	Linear 1.M	Full QTF 3.M	Difference [%]
Line 1 [kN]	19529	24932	27.67
Line 2 [kN]	3169	3524	11.20
Line 3 [kN]	3157	3505	11.02

8.4.2 Comparison of Full QTF (3.M) and Newman's approximation (2.M) models

The standard deviation of the mooring line tensions for line 1, 2 and 3 for load case 1.OP, 1.NC and 1.EX for the full QTF and the Newman's approximation model are presented in Table Table 8.10. The obtained results correspond relatively well with the full QTF model, however there is a sight underestimation.

Table 8.10: Standard deviation of mooring line tension for line 1, 2 and 3 Full QTF and Newman's models

Load Case	**Model**		**Difference [%]**
1.OP	Full QTF 3.M	Newman's 2.M	
Line 1 [kN]	329.0	329.7	0.21
Line 2 [kN]	124.1	124.0	-0.08
Line 3 [kN]	131.1	131.5	3.36
1.NC	Full QTF 3.M	Newman's 2.M	Difference [%]
Line 1 [kN]	1060	1056	-0.38
Line 2 [kN]	506.0	499.4	-1.30
Line 3 [kN]	626.4	623.8	-0.42
1.EX	Full QTF 3.M	Newman's 2.M	Difference [%]
Line 1 [kN]	3193	3121	-2.25
Line 2 [kN]	186.7	184.2	-0.80
Line 3 [kN]	186.7	185.2	-0.80

The maximum mooring line tension for line 1 for the Newman's model exceeded the MBS with 78 % as presented in Table 8.11. During the comparison of the model with the QTF, Newman's approximation provided deviation in the maximum values of the surge motions, and the significance of these discrepancies may be determined by investigating the design of mooring line system and the tension in further work.

Table 8.11: Maximum values of mooring line tension for line 1, 2 and 3 Full QTF and Newman's models

Load Case	**Model**		**Difference [%]**
1.OP	Full QTF 3.M	Newman's 2.M	
Line 1 [kN]	4882	4884	0.04
Line 2 [kN]	3303	3300	-0.09
Line 3 [kN]	3346	3361	0.45
1.NC	Full QTF 3.M	Newman's 2.M	Difference [%]
Line 1 [kN]	9438	9729	3.08
Line 2 [kN]	5464	5365	-1.81
Line 3 [kN]	6235	6252	0.27
1.EX	Full QTF 3.M	Newman's 2.M	Difference [%]
Line 1 [kN]	24932	24646	-1.15
Line 2 [kN]	3524	3499	-0.71
Line 3 [kN]	3505	3501	-0.11

8.4.3 Mooring lines tension spectral density

Load case 1: 1.OP

The time series and PSD of the mooring line tension for operational condition, load case 1.OP are presented in Figure 8.10. As observed from the PSD, the mooring line was influenced by both wave and wind loads. The spectra display an agreement between the linear and non-linear models.

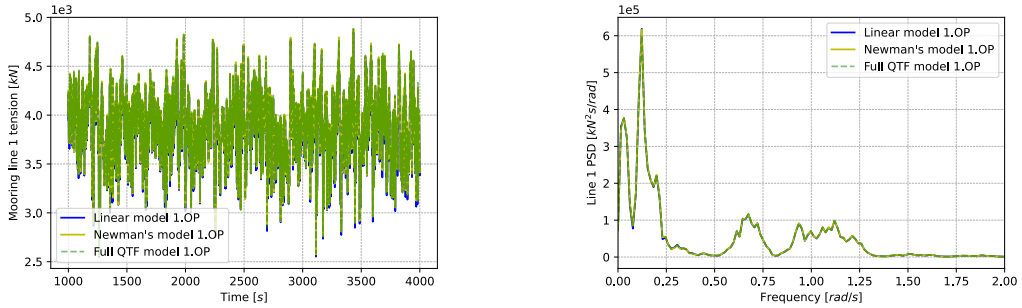

(a) (b)

Figure 8.10: Mooring line 1 load case 1.OP

Load case 2: 1.NC

The time series and PSD of the mooring line tension for near cut-out condition, load case 1.NC are presented in Figure 8.11. The mooring line tension was influenced by both wave and wind loads, which is observed from the PSD. The results obtained from three models corresponds with each other, however the linear model does not take into account the low frequency loads.

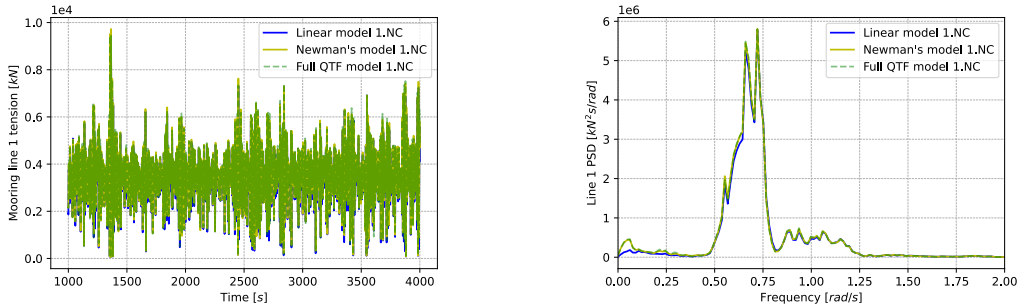

(a) (b)

Figure 8.11: Mooring line 1 load case 1.NC

Load case 3: 1.EX

Investigating the mooring line tension under extreme condition is a critical part of obtaining the highest responses and hydrodynamic loads the mooring system are required to withstand. The Newman's approximation and full QTF models correlated well, while the linear model underestimates the tension as presented in Figure 8.12.

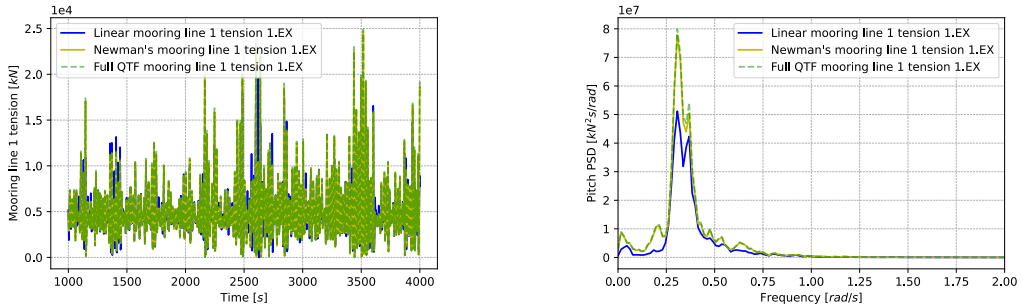

(a) (b)

Figure 8.12: Mooring line 1 load case 1.EX

To investigate the importance of the direction of the incoming waves, wind and current, the model was rotated 180 degrees. Thus, mooring line 2 and 3 experienced the largest mooring line tensions. The mooring lines tensions decreased overall, but in the extreme condition with 100 year return period for U_w, H_s and T_p (1.EX), the maximum mooring line tension for the Full QTF model was 10300 kN in line 2. This value is 26 % less than the MBS.

A solution to increase the MBS would be to change the design of the mooring system, hence increasing the stiffness. The suggested improvements would be an increase of 170 % in chain diameter to 367 mm from 137 mm, increasing the MBS to 43972 kN. The maximum mooring line tension for load case 1.EX then becomes 56 % of the new MBS.

9 Layout Design

The results from the numerical models built a premise for further investigation of the wind farm. Every wind turbine was simulated individually and assumed hydrodynamically and aerodynamically independent. In this chapter, the FWTs was still considered hydrodynamically independent, however aerodynamical wake effects was introduced. A literature review was conducted in chapter 2 on wake effects and wind farm patterns which influences the behavior of wind turbines.

For a wind farm of this size, three different layout concepts are proposed and theoretically compared. Each concept consists of a proposed spacing distance in the prevailing wind direction and the crosswind direction. The spacing distance and wind farm pattern was based on a literature study of two floating offshore wind farms WindFloat Atlantic (2018), which is operational and Hywind Tampen (2019) being installed. The small hypothetical wind farm consists of four 10 MW DTU reference wind turbines, installed on the OO Star Wind Floater and will be produce power to the O&G installation 5 km away. The wind farm has a total rated power of 40 MW. Due to the site location of this wind farm, recently installed power cables by Statnett per the electrification of O&G platforms could be of use.

9.1 Layout Concept 1: Rectangular Pattern

The first concept provides a layout proposal of a rectangular shaped pattern. The spacing distance in the prevailing and crosswind direction was decided to 8D and 4D. The wind farm consists of two rows, with two FWTs in each row. Table 9.1 provides information about relevant properties for the layout concept.

Table 9.1: Layout concept 1 properties

Concept 1	
Number of turbines	4
Turbine spacing distance prevailing [m]	1426
Turbine spacing distance crosswind [m]	713.2
Possibilities of sharing anchor points	Yes

The turbine spacing distance of 713.2 m introduces an opportunity to share anchor points. The horizontal distance from the farileads to the anchors are 689 m, which is equal to 3.9D. An overview of spacing distance and layout pattern is provided in Figure 9.1, while Figure 9.2 presents the layout with mooring lines from a top view perspective. The FOWTs are connected in a loop of 66kV dynamic inter-array cable system with an static export cable to O&G installations via a collecting substation.

The crosswind turbine distance was estimated to be sufficient that wake interactions do not emerge in the row. The FWTs were considered hydrodynamically independent of each other. Thus, for the study in operational and extreme conditions the FWTs were considered isolated. The possibility of FWTs sharing anchor points is an opportunity to reduce installation costs and footprint on the seabed.

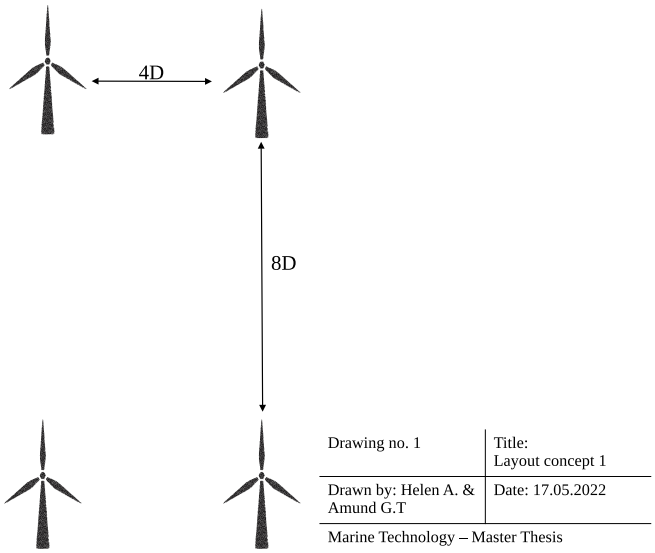

Figure 9.1: Turbine spacing distance for layout concept with rectangular pattern.

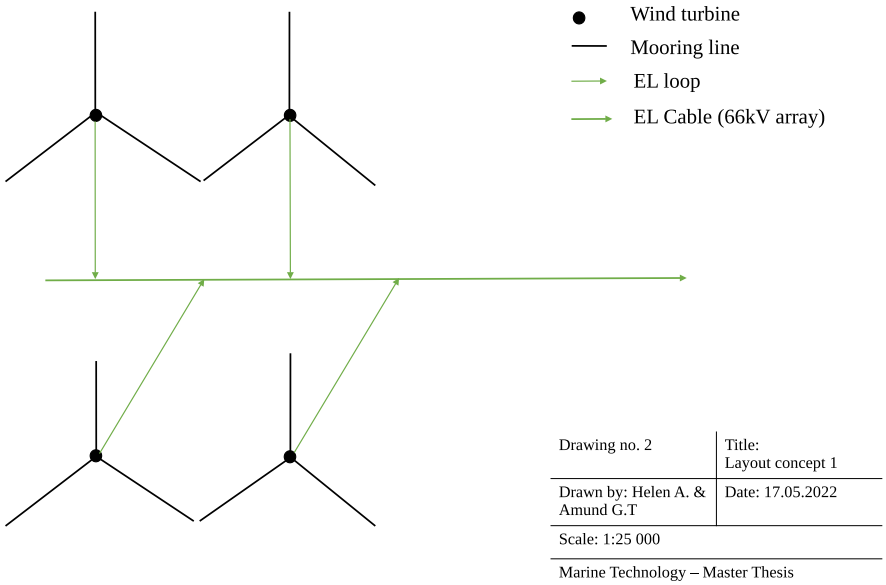

Figure 9.2: Layout concept 1 with mooring and dynamic inter-array cabling system from top view.

9.2 Layout Concept 2: Scattered Pattern

The second concept presents a layout proposal of a parallelogram shaped pattern. The spacing distance in the prevailing and crosswind direction are 8D and 6D. The wind farm consists of two rows, with two FWTs in each row and Table 9.2 provides information about relevant properties for the layout concept. The design of the floating offshore wind farm was based on the design of Hywind Tampen (2019).

Table 9.2: Layout concept 2 properties

Concept 2	
Number of turbines	4
Turbine spacing distance prevailing [m]	1426
Turbine spacing distance crosswind [m]	1070
Possibilities of sharing anchor points	No

The layout concept is illustrated with an overview of the spacing distance and pattern in Figure 9.3, while Figure 9.4 presents the layout with mooring lines from a top view with a dynamic inter-array cabling system. Due to the significant distance between each FWT within the same row, this suggested concept does not have the benefit of sharing anchoring points. The material cost of the inter-array cable system's connecting loop is predicted to be greater due to the significant distance between each turbine. However, the crosswind turbine spacing is adequate to prevent wake interactions from emerging in the row.

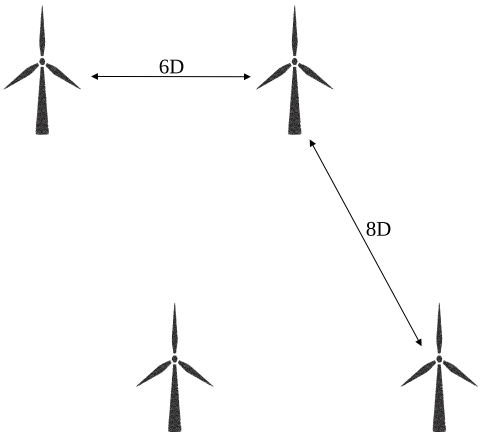

Drawing no. 3	Title: Layout concept 2
Drawn by: Helen A. & Amund G.T	Date: 17.05.2022

Marine Technology – Master Thesis

Figure 9.3: Turbine spacing distance for layout concept with scattered pattern.

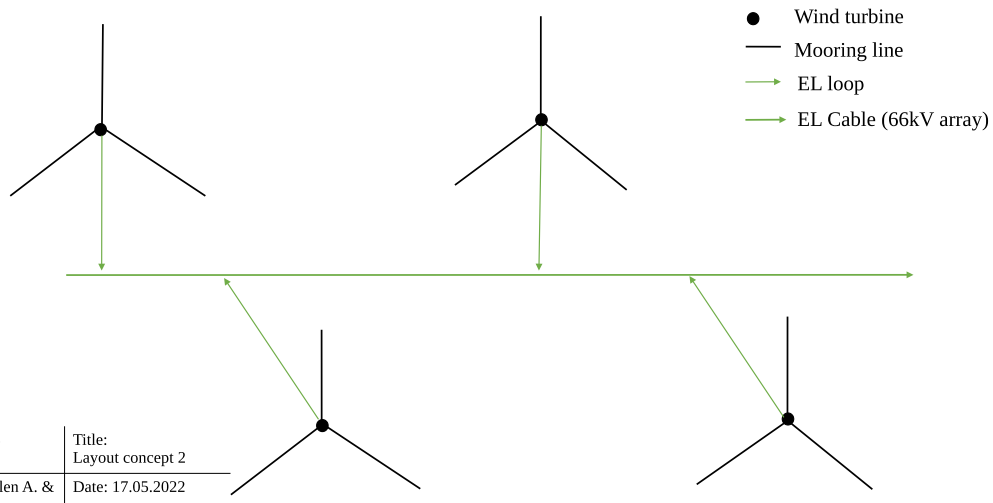

Drawing no. 4	Title: Layout concept 2
Drawn by: Helen A. & Amund G.T	Date: 17.05.2022
Scale: 1:25 000	

Marine Technology – Master Thesis

Figure 9.4: Layout concept 2 with mooring and dynamic inter-array cabling system from top view.

9.3 Layout Concept 3: Single Row

The third concept proposal presents the FWTs in a single row with a crosswind spacing distance of 4D. The design of the wind farm was based on the design of WindFloat Atlantic (2018). Table 9.2 provides information about relevant properties for the layout concept.

Table 9.3: Layout concept 3 properties

Concept 3	
Number of turbines	4
Turbine spacing distance crosswind [m]	713.2
Possibilities of sharing anchor points	Yes

The turbine spacing distance of 713.2 m introduces the same opportunity of sharing anchor points as for the first layout concept. Thereby, contributing to the reduction of installation cost and footprint on the seabed. Additionally, this layout concept would have a reduced environmental impact compared to the two other proposed concepts by being distributed over smaller area with adequate crosswind turbine distance to prevent wake interactions from emerging. An overview of the spacing distance and pattern is illustrated in Figure 9.5 and Figure 9.6 presents the layout with mooring lines from a top view. The distribution of the turbines in this concept will contribute to the reduction of material and operational cost, due to the proximity of the wind turbines.

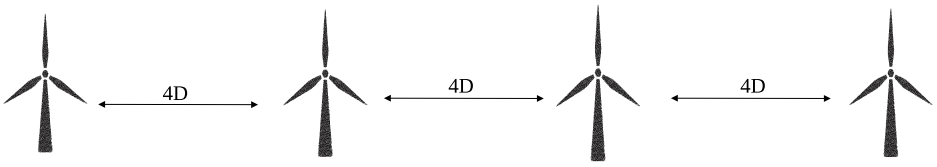

Drawing no. 5	Title: Layout concept 3
Drawn by: Helen A. & Amund G.T	Date: 17.05.2022

Marine Technology – Master Thesis

Figure 9.5: Turbine spacing distance for layout concept with single row pattern.

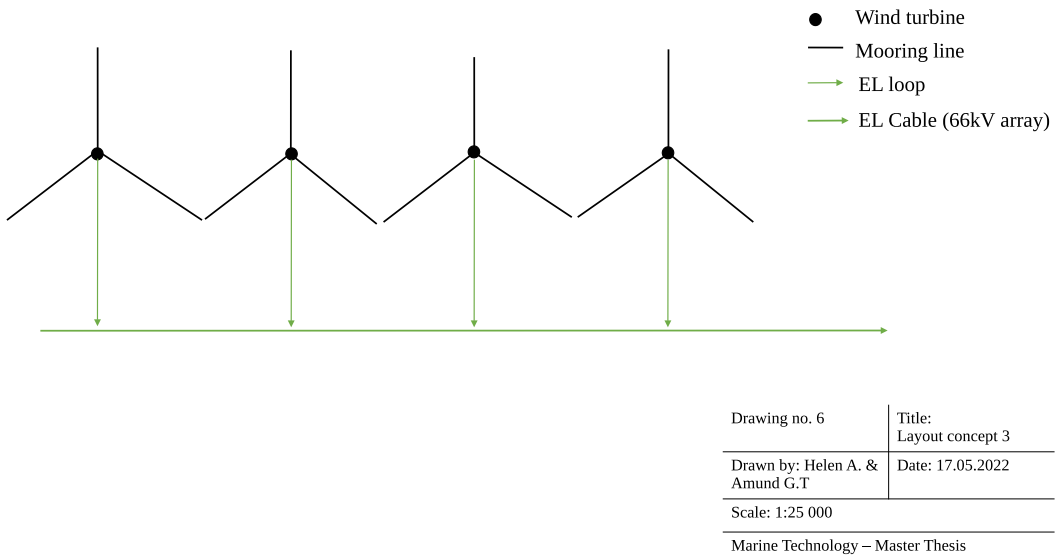

Figure 9.6: Layout concept 3 with mooring and dynamic inter-array cabling system from top view.

9.4 Power Transmission and Storage

A small wind farm of this size located 5 km away from the intended power recipient, an offshore O&G installation does not necessarily require a collecting substation within the wind farm. The possibility of placing the collecting substation on the O&G platform is foreseeable. However, according to the literature study conducted in Section 2.5 placing the substation within the wind farm increases export cables efficiency. Consequently, the substation was determined to be located within the wind farm for simplicity and efficiency. A simplified illustration of the wind farm consisting of four wind turbines connected to an O&G installation is presented in Figure 9.7.

In connection with the Deep purple pilot project reviewed in Chapter 2.5.3, a method of transforming energy for later use can limit constraints regarding power fluctuation. Hence, hydrogen production through electrolysis and storage can be integrated into the energy transmission system. However, a reverse osmosis facility will be required to filter saltwater for electrolysis and the compressed hydrogen can initially be stored on the seafloor. Alternatively, to the considerable expenses of developing an electrolysis and hydrogen storage facility, the excess energy can be exported to a neighbouring installation via an excising infrastructure on the North Sea.

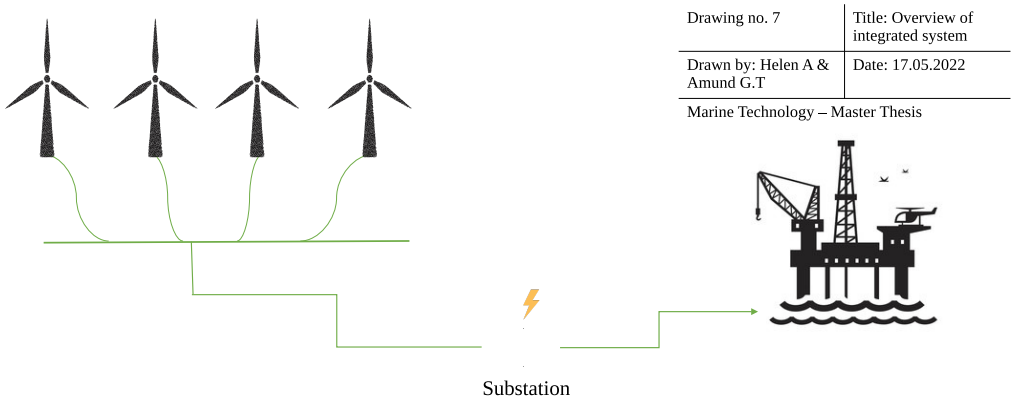

Figure 9.7: Simplified illustration of energy transmission from wind farm to a O&G platform.

10 Conclusion and Recommendations for Further Work

10.1 Conclusion

The feasibility study of an offshore wind farm consisting of four floating wind turbines operating at a water depth of 130 m has been perfomed. The OO Star Wind Floater consisting of a semi-submersible substructure supporting the 10 MW DTU reference wind turbine was analysed. The FWT was investigated under the assumption of hydrodynamically independent from each other. A numerical model was developed through panel method, thereafter hydrodynamic properties of the structure were obtained by performing first-order and second-order frequency domain analysis. A verification of the numerical model was carried out, along with a comparison of results obtained from first-order frequency domain analysis against the results from the LIFES50+ project in Section 7.1.

The obtained properties from frequency domain analysis were then imported into SIMA, where time-domain simulations were conducted. The main objective was to investigate the behavioural characteristics of the FWT and evaluate the feasibility of a small wind farm supplying power to an O&G installation. The applicability, survivability and operativity of the numerical model was evaluated by hydrodynamic load models under operational and extreme conditions. The following compiled list presents the conclusions drawn based on the feasibility study.

- When the wind turbine is operational, linear potential theory underestimated the behaviour of the low-frequency responses. For load cases 2.OP and 2.NC , the difference in standard deviation and maximum value between the linear and the difference-frequency full QTF models in surge motions was, on average, 56 % and 20.1 %, respectively. However, this is not the case for the extreme load cases. In accordance with Duarte et al. 2014 the difference-frequency effects become insignificant in these conditions.
- The full QTF model in surge motion displayed a good agreement with the Newman's approximation. Additionally, the significant mooring line tensions were captured by Newman's approximation. Thus, Newman's approximation can be applicable to determine surge motion and mooring line tension. Nonetheless, the full QTF should be applied during the analysis of second-order effects.

- The mooring line's minimum breaking strength, MBS, was exceeded with 41 % for the linear model and 80 % for the Full QTF model for the extreme environmental load condition 1.EX with wind. Therefore, it is proposed that the FWT needs a new mooring system design. Solutions to this problem could be to upgrade the chain grade, or increase the chain diameter by 170 % to 367 mm, from 137 mm so that the MBS is not exceeded.
- The maximum values of the mooring line tension are underestimated using linear potential theory compared to the full QTF model for load case 1.EX. The difference was 27.67 % for line 1, which experienced the largest tensions. In theory, this is due to the linear model not accounting for second-order effects in low-frequency motions, hence the second-order effects were determined to be particularly relevant to consider. However, these effects did not occur in load cases 1.OP and 1.NC.
- The primary layout for the wind farm was determined to be layout Concept 3: A single row with 4D distance spacing between each turbine. The decision was based on the literature review conducted on requirements for prevention of wake interactions, environmental impact, and preliminary cost discussion of materials.
- The coupled model of the OO Star Wind Floater created in this thesis was deemed not feasible to be employed in a small wind farm in the North Sea. The MBS was exceeded and the model did not behave as expected in pitch. The model showed no excitation around the natural frequency in pitch. A new model with an updated panel model and a modified control system should be further investigated.

10.2 Recommendations for Further Work

- It is advised to conduct a more detailed study of the optimized wind farm layout design. The study can include several wake models and numerical software for optimizing the layout. The site specific capacity factor of the wind farm, annual energy production and wake losses can be calculated. The numerical software TOPFARM can be used for this task. By modifying the position of turbines, the analysis in a software such as TOPFARM, aims to maximize yearly energy output, reduce finance expenses and reduce electrical grid costs.
- Existing infrastructure must be mapped and a Levelized Cost of Electricity analysis can determine if the project is economically justifiable.
- A detailed coupled model with electrical cables, oriented in different directions would be advantageous when performing simulations of more realistic conditions.
- A stability analysis of the new electrical grid after integrating 35 MW wind power by dynamic simulation with several disturbances could be advantageous. These disturbances would be instances of generator start, loss of multiple wind turbines, wind speed gusts and loss of previous power source i.e., gas turbines.
- The behavior of a subsea power cable installed on the platform should be analysed to investigate the optimal hang-off position. In addition, the a sensitivity study of the dimensions of the cables should be performed.

- The effect of the floating substructure's heave plates could be analysed, both in terms of the effect of thickness selection and the viscous forces on the heave plates. The main simulations in this thesis do not include a correction for the added mass contribution due to the heave plates in the potential theory. Consequently, this correction should be investigated.

Bibliography

Ammara, Idriss, Christophe Leclerc, and Christian Masson (2002). "A viscous three-dimensional differential/actuator-disk method for the aerodynamic analysis of wind farms". In: *J. Sol. Energy Eng.* 124.4, pp. 345–356.

Andersen, H et al. (2021). "D1.2 Concept Description Report". In.

Atcheson, Mairead et al. (2016). *Floating Offshore Wind Energy*. Springer.

Azcona, J et al. (2013). "State-of-the-art and implementation of design tools for floating structures". In: *INNWIND D4* 21.

Bachynski, Erin E and Lene Eliassen (2019). "The effects of coherent structures on the global response of floating offshore wind turbines". In: *Wind Energy* 22.2, pp. 219–238.

Bachynski-Polić, Erin (2021). *Lecture notes - Basic aerodynamics for wind turbines*.

Bak, Christian et al. (2013). "The DTU 10-MW reference wind turbine". In: *Danish wind power research 2013*.

Bayati, I et al. (2016). "Wind tunnel validation of AeroDyn within LIFES50+ project: imposed Surge and Pitch tests". In: *Journal of Physics: Conference Series*. Vol. 753. 9. IOP Publishing, p. 092001.

Borg, M and H Bredmose (2015). "Overview of the numerical models used in the consortium and their qualification". In: *LIFES50+ Deliverable* 4.4.

Borg, Michael and Maurizio Collu (2015). "Offshore floating vertical axis wind turbines, dynamics modelling state of the art. Part III: Hydrodynamics and coupled modelling approaches". In: *Renewable and sustainable energy reviews* 46, pp. 296–310.

Borisade, Friedemann et al. (2018). "Validation of INNWIND. EU scaled model tests of a semisubmersible floating wind turbine". In: *International Journal of Offshore and Polar Engineering* 28.01, pp. 54–64.

Chamorro, Leonardo P, REA Arndt, and Fotis Sotiropoulos (2011). "Turbulent flow properties around a staggered wind farm". In: *Boundary-layer meteorology* 141.3, pp. 349–367.

Chuang, Zhenju, Shewen Liu, and Yu Lu (2020). "Influence of second order wave excitation loads on coupled response of an offshore floating wind turbine". In: *International Journal of Naval Architecture and Ocean Engineering* 12, pp. 367–375.

Clauss, Gunther F, Christian Schmittner, and Katja Stutz (2002). *Time-domain investigation of a semisubmersible in rogue waves*. Vol. 36126, pp. 509–516.

Coelingh, JP, AJM Van Wijk, and AAM Holtslag (1996). "Analysis of wind speed observations over the North Sea". In: *Journal of Wind Engineering and Industrial Aerodynamics* 61.1, pp. 51–69.

Coppez, Gabrielle, Sunetra Chowdhury, and SP Chowdhury (2010). "The importance of energy storage in renewable power generation: a review". In: *45th International Universities Power Engineering Conference UPEC2010*. IEEE, pp. 1–5.

Council, Global Wind Energy (2021). "GWEC— global wind report 2021". In: *Global Wind Energy Council: Brussels, Belgium*.

De Hauwere, Nathalie by Flanders Marine Institute (2016). *Marine Regions Towards a standard for georeferenced marine names*. URL: http://www.marineregions.org (visited on May 16, 2022).

Directorate, Norwegian Petroleum (2022). *Factmap*. URL: https://factmaps.npd.no/factmaps (visited on May 16, 2022).

DNV (2010). "Recommended Practice: environmental conditions and environmental loads". In: *DNV: Oslo, Norway*.

– (2015). *DNV-OS-E302: Offshore mooring chain*.

– (2022). *Floating Substations: the next challenge on the path to commercial scale floating windfarms*. URL: https://www.dnv.com/article/floating-substations-the-next-challenge-on-the-path-to-commercial-scale-floating-windfarms-199213 (visited on May 20, 2022).

DNV, GL (2019). "SESAM User Manual, WADAM, Wave Analysis by Diffraction and Morison theory". In: *Høvik, Norway*.

Subsea power cables for wind power plants (June 2016). Standard. DNV.

Duarte, Tiago M, António J Sarmento, and Jason M Jonkman (2014). "Effects of second-order hydrodynamic forces on floating offshore wind turbines". In.

ENERGY EFFICIENCY & RENEWABLE ENERGY, Office of (2022). *Hydrogen Production: Electrolysis Hydrogen and Fuel Cell Technologies Office*. URL: https://www.energy.gov/eere/fuelcells/hydrogen-production-electrolysis (visited on Apr. 25, 2022).

Equinor (2016). "Snorre Field Metocean Design Basis". In.

– (2019a). *Hywind Scotland Facts about Hywind Scotland*. URL: https://www.equinor.com/en/what-we-do/uk-wind.html (visited on Feb. 28, 2020).

– (2019b). *Hywind Tampen the world's first renewable power for offshore oil and gas*. URL: https://www.equinor.com/en/what-we-do/hywind-tampen.html (visited on Mar. 15, 2022).

European Commission (2020). "Boosting Offshore Renewable Energy for a Climate Neutral Europe". In: IP/20/2096. URL: https://ec.europa.eu/commission/presscorner/detail/en/IP_20_2096.

Faltinsen, Odd (1993). *Sea loads on ships and offshore structures*. Vol. 1. Cambridge university press.

Finne, Styrk, John Grue, and Arne Nestegård (2000). "Prediction of the complete second order wave drift damping force for offshore structures". In: *The Tenth International Offshore and Polar Engineering Conference*. OnePetro.

Gao, Xiaoxia, Hongxing Yang, and Lin Lu (2014). "Investigation into the optimal wind turbine layout patterns for a Hong Kong offshore wind farm". In: *Energy* 73, pp. 430–442.

Grady, SA, MY Hussaini, and Makola M Abdullah (2005). "Placement of wind turbines using genetic algorithms". In: *Renewable energy* 30.2, pp. 259–270.

Greco, Marielna (2021). *Lecture notes in Sea Loads*.

Hansen, Martin (2015). *Aerodynamics of wind turbines*. Routledge.

Hansen, Morten Hartvig and Lars Christian Henriksen (2013). "Basic DTU wind energy controller". In.

Herbert-Acero, José F et al. (2014). "A review of methodological approaches for the design and optimization of wind farms". In: *Energies* 7.11, pp. 6930–7016.

Hou, Peng et al. (2015). "Optimized placement of wind turbines in large-scale offshore wind farm using particle swarm optimization algorithm". In: *IEEE Transactions on Sustainable Energy* 6.4, pp. 1272–1282.

BW-Ideol (2021). *EOLMED PROJECT A PRE-COMMERCIAL PROJECT OF 3 UNITS*. URL: `https://www.bw-ideol.com/en/eolmed-project` (visited on Mar. 30, 2022).

IEC (2019). "Wind energy generation systems - Part 3-1: Design requirements for fixed offshore wind turbines". In.

INNWIND.EU project, A consortium comprises of leading Industrial Partners and Research Establishments (2017). URL: `http://www.innwind.eu/work-packages` (visited on Feb. 15, 2022).

Johannessen, Kenneth, Trond Stokka Meling, and Sverre Hayer (2001). "Joint distribution for wind and waves in the northern north sea". In: *The eleventh international offshore and polar engineering conference*. OnePetro.

Johansen, Katinka (2021). "Blowing in the wind: A brief history of wind energy and wind power technologies in Denmark". In: *Energy Policy* 152, p. 112139.

Jonkman, Bonnie J (2009). *TurbSim user's guide: Version 1.50*. Tech. rep. National Renewable Energy Lab.(NREL), Golden, CO (United States).

Jonkman, J. (2007). *Loads analysis of a floating offshore wind turbine using fully coupled simulation*. Tech. rep. National Renewable Energy Lab.(NREL), Golden, CO (United States).

Jonkman, Jason and Walter Musial (2010). *Offshore code comparison collaboration (OC3) for IEA Wind Task 23 offshore wind technology and deployment*. Tech. rep. National Renewable Energy Lab.(NREL), Golden, CO (United States).

KonKraft (2020-1). *The energy industry of tomorrow on the Norwegian continental shelf, climate strategy towards 2030 and 2050.* KonKraft.

Kusiak, Andrew and Zhe Song (2010). "Design of wind farm layout for maximum wind energy capture". In: *Renewable energy* 35.3, pp. 685–694.

Kvittem, Marit Irene (2014). "Modelling and response analysis for fatigue design of a semi-submersible wind turbine". In.

Ladenburg, Jacob and Alex Dubgaard (2009). "Preferences of coastal zone user groups regarding the siting of offshore wind farms". In: *Ocean & Coastal Management* 52.5, pp. 233–242.

Larsen, Gunner Chr and Pierre-Elouan Réthoré (2013). "TOPFARM–a tool for wind farm optimization". In: *Energy Procedia* 35, pp. 317–324.

Larsen, Torben J and Tor D Hanson (2007). "A method to avoid negative damped low frequent tower vibrations for a floating, pitch controlled wind turbine". In: *Journal of Physics: Conference Series*. Vol. 75. 1. IOP Publishing, p. 012073.

Li, Lin, Zhen Gao, and Torgeir Moan (2015). "Joint distribution of environmental condition at five european offshore sites for design of combined wind and wave energy devices". In: *Journal of Offshore Mechanics and Arctic Engineering* 137.3.

Linton, CM and DV Evans (1990). "The interaction of waves with arrays of vertical circular cylinders". In: *Journal of fluid mechanics* 215, pp. 549–569.

Lopez-Pavon, Carlos and Antonio Souto-Iglesias (2015). "Hydrodynamic coefficients and pressure loads on heave plates for semi-submersible floating offshore wind turbines: A comparative analysis using large scale models". In: *Renewable Energy* 81, pp. 864–881.

Marmidis, Grigorios, Stavros Lazarou, and Eleftheria Pyrgioti (2008). "Optimal placement of wind turbines in a wind park using Monte Carlo simulation". In: *Renewable energy* 33.7, pp. 1455–1460.

McIver, P (2002). "Wave interaction with arrays of structures". In: *Applied Ocean Research* 24.3, pp. 121–126.

McIver, P and DV Evans (1984). "Approximation of wave forces on cylinder arrays". In: *Applied ocean research* 6.2, pp. 101–107.

Meier, Konrad (2014). "Hydrogen production with sea water electrolysis using Norwegian offshore wind energy potentials". In: *International Journal of Energy and Environmental Engineering* 5.2, pp. 1–12.

Mello, Pedro C et al. (2021). "Influence of heave plates on the dynamics of a floating offshore wind turbine in waves". In: *Journal of Marine Science and Technology* 26.1, pp. 190–200.

Ministry of Petroleum and Energy (June 12, 2020). *Opening of the areas Utsira Nord and Sørlige Nordsjø II for processing of applications for licences for renewable energy production pursuant to the Offshore Energy Act*. 1 Meld. St.36. The Norwegian Government. URL: https://www.regjeringen.no/no/dokumenter/meld.-st.-36-20202021/id2860081.

Mosetti, GPCDB, Carlo Poloni, and Bruno Diviacco (1994). "Optimization of wind turbine positioning in large windfarms by means of a genetic algorithm". In: *Journal of Wind Engineering and Industrial Aerodynamics* 51.1, pp. 105–116.

Mota, Daniel (2021). *Wind energy for offshore installations: opportunities and challenges How connecting offshore wind to oil and gas rigs can help reduce their greenhouse gas emissions*. URL: https://blog.sintef.com/sintefenergy/wind-energy-for-offshore-installations-opportunities-and-challenges/ (visited on Mar. 22, 2022).

Newman, John Nicholas (2018). *Marine hydrodynamics*. The MIT press.

Norsk-Industri (2021). *LEVERANSEMODELLER FOR HAVVIND*. Norsk Industri. URL: https://www.norskindustri.no/siteassets/dokumenter/rapporter-og-brosjyrer/leveransemodeller-havvind/leveransemodeller-havvind_hovedrapport.pdf.

Ormberg, Harald and Erin E Bachynski (2012). "Global analysis of floating wind turbines: Code development, model sensitivity and benchmark study". In: *The Twenty-second International Offshore and Polar Engineering Conference*. OnePetro.

Pegalajar-Jurado, A et al. (2018). "LIFES50+ D4. 5: State-of-the-art models for the two LIFES50+ 10 MW floater concepts". In: *Technical University of Denmark, Technical Report*.

Pookpunt, Sittichoke and Weerakorn Ongsakul (2013). "Optimal placement of wind turbines within wind farm using binary particle swarm optimization with time-varying acceleration coefficients". In: *Renewable energy* 55, pp. 266–276.

Principle-Power (2019). *WindFloat Atlantic New giants at sea*. URL: https://www.principlepower.com/projects/windfloat-atlantic (visited on Mar. 27, 2022).

Rentschler, Manuel UT et al. (2020). "Parametric study of dynamic inter-array cable systems for floating offshore wind turbines". In: *Marine Systems & Ocean Technology* 15.1, pp. 16–25.

Resner, Leszek and Sandra Paszkiewicz (2021). "Radial Water Barrier in Submarine Cables, Current Solutions and Innovative Development Directions". In: *Energies* 14.10, p. 2761.

Robertson, Amu N et al. (2020). "OC6 Phase I: Investigating the underprediction of low-frequency hydrodynamic loads and responses of a floating wind turbine". In: *Journal of Physics: Conference Series*. Vol. 1618. 3. IOP Publishing, p. 032033.

Robertson, Amy et al. (2014). "Offshore code comparison collaboration continuation within IEA wind task 30: Phase II results regarding a floating semisubmersible wind system". In: *International Conference on Offshore Mechanics and Arctic Engineering*. Vol. 45547. American Society of Mechanical Engineers, V09BT09A012.

Robertson, Amy N et al. (2017). "OC5 project phase II: validation of global loads of the DeepCwind floating semisubmersible wind turbine". In: *Energy Procedia* 137, pp. 38–57.

Rodrigues, S et al. (2015). "Trends of offshore wind projects". In: *Renewable and Sustainable Energy Reviews* 49, pp. 1114–1135.

Sanderse, Benjamin, SP Van der Pijl, and Barry Koren (2011). "Review of computational fluid dynamics for wind turbine wake aerodynamics". In: *Wind energy* 14.7, pp. 799–819.

Scotland, Marine (2018). *Review of Approaches and Costs of Decommissioning OffshoreWind Installations Public report.*

Shahan, Zachary et al. (2014). "History of wind turbines". In: *Renewable Energy World* 21.

Silva de Souza, Carlos Eduardo, Petter Andreas Berthelsen, et al. (2021). "Definition of the INO WINDMOOR 12 MW base case floating wind turbine". In.

Silva de Souza, Carlos Eduardo, Nuno Fonseca, et al. (2021). "Calibration of a Time-Domain Hydrodynamic Model for A 12 MW Semi-Submersible Floating Wind Turbine". In: *International Conference on Offshore Mechanics and Arctic Engineering*. Vol. 85192. American Society of Mechanical Engineers, V009T09A028.

Simos, Alexandre N et al. (2018). "Slow-drift of a floating wind turbine: An assessment of frequency-domain methods based on model tests". In: *Renewable energy* 116, pp. 133–154.

SINTEF, Ocean (2017). *SIMO 4.10. 3 User Guide.*

Song, Huimin et al. (2012). "Incorporation of multi-member substructure capabilities in FAST for analysis of offshore wind turbines". In: *Offshore Technology Conference*. OnePetro.

Spring, Bradford H and Peter L Monkmeyer (1975). "Interaction of plane waves with vertical cylinders". In: *Coastal Engineering 1974*, pp. 1828–1847.

Tao, Longbin and Shunqing Cai (2004). "Heave motion suppression of a Spar with a heave plate". In: *Ocean engineering* 31.5-6, pp. 669–692.

Tao, Longbin and Krish Thiagarajan (2003). "Low KC flow regimes of oscillating sharp edges. II. Hydrodynamic forces". In: *Applied ocean research* 25.2, pp. 53–62.

TechnipFMC (2021a). *Deep Purple Energy Transition, Deep Purple.* URL: `https://www.technipfmc.com/en/what-we-do/subsea/energy-transition-deep-purple/` (visited on Apr. 22, 2022).

– (2021b). *Deep Purple Pilot.* URL: `https://www.technipfmc.com/en/what-we-do/subsea/energy-transition-deep-purple/deep-purple-pilot/` (visited on Apr. 22, 2022).

Thys, Maxime, Valentin Chabaud, et al. (2018). "Real-time hybrid model testing of a semi-submersible 10MW floating wind turbine and advances in the test method". In: *International Conference on Offshore Mechanics and Arctic Engineering*. Vol. 51975. American Society of Mechanical Engineers, V001T01A013.

Thys, Maxime, Alessandro Fontanella, et al. (2019). "Hybrid model tests for floating offshore wind turbines". In: *International Conference on Offshore Mechanics and Arctic Engineering*. Vol. 59353. American Society of Mechanical Engineers, V001T01A023.

Vermeer, LJ, Jens Nørkær Sørensen, and Antonio Crespo (2003). "Wind turbine wake aerodynamics". In: *Progress in aerospace sciences* 39.6-7, pp. 467–510.

Wang, Lu et al. (2022). "OC6 phase I: Improvements to the OpenFAST predictions of nonlinear, low-frequency responses of a floating offshore wind turbine platform". In: *Renewable Energy*.

Williams, AN and Z Demirbilek (1988). "Hydrodynamic interactions in floating cylinder arrays—I. Wave scattering". In: *Ocean Engineering* 15.6, pp. 549–583.

WindFloat Atlantic (2018).

Worzyk, Thomas (2009). *Submarine power cables: design, installation, repair, environmental aspects*. Springer Science & Business Media.

Yu, W et al. (2018). "LIFES50+ Deliverable D4.2: Public definition of the two LIFES50+ 10 MW floater concepts". In: *University of Stuttgart*.

Yu, Wei, Kolja Müller, and Franck Lemmer (2018). *Qualification of innovative floating substructures for 10MW wind turbines and water depths greater than 50 m: D7.1 Review of FOWT guidelines and design practice*. Tech. rep. Technical report, LIFES50+ project.

Zhang, Lixian et al. (2020). "Second-order hydrodynamic effects on the response of three semisubmersible floating offshore wind turbines". In: *Ocean Engineering* 207, p. 107371.

A Free decay simulations

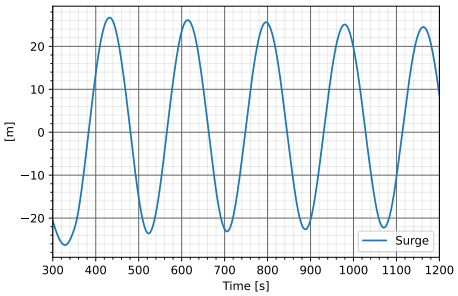

(a) Surge

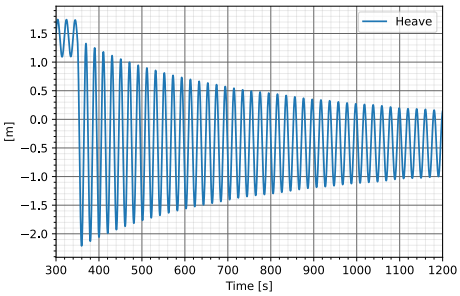

(b) Heave

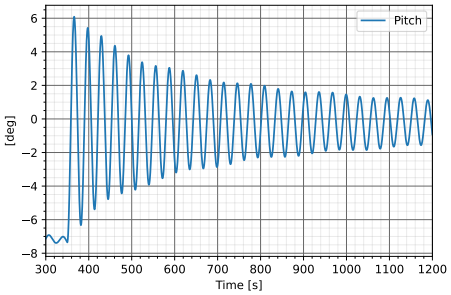

(c) Pitch

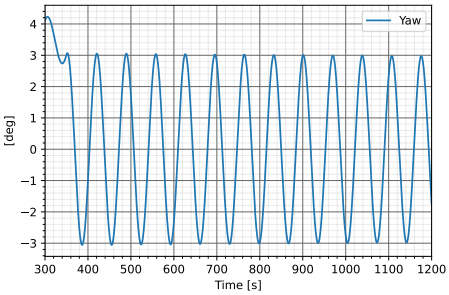

(d) Yaw

Figure A.1: Free decay tests performed in SIMA

B Load cases

B.1 Load case 1.OP response

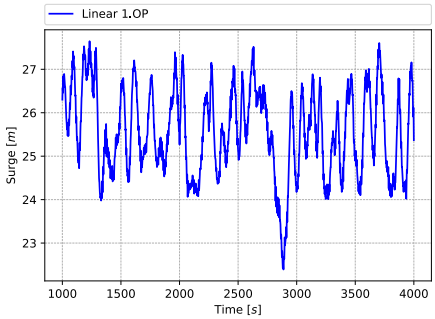

(a) Linear model timeseries surge 1.OP

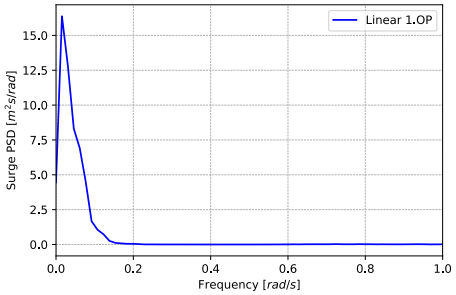

(b) Linear model PSD surge 1.OP

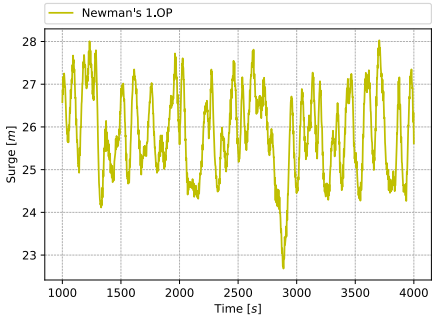

(c) Newman's model timeseries surge 1.OP

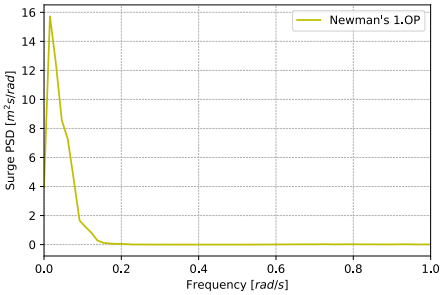

(d) Newman's model PSD surge 1.OP

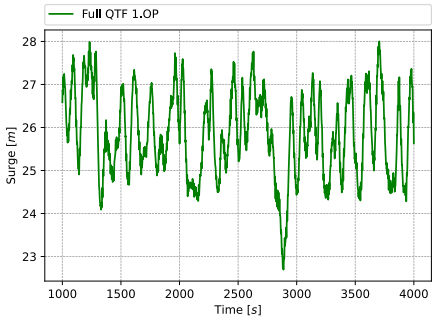

(e) Full QTF model timeseries surge 1.OP

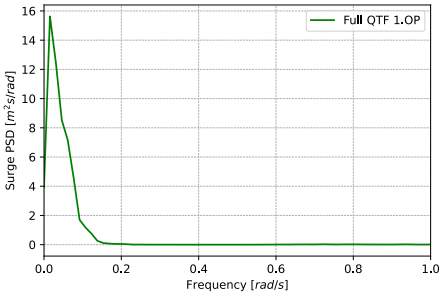

(f) Full QTF model PSD surge 1.OP

Figure B.1: Surge response 1.OP

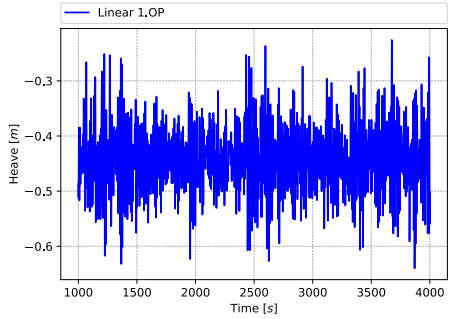

(a) Linear model timeseries heave 1.OP

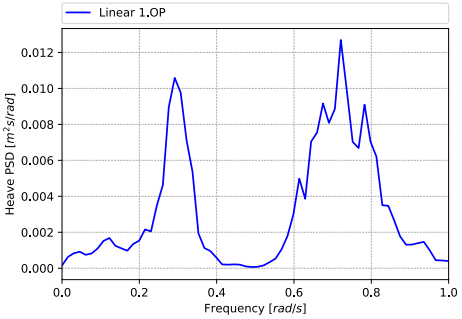

(b) Linear model PSD heave 1.OP

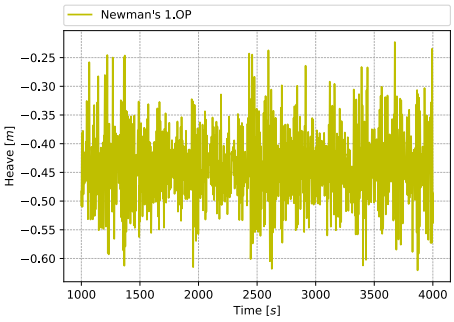

(c) Newman's model timeseries heave 1.OP

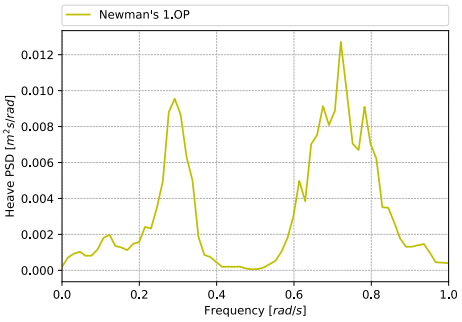

(d) Newman's model PSD heave 1.OP

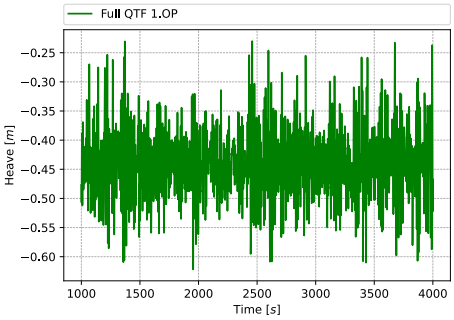

(e) Full QTF model timeseries heave 1.OP

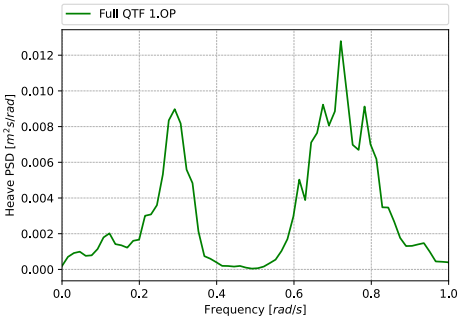

(f) Full QTF model PSD heave 1.OP

Figure B.2: Heave response 1.OP

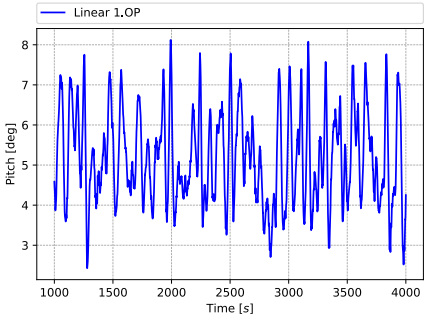

(a) Linear model timeseries pitch 1.OP

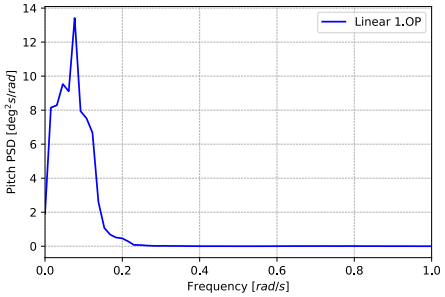

(b) Linear model PSD pitch 1.OP

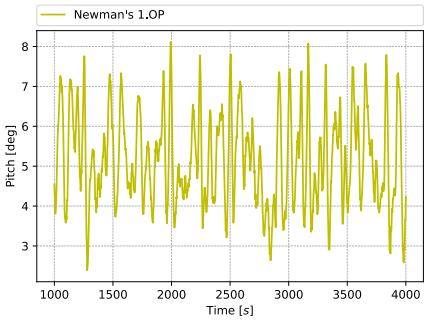

(c) Newman's model timeseries pitch 1.OP

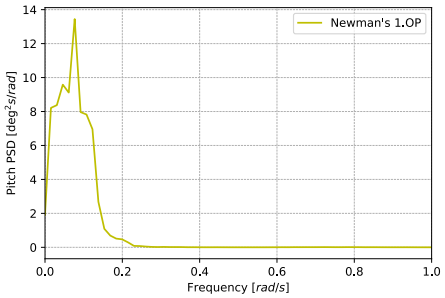

(d) Newman's model PSD pitch 1.OP

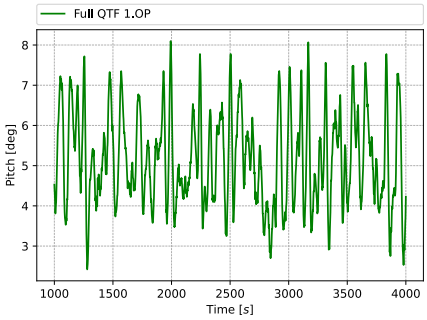

(e) Full QTF model timeseries pitch 1.OP

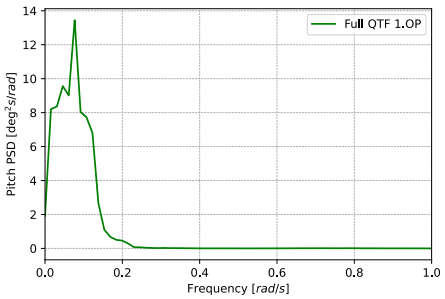

(f) Full QTF model PSD pitch 1.OP

Figure B.3: Pitch response 1.OP

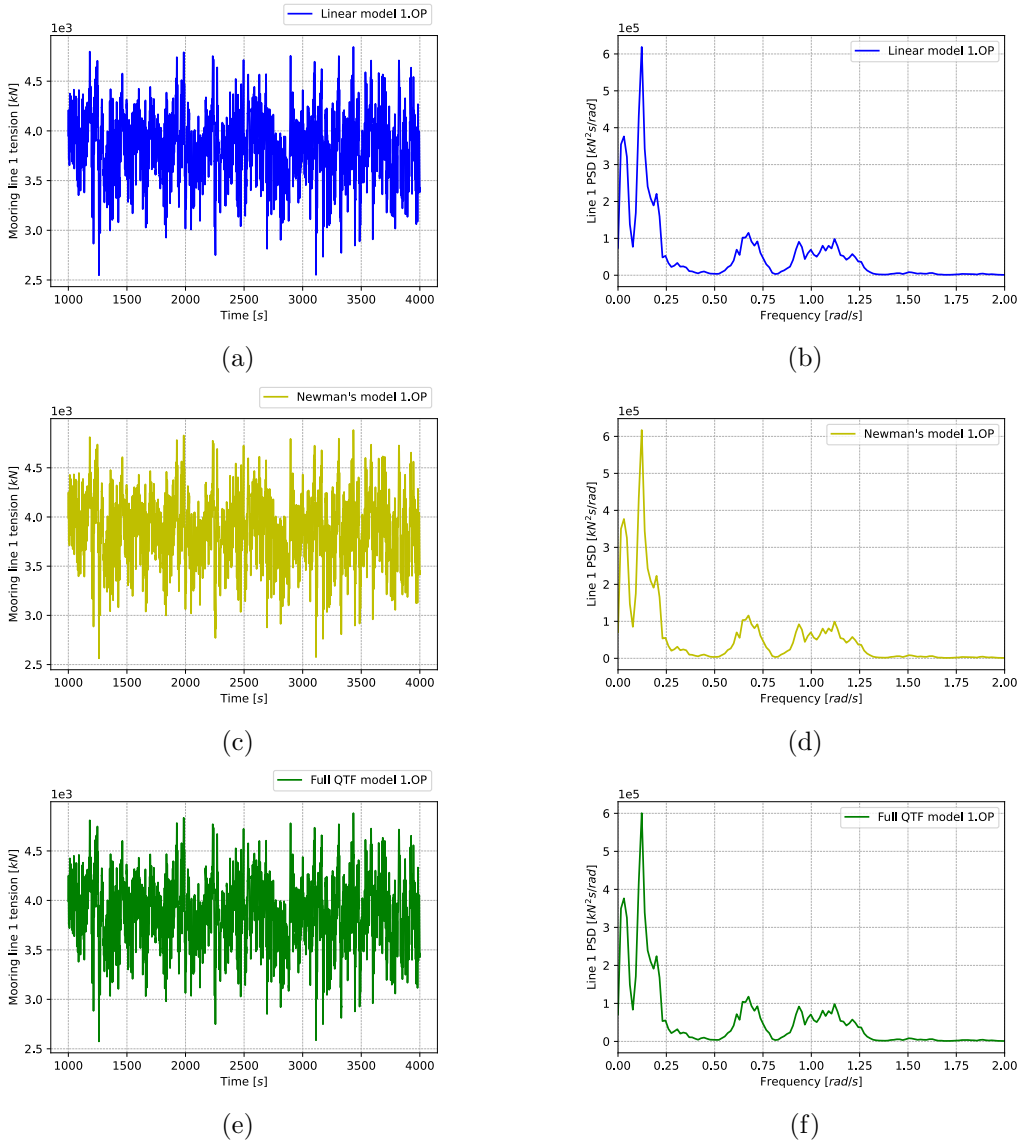

Figure B.4: Mooring line 1 tension and PSD for the three different models load case 1.OP

B.2 Load case 2.OP response

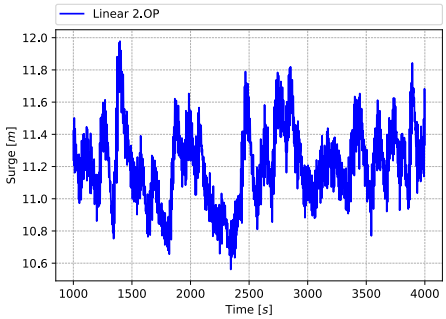

(a) Linear model timeseries surge 2.OP

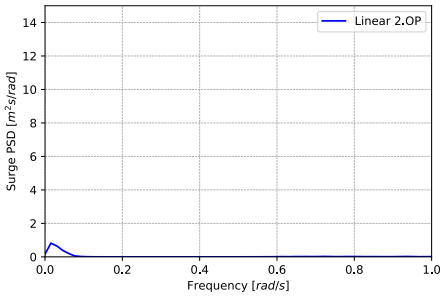

(b) Linear model PSD surge 2.OP

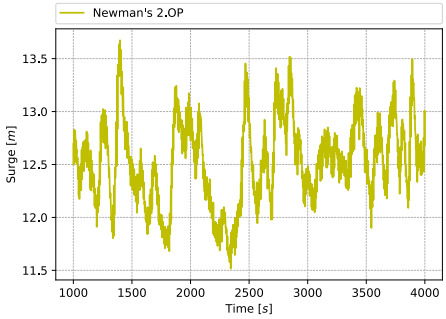

(c) Newman's model timeseries surge 2.OP

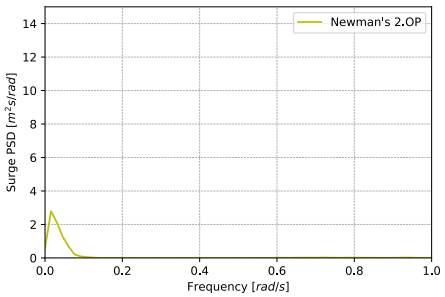

(d) Newman's model PSD surge 2.OP

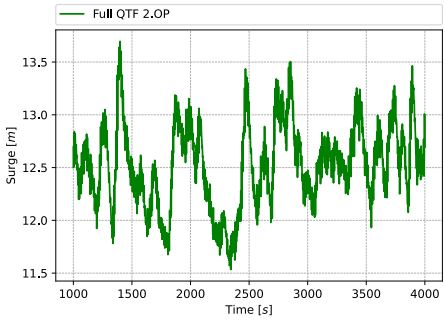

(e) Full QTF model timeseries surge 2.OP

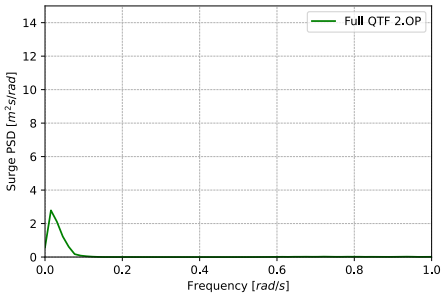

(f) Full QTF model PSD surge 2.OP

Figure B.5: Surge response 2.OP

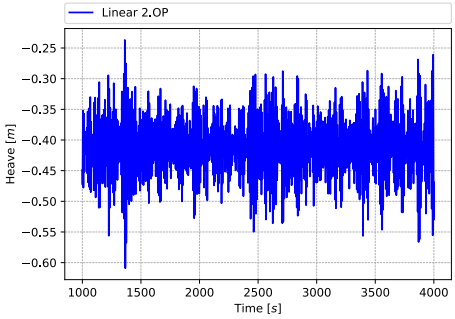

(a) Linear model timeseries heave 2.OP

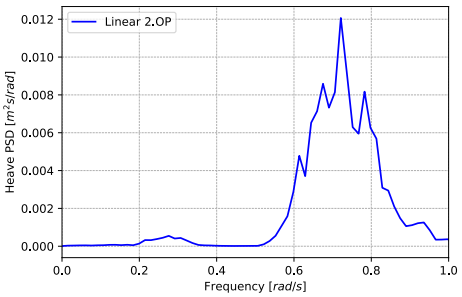

(b) Linear model PSD heave 2.OP

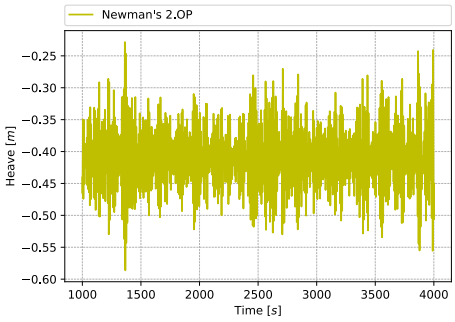

(c) Newman's model timeseries heave 2.OP

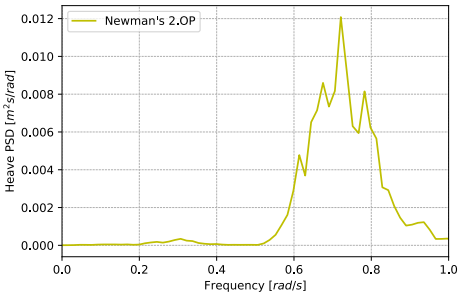

(d) Newman's model PSD heave 2.OP

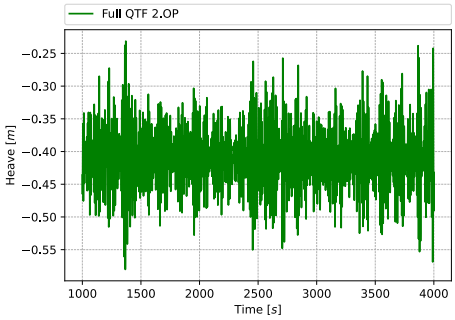

(e) Full QTF model timeseries heave 2.OP

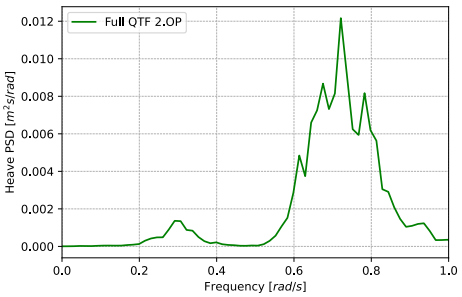

(f) Full QTF model PSD heave 2.OP

Figure B.6: Heave response 2.OP

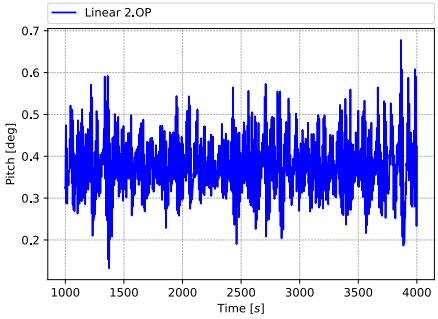

(a) Linear model timeseries pitch 2.OP

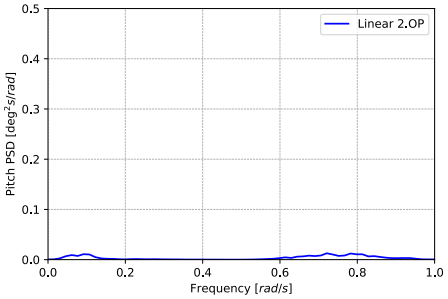

(b) Linear model PSD pitch 2.OP

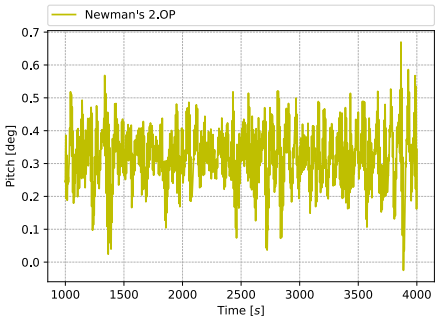

(c) Newman's model timeseries pitch 2.OP

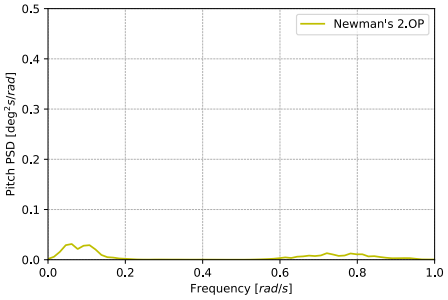

(d) Newman's model PSD pitch 2.OP

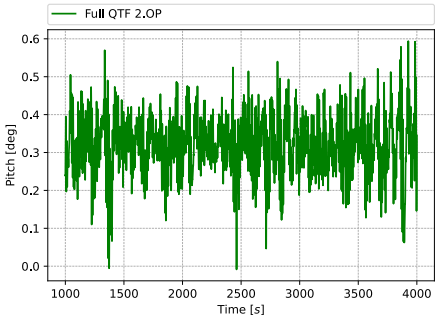

(e) Full QTF model timeseries pitch 2.OP

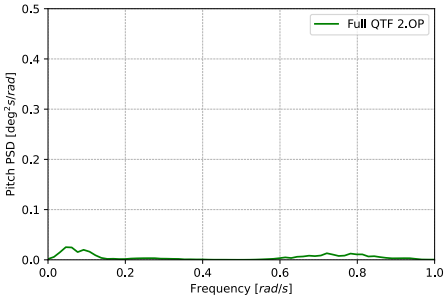

(f) Full QTF model PSD pitch 2.OP

Figure B.7: Pitch response 2.OP

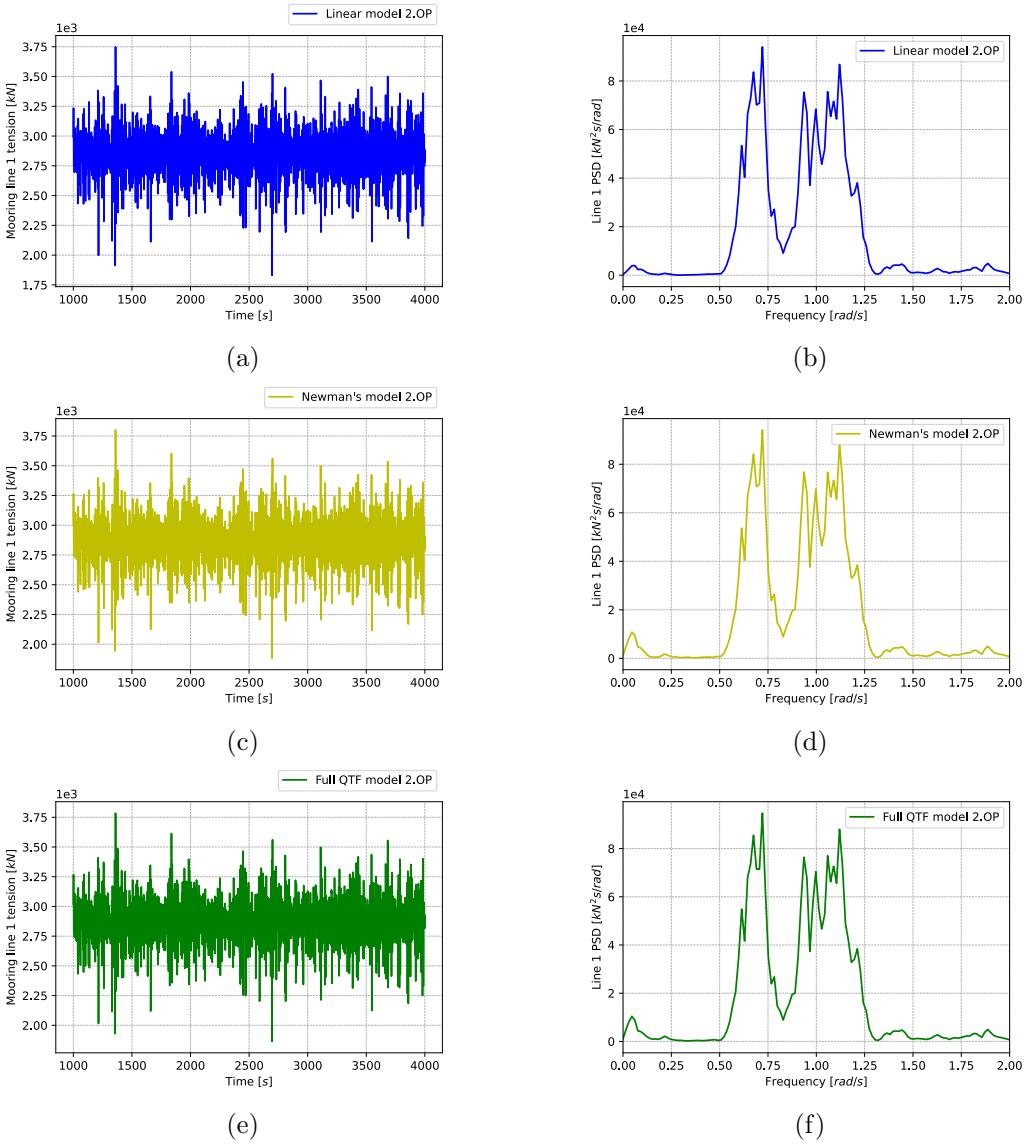

Figure B.8: Mooring line 1 tension and PSD for the three different models load case 2.OP

B.3 Load case 1.NC response

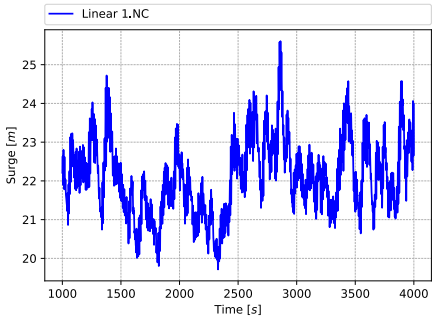

(a) Linear model timeseries surge 1.NC

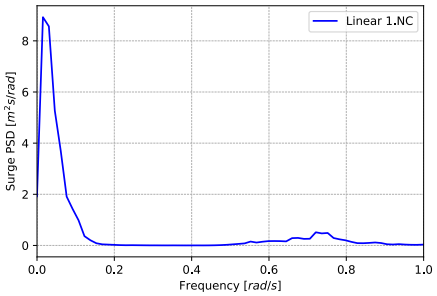

(b) Linear model PSD surge 1.NC

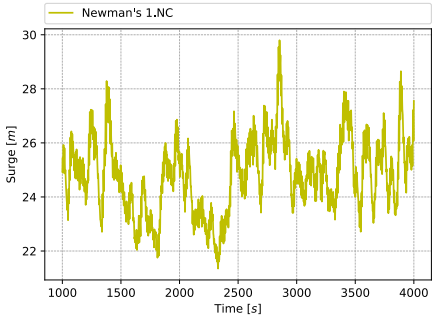

(c) Newman's model timeseries surge 1.NC

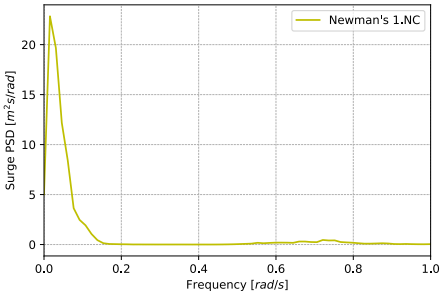

(d) Newman's model PSD surge 1.NC

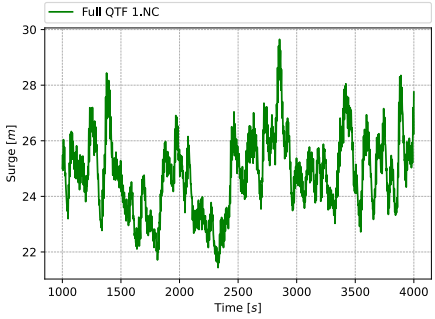

(e) Full QTF model timeseries surge 1.NC

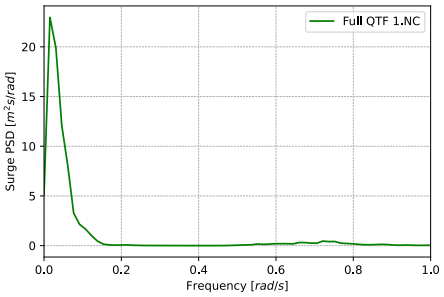

(f) Full QTF model PSD surge 1.NC

Figure B.9: Surge response 1.NC

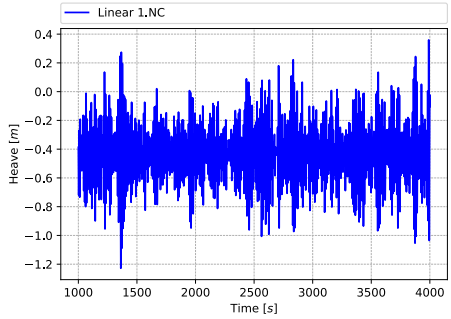

(a) Linear model timeseries heave 1.NC

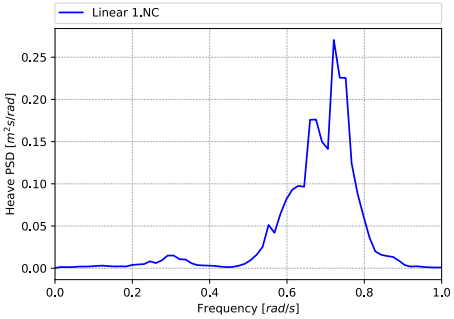

(b) Linear model PSD heave 1.NC

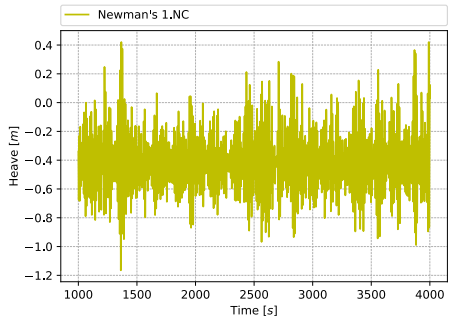

(c) Newman's model timeseries heave 1.NC

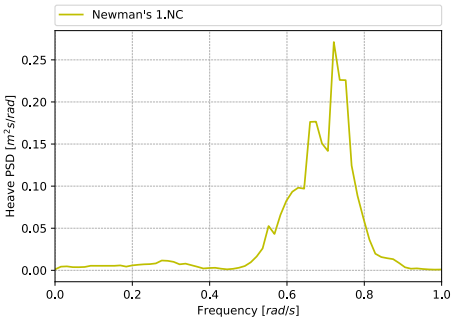

(d) Newman's model PSD heave 1.NC

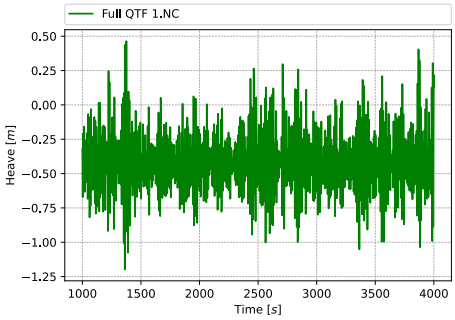

(e) Full QTF model timeseries heave 1.NC

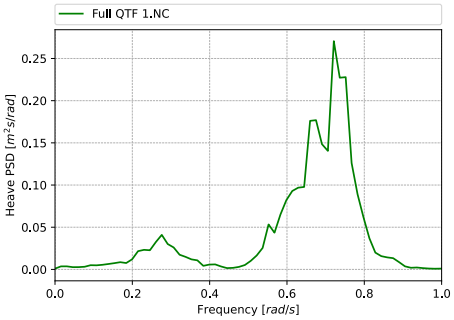

(f) Full QTF model PSD heave 1.NC

Figure B.10: Heave response 1.NC

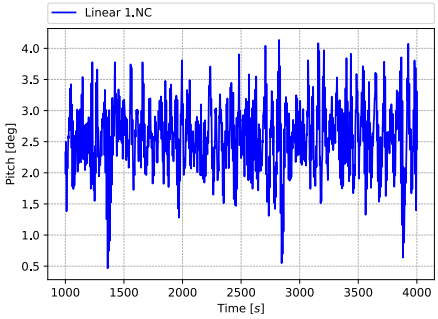

(a) Linear model timeseries pitch 1.NC

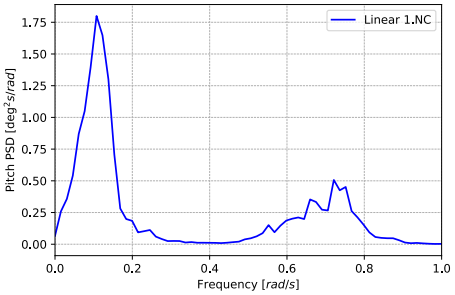

(b) Linear model PSD pitch 1.NC

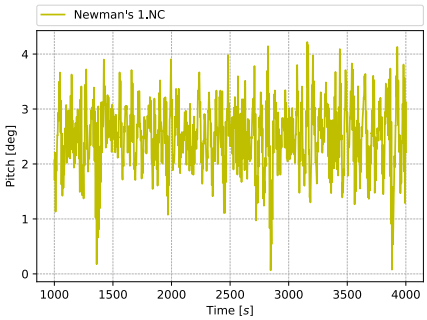

(c) Newman's model timeseries pitch 1.NC

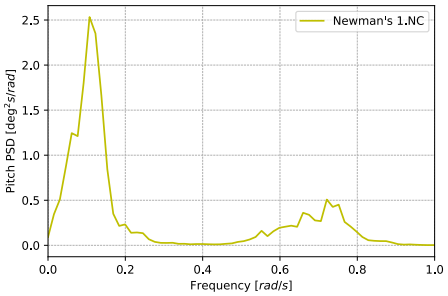

(d) Newman's model PSD pitch 1.NC

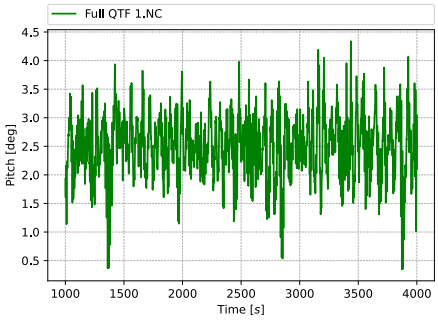

(e) Full QTF model timeseries pitch 1.NC

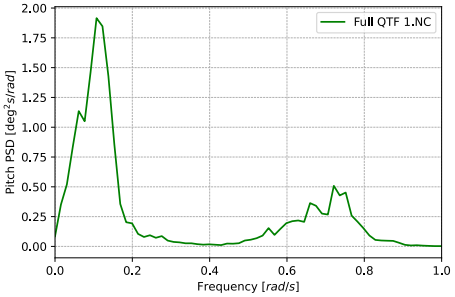

(f) Full QTF model PSD pitch 1.NC

Figure B.11: Pitch response 1.NC

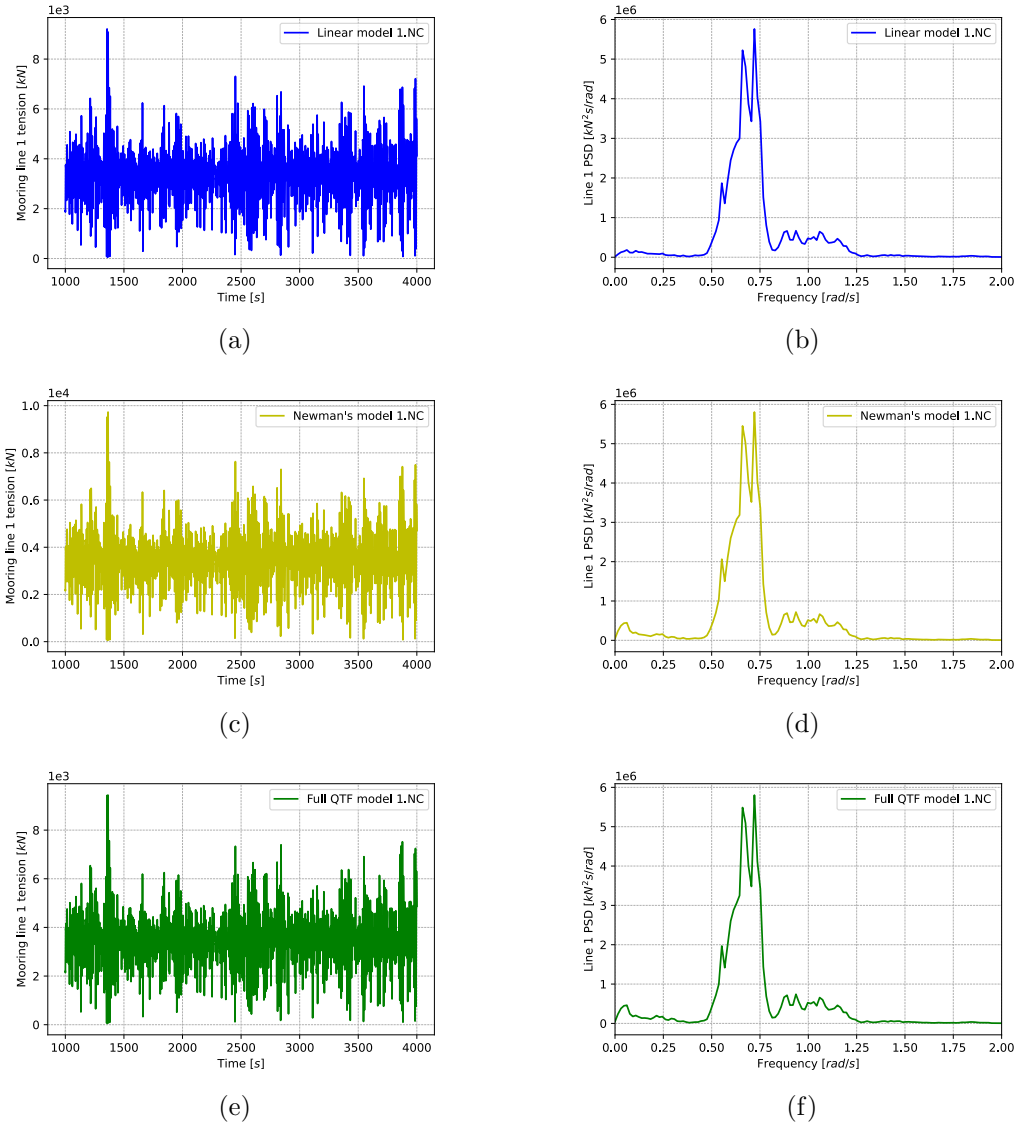

Figure B.12: Mooring line 1 tension and PSD for the three different models load case 1.NC

B.4 Load case 2.NC response

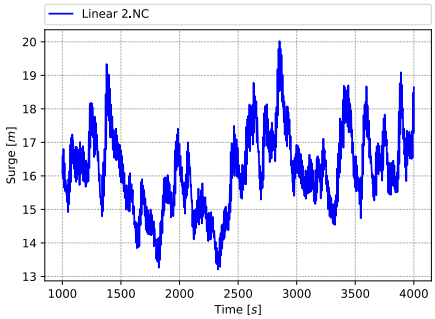

(a) Linear model timeseries surge 2.NC

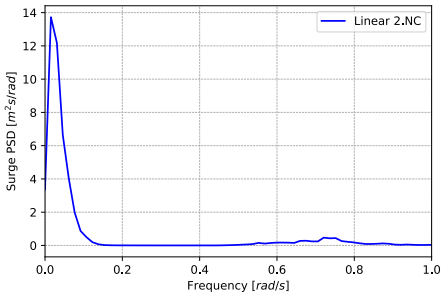

(b) Linear model PSD surge 2.NC

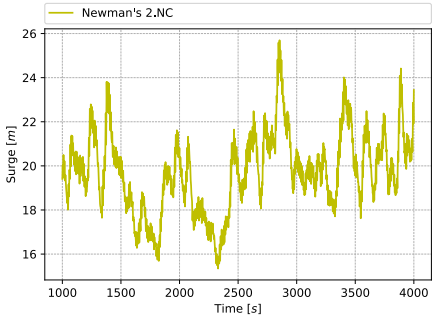

(c) Newman's model timeseries surge 2.NC

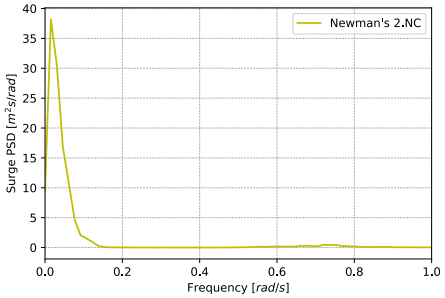

(d) Newman's model PSD surge 2.NC

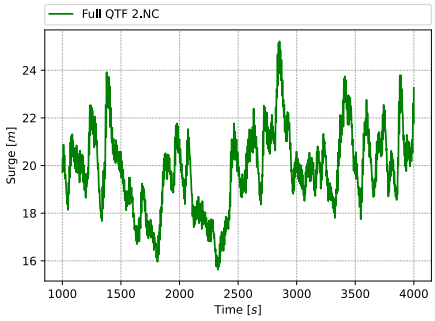

(e) Full QTF model timeseries surge 2.NC

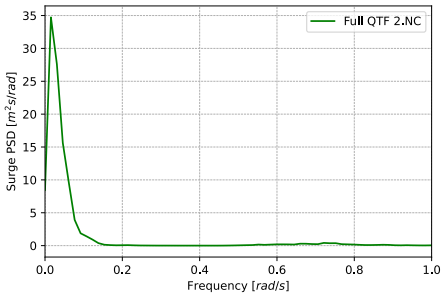

(f) Full QTF model PSD surge 2.NC

Figure B.13: Surge response 2.NC

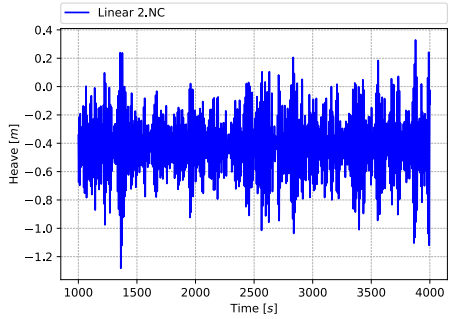

(a) Linear model timeseries heave 2.NC

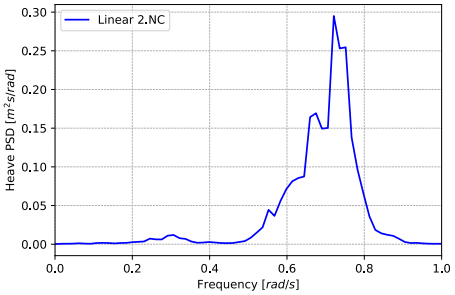

(b) Linear model PSD heave 2.NC

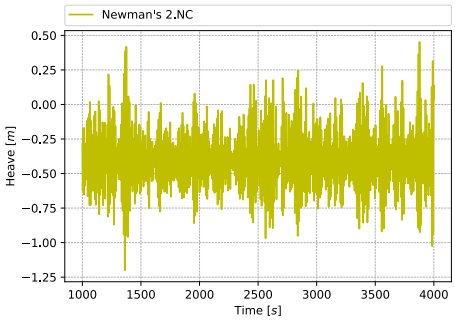

(c) Newman's model timeseries heave 2.NC

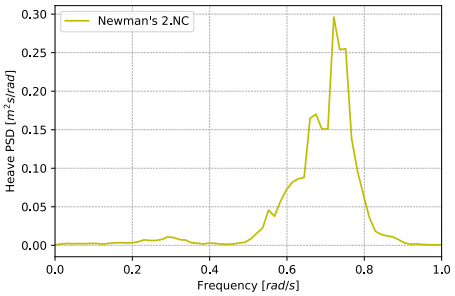

(d) Newman's model PSD heave 2.NC

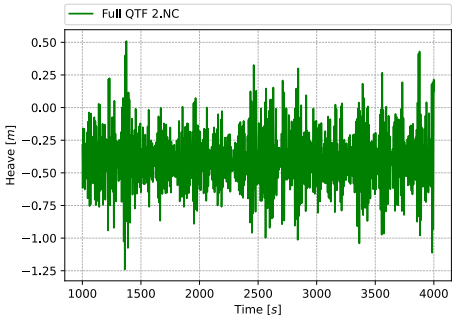

(e) Full QTF model timeseries heave 2.NC

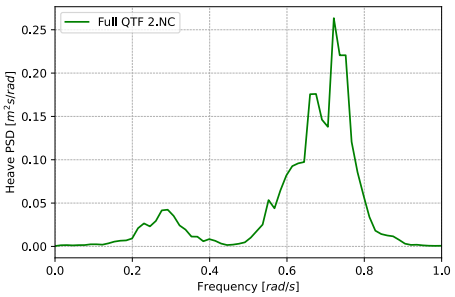

(f) Full QTF model PSD heave 2.NC

Figure B.14: Heave response 2.NC

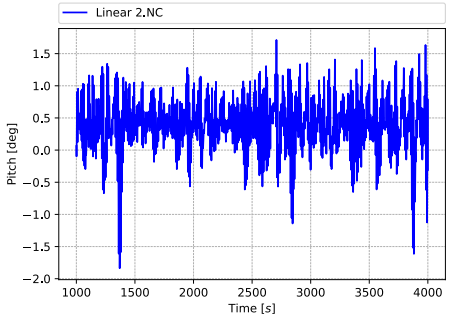

(a) Linear model timeseries pitch 2.NC

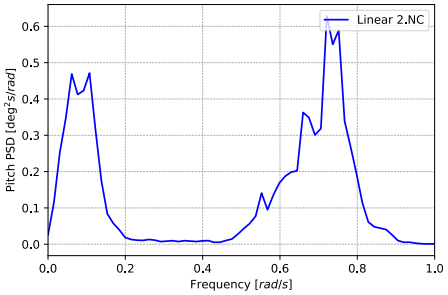

(b) Linear model PSD pitch 2.NC

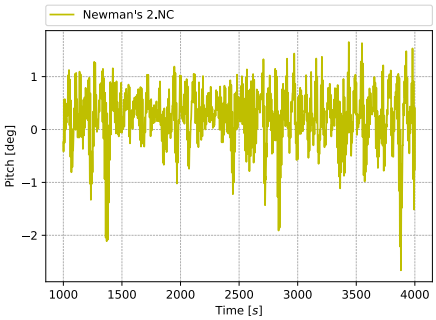

(c) Newman's model timeseries pitch 2.NC

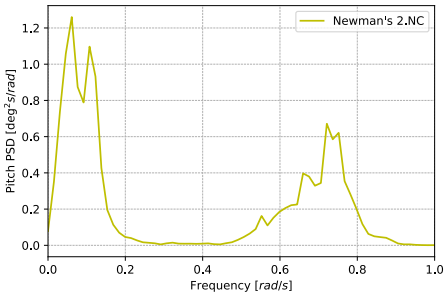

(d) Newman's model PSD pitch 2.NC

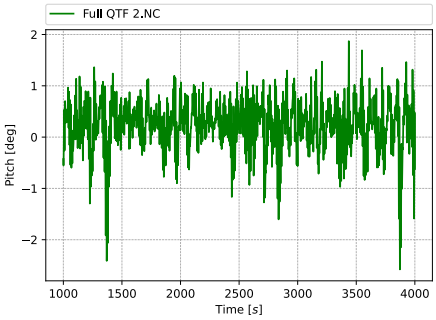

(e) Full QTF model timeseries pitch 2.NC

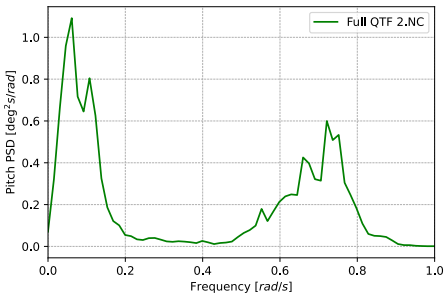

(f) Full QTF model PSD pitch 2.NC

Figure B.15: Pitch response 2.NC

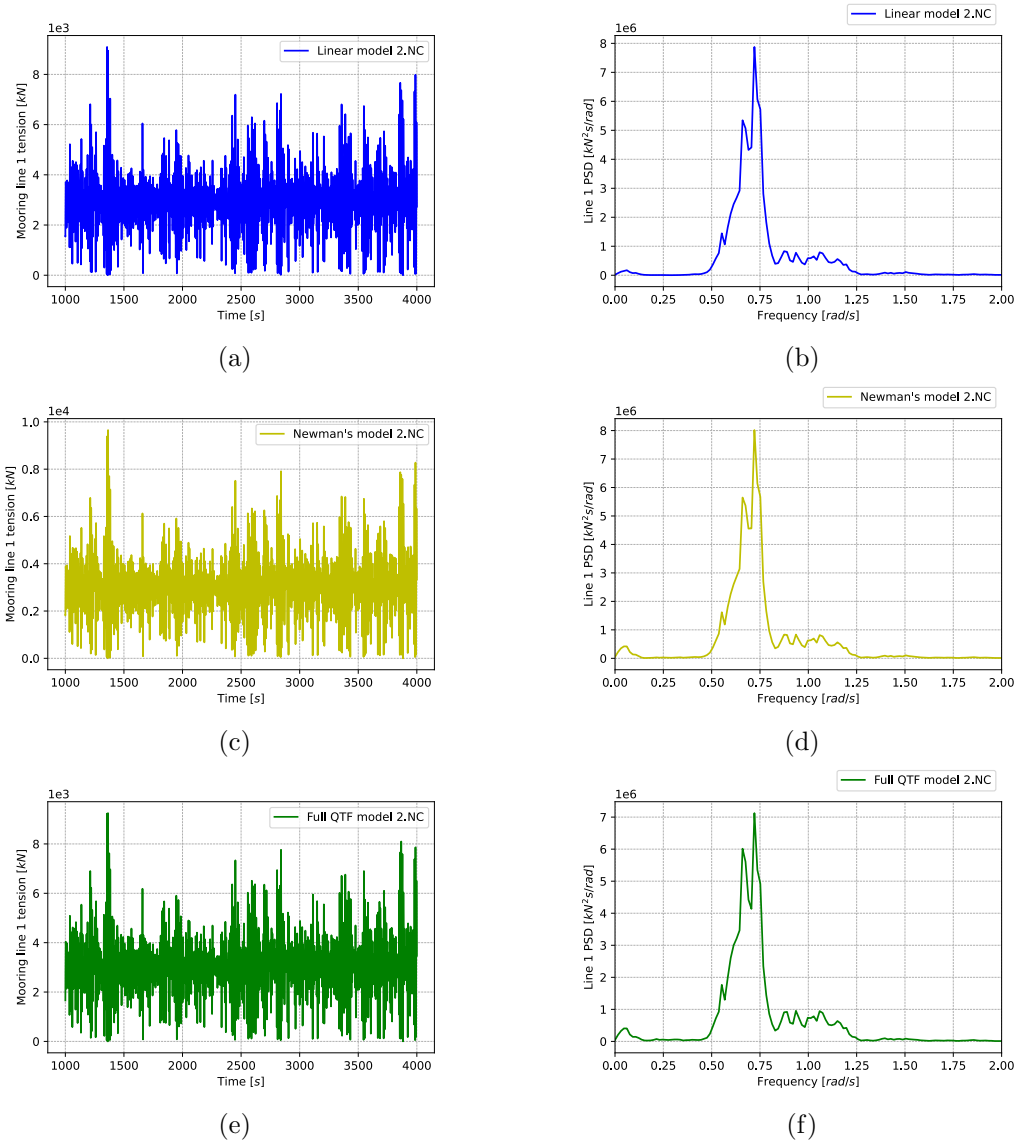

Figure B.16: Mooring line 1 tension and PSD for the three different models load case 2.NC

B.5 Load case 1.EX response

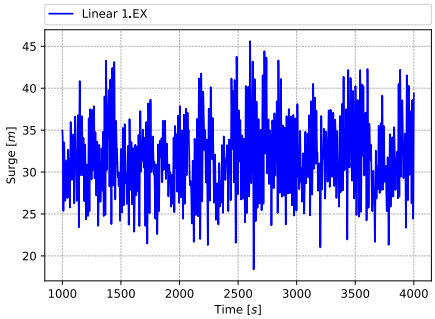

(a) Linear model timeseries surge 1.EX

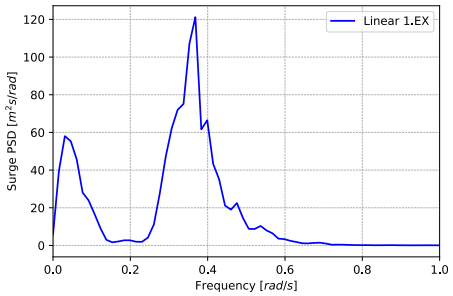

(b) Linear model PSD surge 1.EX

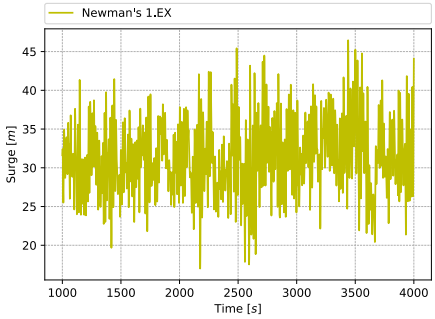

(c) Newman's model timeseries surge 1.EX

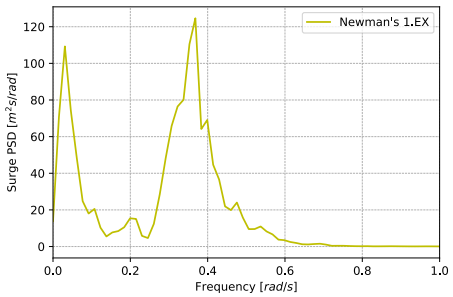

(d) Newman's model PSD surge 1.EX

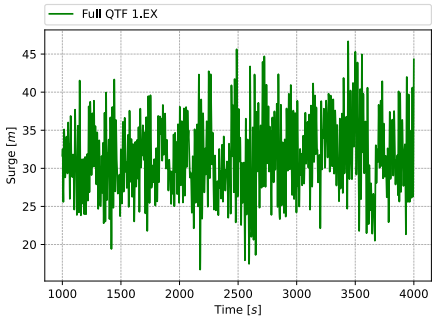

(e) Full QTF model timeseries surge 1.EX

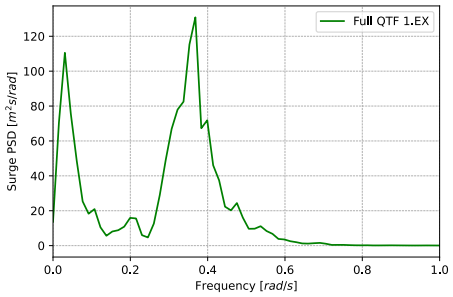

(f) Full QTF model PSD surge 1.EX

Figure B.17: Surge response 1.EX

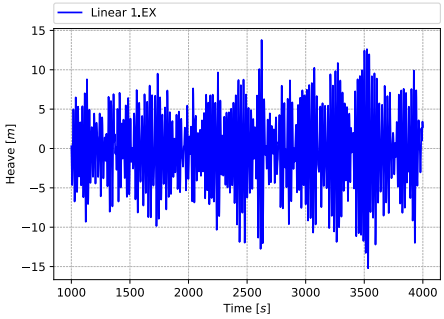

(a) Linear model timeseries heave 1.EX

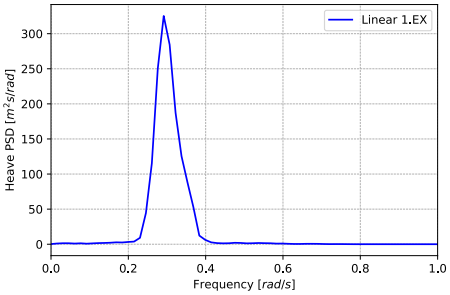

(b) Linear model PSD heave 1.EX

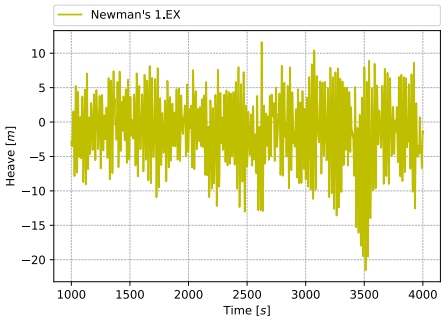

(c) Newman's model timeseries heave 1.EX

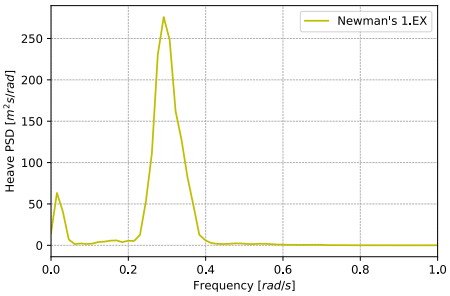

(d) Newman's model PSD heave 1.EX

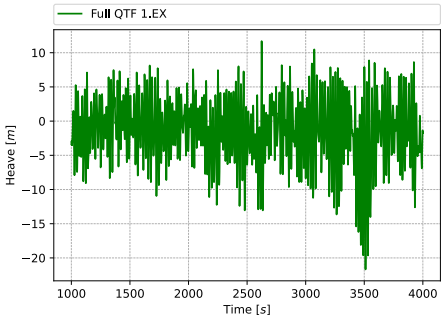

(e) Full QTF model timeseries heave 1.EX

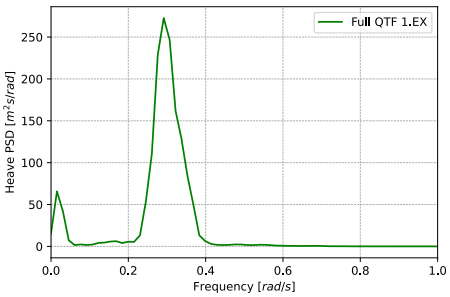

(f) Full QTF model PSD heave 1.EX

Figure B.18: Heave response 1.EX

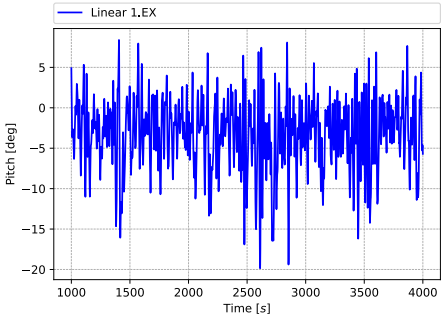

(a) Linear model timeseries pitch 1.EX

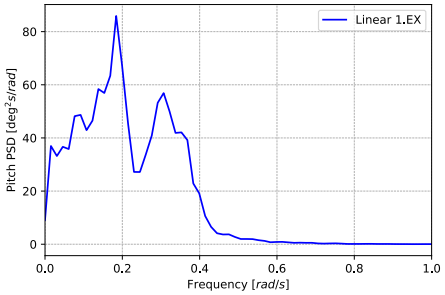

(b) Linear model PSD pitch 1.EX

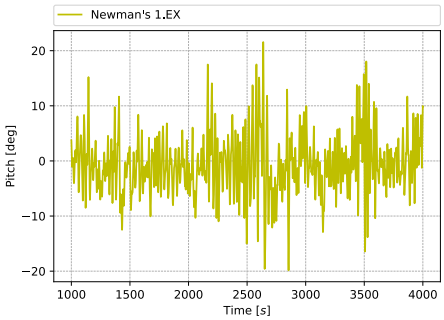

(c) Newman's model timeseries pitch 1.EX

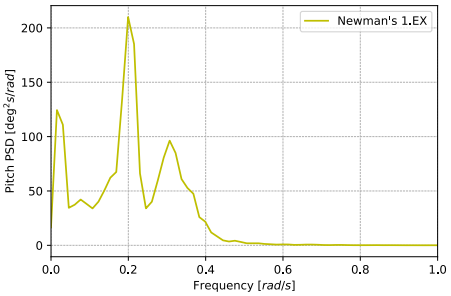

(d) Newman's model PSD pitch 1.EX

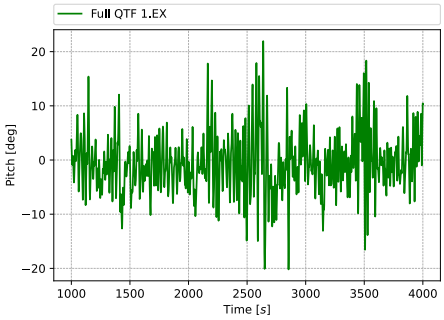

(e) Full QTF model timeseries pitch 1.EX

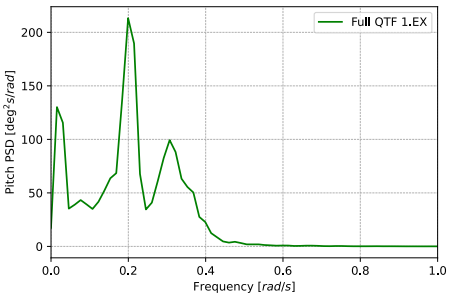

(f) Full QTF model PSD pitch 1.EX

Figure B.19: Pitch response 1.EX

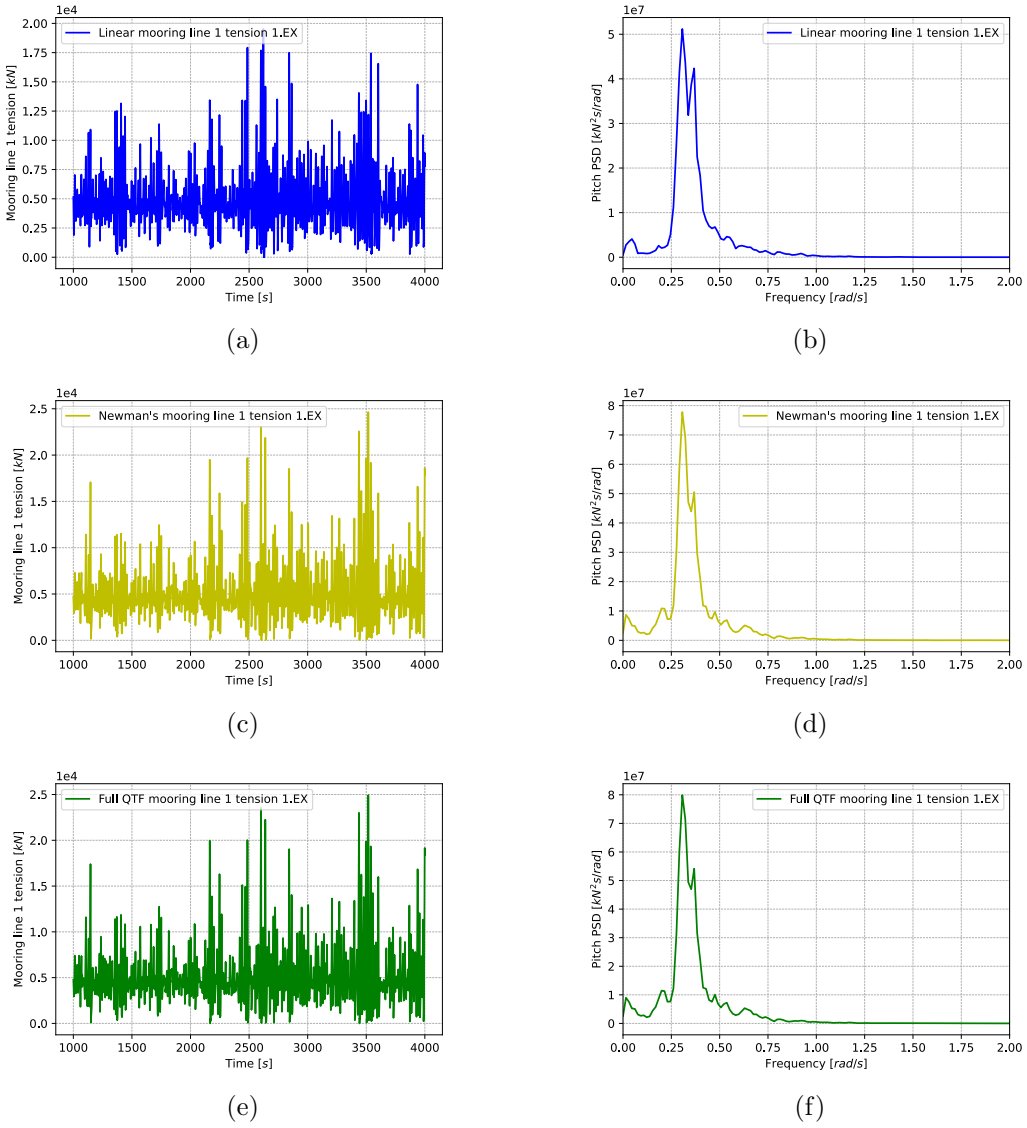

Figure B.20: Mooring line 1 tension and PSD for the three different models load case 1.EX

B.6 Load case 2.EX response

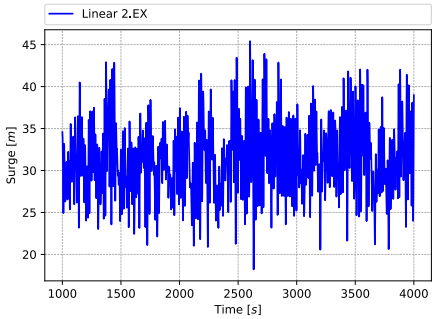

(a) Linear model timeseries surge 2.EX

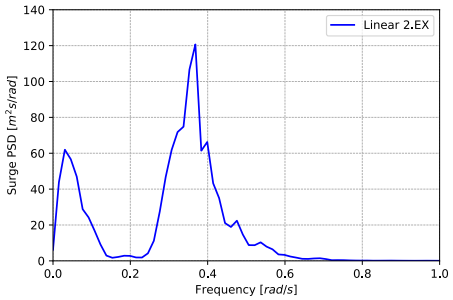

(b) Linear model PSD surge 2.EX

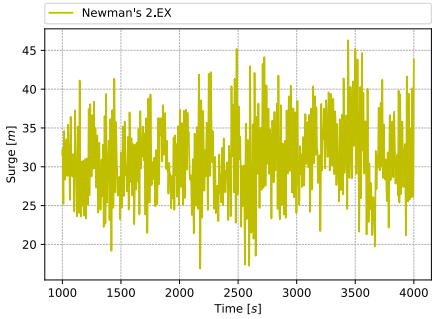

(c) Newman's model timeseries surge 2.EX

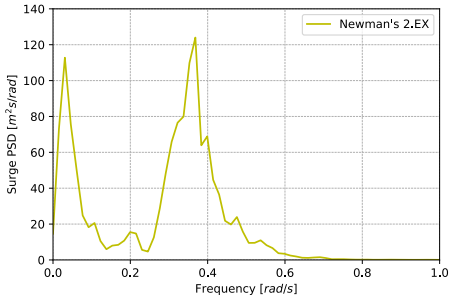

(d) Newman's model PSD surge 2.EX

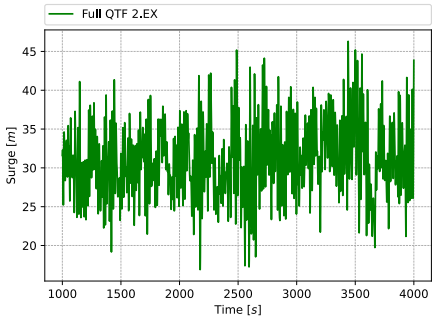

(e) Full QTF model timeseries surge 2.EX

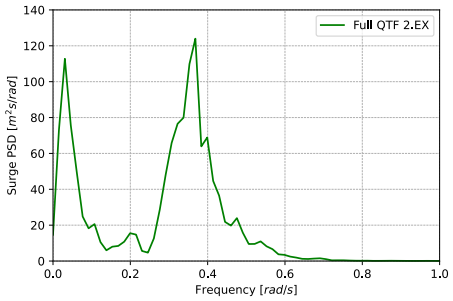

(f) Full QTF model PSD surge 2.EX

Figure B.21: Surge response 2.EX

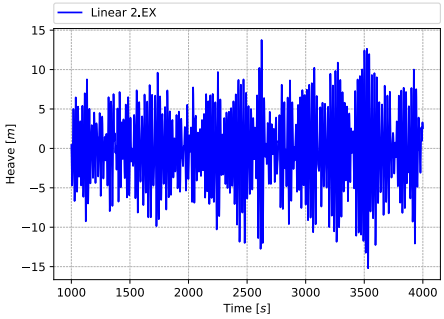

(a) Linear model timeseries heave 2.EX

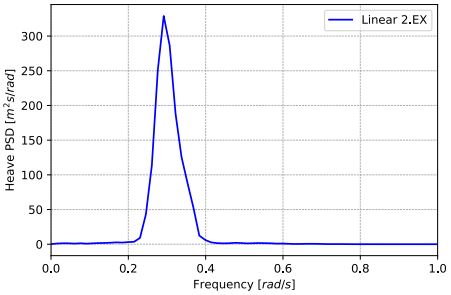

(b) Linear model PSD heave 2.EX

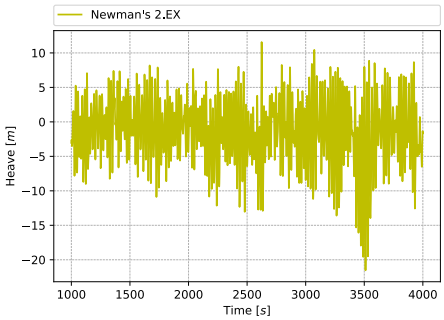

(c) Newman's model timeseries heave 2.EX

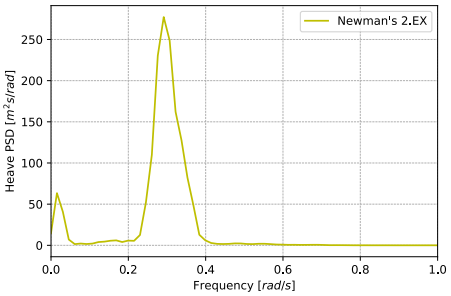

(d) Newman's model PSD heave 2.EX

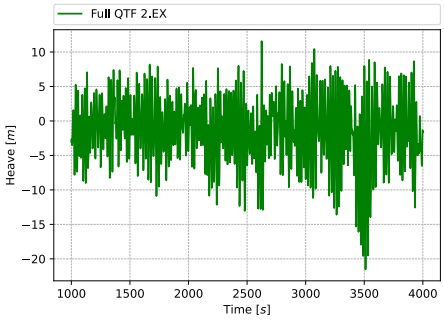

(e) Full QTF model timeseries heave 2.EX

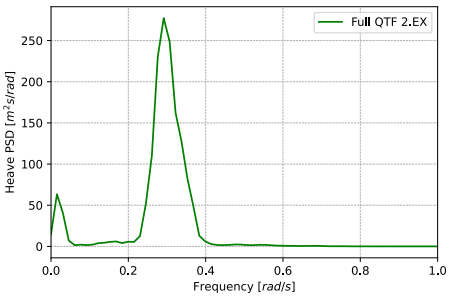

(f) Full QTF model PSD heave 2.EX

Figure B.22: Heave response 2.EX

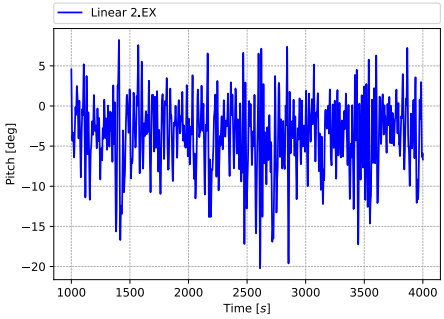

(a) Linear model timeseries pitch 2.EX

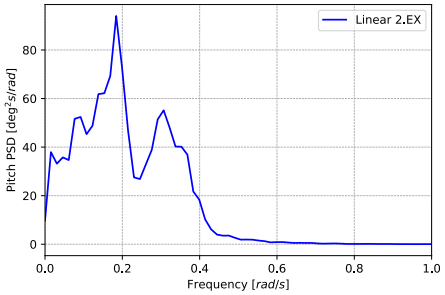

(b) Linear model PSD pitch 2.EX

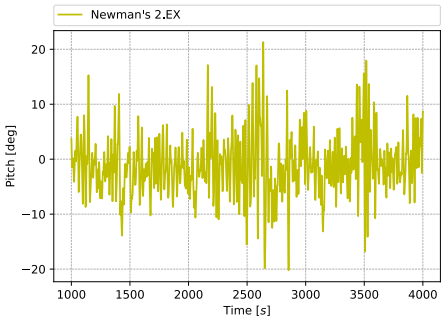

(c) Newman's model timeseries pitch 2.EX

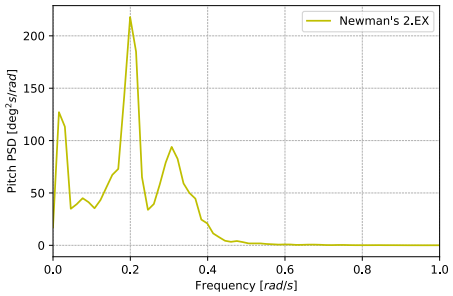

(d) Newman's model PSD pitch 2.EX

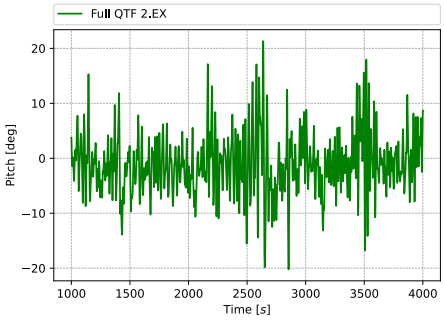

(e) Full QTF model timeseries pitch 2.EX

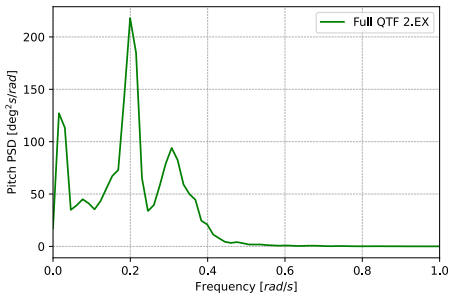

(f) Full QTF model PSD pitch 2.EX

Figure B.23: Pitch response 2.EX

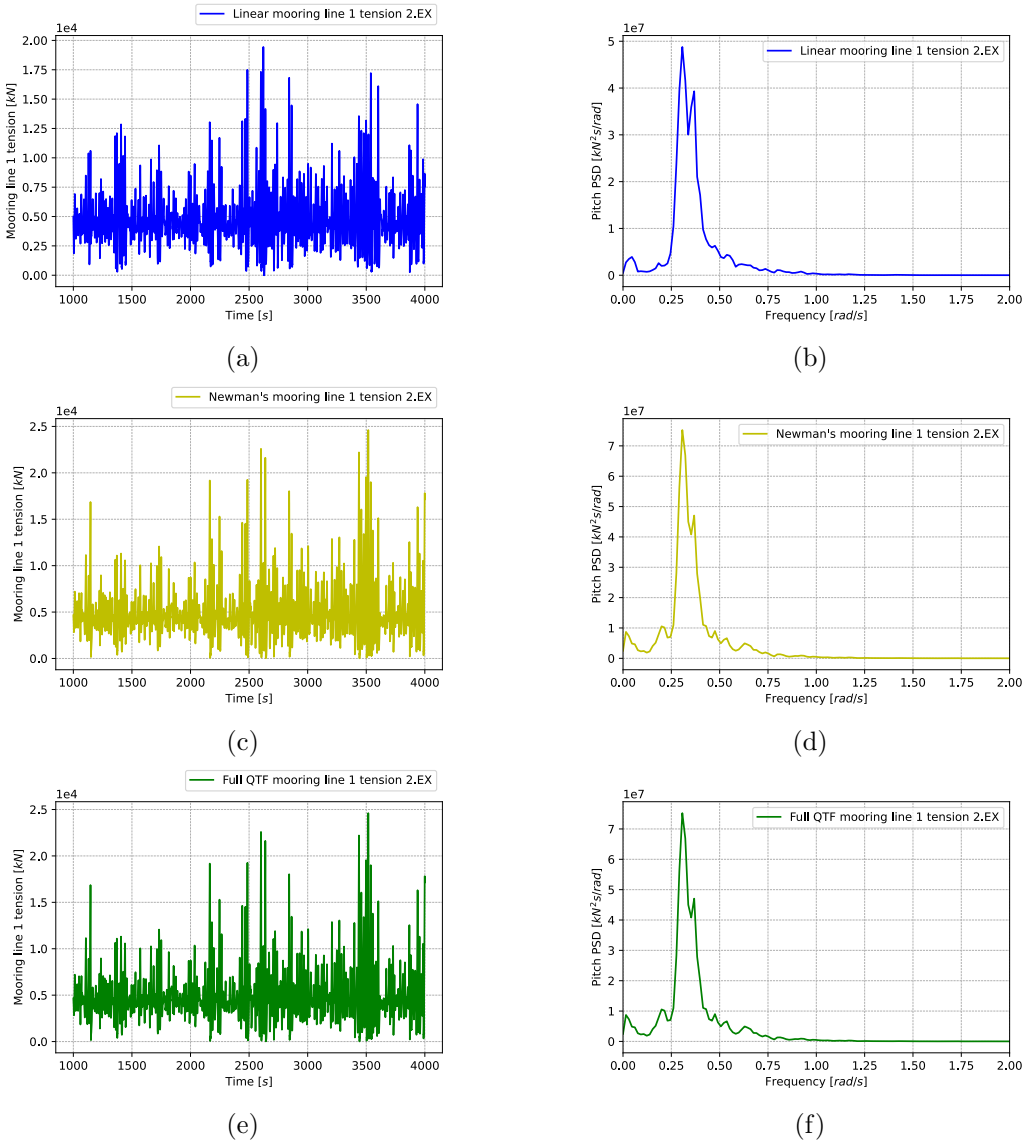

Figure B.24: Mooring line 1 tension and PSD for the three different models load case 2.EX

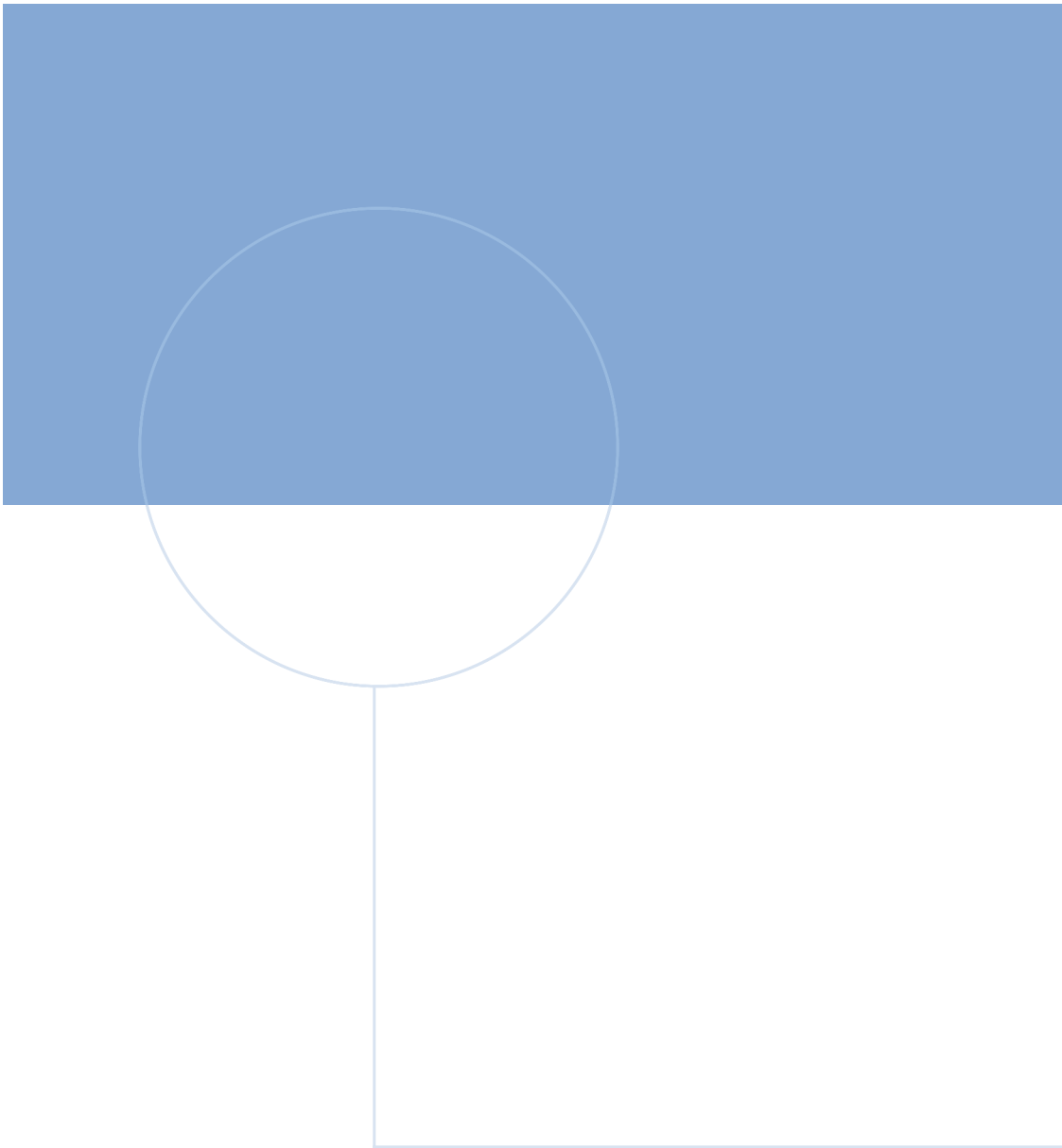

NTNU

Norwegian University of
Science and Technology